UNIVERSIDAD CARLOS III DE MADRID

TESIS DOCTORAL

DISCRETE MODELS OF DISLOCATIONS IN CRYSTAL LATTICES: FORMULATION, ANALYSIS AND APPLICATIONS

Modelos discretos de dislocaciones en redes cristalinas: formulación, análisis y aplicaciones

Autor:
Ignacio Plans Beriso

Directores:
Luis López Bonilla
Ana María Carpio Rodríguez

DEPARTAMENTO DE CIENCIA E INGENIERÍA DE MATERIALES E INGENIERÍA QUÍMICA

Grupo de Simulación, Modelización Numérica y Matemática Industrial

Leganés, Julio de 2007

TESIS DOCTORAL

Modelos discretos de dislocaciones en redes cristalinas: formulación, análisis y aplicaciones

Autor: Ignacio Plans Beriso

Directores: Luis López Bonilla y Ana María Carpio Rodríguez

Firma del Tribunal Calificador:

	(Nombre y apellidos)	Firma
Presidente:		
Vocal:		
Vocal:		
Vocal:		
Secretario:		

Calificación:

Leganés, de de 2007

A mi madre,
en el más amplio sentido.

ACKNOWLEDGEMENTS

The work presented in this thesis report has been developed under the direction of Professors Luis L. Bonilla and Ana Carpio. I acknowledge them for proposing this interesting research topic to me, as well as for their guidance in this project. They not only provided me with their help and advice, but also encouraged me to participate in the FPI program visiting other groups abroad. I also feel thankful to Jorge Sánchez-Ruiz, who firstly introduced me to Luis.

I would like to express my gratitude to the Spanish Ministry of Education and Science for funding me through the FPI program with grant BES-2003-1610 and projects BFM2002-04127-C02-01 and MAT2005-05730-C02-01. Thanks to the FPI short stays program (*programa de estancias breves FPI*) I had the chance to visit groups at UCLA and CalTech for several months.

The first part of Chapter 4 presented in this thesis was developed in collaboration with Prof. Russel Caflisch. I want to acknowledge him and his Materials Modeling in Applied Mathematics group at UCLA for their hospitality during two stays (2004 and 2005). I really enjoyed to discuss with Youri Bae, Xiaobin Niu, Young-Ju Lee and Christian Ratsch, to whom I felt really grateful for taking me in a comfortable cubicle during a later visit.

I feel thankful to Prof. Michael Ortiz and his Computational Solid Mechanics Group (Graduate Aeronautical Laboratories, CalTech) for their help and hospitality during my visit in 2006. I thank Ashwin Ramasubramaniam for his infinite patience and useful guidance, and Pilar Ariza for giving me the opportunity of learning from their theory. Fernando, Jee, Santiago, Mitsuhiro, Alejandro, Julián, Lydia, Marta and the rest of the group made my stay really rewarding.

I thank Professors Ya-Hong Xie, Jiun-Shyan Chen and Nasr M. Ghoniem at UCLA, and Gang Lu at CSU Northridge, for being always receptive either to answering my questions, having interesting discussions or inviting me to give a talk. I also feel

grateful to Prof. Frank E. Karasz and Ljiljana S. Korugic-Karasz at UMASS for their friendship.

At UC3M, Carmen Ballesteros was really patient answering all my questions on experiments in heteroepitaxial systems. Rosa María de la Cruz provided me with very useful guidance in a time in which her advice turned out to be essential for me.

My thanks are due to Jorge Galán-Vioque for his hospitality in my short visit to Seville, and his help with the program AUTO [1]. I remember that week as one of the most challenging ones in my PhD studies.

I also want to thank Universidad Carlos III de Madrid, for funding me as a Teaching Assistant in the Department of Mathematics during the first semester of my PhD studies.

My thanks are due to the people in charge of the Modeling and Numerical Simulation branch of the UC3M Mathematical Engineering PhD Program for making it possible for me to attend two *ECMI Modeling Weeks* when I started my graduate studies. These activities really motivated me to enjoy science.

I am also indebted to other people and institutions. IPAM recently invited me to the really interesting *Bridging Time and Length Scales in Materials Science and Bio-Physics: Reunion Conference I*, covering the full cost. I especially acknowledged the feedback from Prof. Mitchell Luskin in this conference. CISM partially funded me for attending a really useful course on dislocations in Udine, Italy.

I feel also grateful to Jesús Salas, Sara Cuenda, Alejandro Plans and David Muñoz (GUL, UC3M) for making my life inside a linux terminal easier. Beatriz Díaz and Nieves García were really efficient and helpful in any single detail concerning the management of the FPI program at UC3M. Miguel Moscoso shared his office and printer with me so I could improve the successive drafts of this report. Manuel Carretero was really helpful in managing the webpage of the Modeling and Numerical Simulation Group[1]. Discussions with Yossi Farjoun gave rise to many helpful comments. Francisco Bernal provided me with generous friendship and sharp sense of humor throughout these years. I believe I am completely ready to laugh a lot about myself

1 http://scala.uc3m.es

now. Patricia provided me with smart help in fixing some issues with the plots contained in this thesis, and also encouraged me to rise to every new challenge. Any attempt to capture into words the dimension of her infectious enthusiasm would be a failure for sure.

I have been so lucky to have Beatriz, Alejandro, Carlos and Elena as a source of joy, unique sense of humor and great courage to face difficulties.

I want to thank Patri, Paco, Marta, David, Roger, Ali, Minoo, Xavi, Karen, Hanne, Lin, Lan, Jorge, both Ricardos, Korinna, Alma, Nikos, Israel, Tony, Agus, Nonia, Roxana, Moisés, Susana, Ana, Eva, Martina, Laura, Marc, Christoph, Alexander and all the rest of the Jedi troops for accumulating such a strength of the Jedi Force.

I feel grateful to Ana, Rossmary, Paúl, Pedro, Nacho, Javi, Saúl, María José, Ángeles, Marina, Nona, José Ángel, Alfredo, Roberto, Luis, Matteo, Manuel, Marco, Leyla and friends, the omnipresent Danilo and *all* the rest of my colleagues for their friendship. Kenon, Gustavo, Carlos, Fran and Rodrigo were always present in my inbox, in many ways.

I would like to thank Lucía and Elena, as well as Irene, Félix, Natalia, Carlos, María and all the crew from the Conservatory of Music for being always there. The people from the *Ateneo* in Madrid also deserve my acknowledgement, since we shared many experiences at the beginning of our studies.

I deeply thank Miguel, Sara, David and Rafa, and also the *Berisos*, the *Plans-Portabellas*, the *Arturos* and the *Zielinskis* for all what I have learned from them. I especially would like to thank Oba for her wise advice, and Gongui for showing me how to enjoy a walk.

Backwards in time, my parents, my uncle Carlos Plans, Marek Zielinski, and Enrique Álvarez were essential to motivate my first steps either asking *'why?'* or enjoying the understanding of mathematics.

I find it deeply frustrating to attempt to write lists of people, since I must be leaving somebody inadvertently out. These days my mind is undergoing some kind of *scientific overflow*, which is exciting but also makes it more difficult to remember accurately

anything but work, formulas, simulations and results! There are many people to whom I feel grateful for their support during these years. I hope I sufficiently expressed my gratitude to them in private at the right moment, since to mention all of them, I would need to start writing another thesis.

CONTENTS

1

INTRODUCTION

1.1 MOTIVATION

Real crystal lattices are not perfect. They have defects such as dislocations, vacancies, and cracks that control the mechanical properties of materials, including crystal plasticity, creep, fatigue, ductility, brittleness, hardness and friction. Crystal growth, radiation damage of materials, and their optical and electronic properties are also strongly affected by defects, particularly dislocations.

Why is it so important to understand the behavior of defects in crystal lattices? An accurate description of defect dynamics may help to optimize the design and manufacture of important nanoelectronic devices such as those based on self-assembled quantum dots [2, 3] or superlattices [4]. Moreover, assessing *how and under which conditions dislocations nucleate* may become an essential issue, since they act as scattering centers, degrading charge transport properties in opto-electronic devices. But at the present time, even the homogeneous nucleation of dislocations is not completely understood. While there is a widespread feeling that it is related to some bifurcation occurring once a dislocation-free state becomes unstable, *no precise analysis and calculation of this bifurcation has been reported* [5, 6].

Think of another example: to build up a superlattice, heteroepitaxial structures of alternate slices of semiconductors having different lattice spacings are grown. But layers with quite different lattice parameters do not *fit seamlessly*! This typically results in the formation of *misfit* dislocations at the interfaces that separate different materials. Therefore, it is crucial to compute *threshold values* for the formation of dislocations in many important experiments: the critical shear stress for homogeneous nucleation of dislocations, the critical thickness of a thin film (and also the critical discrepancy between their lattice constants -the critical *misfit*-) in heteroepitaxial growth for interfacial misfit dislocations

formation, the critical stresses leading to dislocation nucleation from cracks or from nanoindentor tips, and so on.

The goal of this thesis is to provide some insight in the aforementioned issues. But, tackling these problems is not simple! Dislocations may affect phenomena such as the strength of materials occurring over many different scales of length and time and the properties at each scale are influenced by the others. At the present time there are different attempts to bridge the gaps between disparate scales by using detailed microscopic calculations such as molecular dynamics in small regions near defect cores and linear elasticity in the far field [7, 8, 9]. In this thesis, we have chosen to model dislocation dynamics at the nanoscale by versions of discrete elasticity that become the proper linear anisotropic elasticity of cubic crystals in the far field and allow motion of dislocations in a natural manner. One important advantage of these models is that they are amenable to analysis using bifurcation theory and numerical continuation methods. We have used these methods to study very simple scalar versions of discrete elasticity models for two-dimensional edge dislocations. Within these limitations, we have analyzed homogeneous nucleation of dislocations in sheared materials, misfit dislocations, nanoindentations and cracks. The simplicity of the models allows us to find a more precise picture of these phenomena that may be useful in the nanoscale. Whether these models can be used as part of multiscale/multiphysics calculations at larger scales, remains as a challenging task for future work.

1.2 WHAT IS A DISLOCATION?

An example of an *edge* dislocation in a square lattice is shown in Fig. 1. The atoms shown in the plot belong to the $z = 0$ plane, and the system may be easily extended to its corresponding three-dimensional simple cubic lattice by repetition of the represented atoms in subsequent $z = k$ planes, k being any integer. What does the distortion shown in Fig. 1 consist of? A simple way to construct this dislocation is to insert an extra half-plane of atoms (the extra-half column shown in dashed red line) in the crystal. The edge of this half-plane (i.e., the z axis) is the *dislocation line* of this *edge dislocation*, and it is usually represented in the plots by the symbol $\top$, which is oriented along to the extra-half column direction (note that in Fig. 1 it is inverted, so we have the symbol

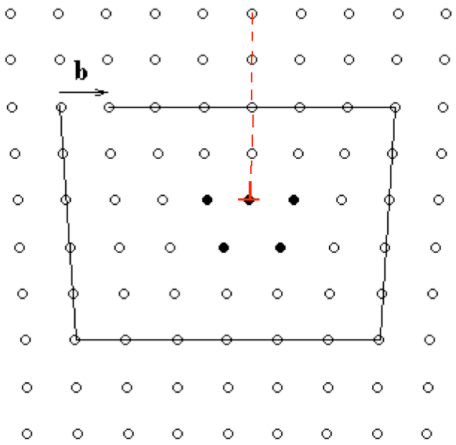

Figure 1. Burgers circuit encircling an edge dislocation with Burgers vector $b = (1, 0, 0)$.

$\perp$ in red at the end of the dashed line). Near the dislocation line, the lattice is greatly distorted but, as we move away from this *core* region, the planes of atoms fit almost regularly. The Burgers vector b measures the magnitude of the distortion caused by the dislocation. The simplest way to compute it for edge dislocations, is to count the number of extra half planes that have been added. In Fig. 1, just one half plane has been added, so $b = (+1, 0, 0)$, where the plus sign means that we have chosen the addition of *upper* half-planes to count as *positive* Burgers vectors.

It is useful to define a dislocation line unit vector, ξ. In Fig. 1, $\xi = (0, 0, 1)$ is perpendicular to the represented xy plane of atoms, lying along the z direction. There are different types of dislocations which may be classified according to the relative orientation of b and ξ:

- $b \perp \xi$ for *edge* dislocations (Fig. 1),
- $b \parallel \xi$ for *screw* dislocations (Fig. 7),
- any other relative orientations of b and ξ corresponds to *mixed* dislocations.

A way to compute the Burgers vector of any type of dislocation is to form the so-called Burgers circuit of lattice points around the dislocation line (see Fig. 1). Let us firstly consider the undistorted lattice, in which a closed circuit is chosen comprising a sequence

$i = 1, ..., N$ of vectors Δx_i whose sum is zero. These vectors connect neighboring atoms and (in the perfect lattice case) are lattice vectors, so that $\sum_{i=1}^{N} \Delta x_i = 0$. Let us then consider the distorted lattice and follow again the sequence $i = 1, ..., N$ of vectors $\Delta x_i'$ that connect neighboring atoms, trying to complete the circuit followed in the previous case. If the Burgers circuit encloses any dislocation, the vectors $\Delta x_i'$ are not perfect lattice vectors any more, and the resulting gap b which is missing to complete a closed circuit is defined to be the total Burgers vector of the dislocations which are present within the region delimited by the chosen circuit. Therefore,

$$\sum_{i=1,...,N} \Delta x_i' + b = 0. \tag{1.1}$$

When a Burgers circuit encloses several dislocations, the resulting Burgers vector is the sum of those corresponding to each of the enclosed dislocations. In Fig. 1, we have $b = (1, 0, 0)$, as explained before.

To define the Burgers vector more precisely, we follow Ref. [16]. Let the dislocation line point outside the page (the positive z axis) and let the circuit be oriented counter-clockwise, following the right-hand rule [14]. Let r_0 be an arbitrary lattice point which we take as the initial point of the circuit, and let $v_i, i = 1, \ldots, N$ be vectors of length equal to one lattice period comprising the Burgers circuit in the undistorted lattice, such that $\sum_{i=1}^{N} v_i = 0$. Each $v_i \in \{(1, 0), (-1, 0), (0, 1), (0, -1)\}$. The points of the Burgers circuit in the distorted lattice are such that r_i is the lattice point closest to $r_{i-1} + v_i$. A circuit that does not enclose a dislocation line ends at the initial point, $r_N = r_0$. A circuit containing a dislocation line is not closed, and we define *the Burgers vector* as [8]

$$b = r_N - r_0 = \sum_{i=1}^{N} \Delta u_i, \quad \Delta u_i = r_i - (r_{i-1} + v_i). \tag{1.2}$$

In our example, $b = (1, 0, 0)$, one period in the positive x direction.

The Burgers vector is the same for any deformation of the Burgers circuit as long as a dislocation line is not crossed during

the deformation process. If n dislocation lines merge at a lattice point and we take their directions to flow out of the common point, then conservation of the Burgers vector implies $b_1 + \ldots + b_n = 0$.

At low temperature, the motion of an edge dislocation such as that shown in Fig. 1 takes place along the *glide plane*, this plane is formed by the dislocation line and the Burger vector (the xz plane in Fig. 1).

There are many interesting introductory reviews and text-books on dislocations. For having a first glance, the webpage of Foell [10] may be of interest. A text-book introducing basic important concepts in a clear manner is the one written by Hull and Bacon [11]. Classical references are the book written by Nabarro [12] and the one by Landau and Lifshitz [13]. The text written by Hirth and Lothe [14] might be one of the most complete reference books on dislocations.

1.3 DIFFERENT DISLOCATION THEORIES

Since initiated by Volterra in 1905 within a continuum mechanics description, the theoretical study of dislocations has already been an active area of research for a whole century. In this section, existing theories of dislocations are presented following the books by Bulatov and Cai [8] and by Mura [15], and the paper by Bonilla and Carpio [16]:

- First-principles and atomistic calculations (Sec. 1.3.1).
- Continuum mechanics descriptions (Sec. 1.3.2).
- Classical theory of eigendistortions (Sec. 1.3.3).
- Dislocation-line tracking methods (Sec. 1.3.4).
- The Peierls-Nabarro model (Sec. 1.3.5).
- Discrete models approaches (Sec. 1.3.6).

The work described in this thesis fits within the last category in the previous list: discrete models of dislocations are formulated, analyzed and applied to different situations.

1.3.1 *First-principles and atomistic calculations*

Describing dislocations requires an accurate description of the atoms which are present in the crystal lattice and their dynamics. First-principles calculations such as density functional theory (DFT) are widely considered as a reference to provide information or validate other models that work at larger scales.

A more simplified description is provided by molecular dynamics (MD), which does not describe what happens *inside* the atoms, but only their interactions through an empirical potential ϕ, and the electron density, $\rho_e(r)$. The embedded-atom model (EAM) potential for a system having atoms at positions r_i is:

$$V(\{r_j\}) = \sum_{i,j,i<j} \phi(|r_i - r_j|) + \sum_i F(\bar{\rho}_i), \tag{1.3}$$

$$\bar{\rho}_i = \sum_{j \neq i} \rho_e(|r_i - r_j|). \tag{1.4}$$

This potential is widely used for metals [8]. It is a sum of two-body potentials and a so-called *glue-potential* density term, which contains an embedding function F that represents the energy needed to embed the atom i into an environment having electron density $\rho_e(r)$.

The procedure in MD consists of integrating the Newton equations of motion for all the atoms in a sample:

$$m\frac{d^2 r_i}{dt^2} = -\frac{\partial V}{\partial r_i}. \tag{1.5}$$

Improvements as the Modified EAM (MEAM) [17] (which includes angular dependence in the density term) and subsequent approaches, as well as many algorithmic optimization techniques, have set MD as a well-established technique for simulation creation and motion of dislocations, crack propagation, nanoindentations, and even protein folding. However, MD has several drawbacks:

- Potentials need to be fit to empirical data or first-principles calculations, which is not always possible to be done accurately.
- Great limitations in the time and length scales that may be described, due to the huge computational cost. Algorithms to update lists of neighboring atoms, for instance, must be run at every time-step.
- The information provided from the simulations might be difficult to extract or analyze.

1.3.2 *Continuum mechanics*

As mentioned, the theoretical study of dislocations was initiated by Volterra in 1905. The continuum mechanics approach consists of using the Navier equations of linear elasticity with singular source terms supported on dislocation lines. For a static dislocation in an isotropic medium, these equations are [14, 13]:

$$\Delta u + \frac{1}{1-2\nu}\nabla \mathrm{div} u = b \times \xi \, \delta_\Gamma, \tag{1.6}$$

in which u, b, ξ, and ν are the displacement vector from a lattice site, the Burgers vector, the unit tangent vector to the dislocation line Γ and the Poisson ratio, respectively. The displacement vector has a jump discontinuity of magnitude $|b|$ at a branch cut which, for the edge dislocation of Fig. 1, is the positive x axis:

$$\oint_c \nabla u \cdot dx = b, \tag{1.7}$$

where the integral is over any closed Burgers circuit c encircling the dislocation line. Note that 1.7 is the continuum version of 1.2. The circuit orientation determines the sign of b. Then the gradient of u and the stress have a singularity along the dislocation line: they are inversely proportional to the distance to the line, $1/r$. This unphysical behavior indicates that modeling a dislocation by 1.6 is a reasonable approximation of the elastic stress and strain at the far field of a dislocation, but this description breaks down at the dislocation core, near the origin. Moreover, elasticity gives no information about the motion of dislocations.

1.3.3 *Classical theory of eigendistortions*

The theory of eigendistortions explained in Mura's book [15] is widely used in plasticity. Instead of adding delta sources to the Navier equations, dislocations are included considering that the gradient of the displacement vector (the distortion tensor) is a sum of elastic and plastic distortions:

$$\frac{\partial u_i}{\partial x_j} = \beta_{ij} + \beta^*_{ij}, \tag{1.8}$$

with no source. The equations of motion are found from the stress-strain relation $\sigma_{ij} = c_{ijkl}\beta_{kl}$:

$$\rho\ddot{u}_i - \frac{\partial}{\partial x_j}\left(c_{ijkl}\frac{\partial u_k}{\partial x_l}\right) = -\frac{\partial}{\partial x_j}(c_{ijkl}\beta^*_{kl}), \tag{1.9}$$

where $\dot{u} = \partial u/\partial t$. For constant ρ, the solution of this equation is

$$u_i(x,t) = -\int c_{jlmn}\beta^*_{mn}(x',t')\frac{\partial G_{ij}}{\partial x_l}(x-x',t-t')dx'dt', \tag{1.10}$$

$$\rho\ddot{G}_{im} - c_{ijkl}\frac{\partial^2 G_{km}}{\partial x_l \partial x_j}(x,t) = \delta_{im}\delta(x)\delta(t), \tag{1.11}$$

where the elastic Green function satisfies the previous equation for $t > 0$ in $\mathbb{R}^3$ and $G_{km} = 0$ if $t < 0$. Further details are given in chapter 6 of Ref. [15].

The trouble with the classical theory is that the information on dislocation density and flux (or dislocation velocity) should be known in advance. Alternatively, equations for these magnitudes should be postulated. See for example the Boltzmann-like kinetic equations of Groma and Bakó [18]. Other recent approaches are the phasefield model [19] and the level set method, which is able to describe dislocation climb and cross-slip [20].

1.3.4 *Dislocation-line tracking methods*

A different approach to track the simultaneous evolution of a large number of dislocations in a continuum is to divide a given dislocation network into small straight segments (each having its own Burgers vector) and to consider their energies, forces acting on them, empirical dislocation velocity depending on the acting force, and mechanisms of dislocation creation [21, 22, 23, 24, 8]. The resulting theory can be used to numerically simulate and discuss more complex situations involving billions of dislocation segments.

1.3.5 *The Peierls-Nabarro model*

How to eliminate the singularity of the elastic strain at the origin? Since crystal lattices are discrete systems, the most obvious way is to consider an atomistic or discrete descriptions (See Secs. 1.3.1 and 1.3.6, respectively). However, there are non-atomistic models that eliminate the singularity without having to consider the crystal lattice as a regularization of elasticity. Among them, the Peierls-Nabarro (PN) is widely used. This model solves the equations of linear elasticity for a configuration with a straight dislocation such as that in Fig. 1. Here we consider only this one-dimensional situation with Burgers vector b directed along the positive x axis. There is a cut at the positive x axis such that $u(x) \equiv u_+(x) - u_-(x)$ is the relative displacement (the *disregistry*) across the cut plane. In a Volterra dislocation, $u(x)$ is the step function $b\theta(x)$, equal to b if $x > 0$ and zero otherwise. The disregistry density is $\rho_{dis}(x) \equiv du/dx = b\delta(x)$. In the PN model, ρ_{dis} is a smooth function and the force on the dislocation due to the elastic stress can be calculated to be the left hand side of the following equilibrium equation defining the model [8]

$$-\frac{\mu}{2\pi(1-\nu)}\int_{-\infty}^{\infty}\frac{\rho_{dis}(x')}{x-x'}dx' = \frac{U\pi}{b}sin\left(\frac{2\pi u(x)}{b}\right). \quad (1.12)$$

Here μ and U are the shear modulus and the energy per unit area of the cut plane, respectively. The right hand side of 1.12 is the force acting on the atoms as a result of having rigidly displaced the upper half of the crystal a distance $u(x)$ over the lower half.

This force is a b-periodic function of u and comes from the *misfit potential*:

$$\gamma(u(x)) = \frac{U}{2}\left[1 - cos\left(\frac{2\pi u}{b}\right)\right]. \tag{1.13}$$

A $\gamma(u(x))$ profile may be much more complex than the simple sine form shown here. An accurate calculation of these energies may be obtained from *ab initio* calculations such as DFT. Calculating $\gamma(u(x))$ becomes a much more complex task when the displacement vector x is spanned not only along one dimension as in the original PN approach, but over the two-dimensions along which two rigid blocks of a three-dimensional material may be shifted one with respect to the other. A two-dimensional γ-surface, which is also called Generalized Stacking-Fault (GSF) energy, results.

Peierls presented in 1940 [25] the following simple analytical solution of Eq. 1.12:

$$u(x) = \frac{b}{\pi}\tan^{-1}\left(\frac{x}{d}\right) - \frac{b}{2}, \quad d = \frac{\mu b^2}{4\pi^2 U(1-\nu)}, \tag{1.14}$$

in which d can be interpreted as the width of the dislocation core (actually, his original paper [25] was entitled *The Size of a Dislocation*). In Eq. 1.14, the stress field of this dislocation along the x axis is proportional to $x/(x^2 + d^2)$, and the singularity at $x = 0$ has been removed.

With exception of the discrete relative displacement $u(x) \equiv u_+(x) - u_-(x)$, the PN approach provides a continuum description, so it does not take into account the discrete nature of the crystal lattice. It does not describe properly the motion of dislocations and the existence of threshold stresses that are needed to start moving a dislocation (the so-called Peierls stress). Different modifications have improved the model, without changing its hybrid nature, that an atomistic force in the right hand side of Eq. 1.12 is balanced with the continuum response of the elastic medium on the left hand side of this equation. The ideas which are present in the PN approach pave the way to a discrete model description of dislocations.

1.3.6 *Discrete models*

Frenkel and Kontorova (FK) proposed in 1938 the first discrete approach to describe a model of interconnected harmonic springs in a periodic potential, which may be created by a fixed substrate. The displacements u_i have the following equations of motion [26, 12]:

$$m\frac{d^2u_i}{dt^2} = \kappa(u_{i+1} - 2u_i + u_{i-1}) - \frac{U\pi}{b}\sin\left(\frac{2\pi u_i}{b}\right). \qquad (1.15)$$

Considering a static dislocation, the equations describing the model are those in Eq. 1.12, where u has been replaced in the right hand side by u_i, i being an integer. The left hand side in Eq. 1.12 now becomes proportional to the discrete term $(u_{i+1} - 2u_i + u_{i-1})$. Dislocations are kink solutions of these equations [12], but the distortion $(u_{i+1} - u_i)$ decays exponentially far from the dislocation core, not as $1/i$ as the elastic far field of a true dislocation does. This unrealistic exponential decay remains in related models such as the discrete models of crystal growth by Frank and van der Merwe [27]. Other discrete models such as the Suzuki model of moving screw dislocations in terms of sliding chains [28] and the Landau-Kovalev-Kondratiuk model of interacting atomic chains (IAC) for edge dislocations [29] change the FK model so as to achieve algebraic decay of the distortion far from dislocation cores. They are all related to the FK model of idealized springs on a periodic substrate and are limited to simplified geometries. Moreover, these models are related to discretizations of linear elasticity by finite differences. A more recent discrete mechanics approach, found in Refs. [30, 31], is related to finite elements discretizations of elasticity. It uses algebraic topology to formulate discrete models consistent with empirical potentials.

The IAC model has been used in this thesis. It is simple, yet able to describe basic phenomena such as depinning of dislocations at the Peierls stress [32]. The IAC model of edge dislocations considers displacement vectors with a single non-zero component $(u_{i,j}(t), 0, 0)$ (in two space dimensions). The equations are [29]:

$$\begin{aligned}\frac{d^2u_{i,j}}{dt^2} + \gamma\frac{du_{i,j}}{dt} &= (u_{i+1} - 2u_i + u_{i-1}) \\ &\quad -A\left[\sin(u_{i,j} - u_{i,j+1}) + \sin(u_{i,j} - u_{i,j-1})\right], \qquad (1.16)\end{aligned}$$

where, for simplicity, the atomic masses and the interatomic distances are assumed to be equal to unity. Here γ is the dimensionless friction coefficient, and the dimensionless parameter A characterizes the amplitude of interaction between atoms of neighboring chains. The following Hamiltonian corresponds to Eq. 1.16:

$$H = \frac{1}{2}\sum_{i,j}\left(\frac{du_{i,j}}{dt}\right)^2 + \frac{1}{2}\sum_{i,j}(u_{i+1,j} - u_{i,j})^2 + \\ +A\sum_{i,j}\left[1 - \cos(u_{i,j} - u_{i,j+1})\right]. \tag{1.17}$$

Linearizing the right hand side of Eq. 1.16, the following continuum limit is obtained for the continuum displacement $u(x, y)$:

$$\frac{\partial^2 u}{dt^2} + \gamma\frac{\partial u}{\partial t} = \frac{\partial^2 u}{\partial x^2} + A\frac{\partial^2 u}{\partial y^2} = \frac{\partial^2 u}{\partial x^2} + \frac{\partial^2 u}{\partial (y^*)^2} = \Delta u, \tag{1.18}$$

where the coordinate y has been rescaled as $y^* = A^{-1/2}y$. The static continuum case satisfies the harmonic equation $\Delta u = 0$.

More complete models should recover anisotropic linear elasticity far from defect cores and yet allow dislocation glide. A simple way to achieve this is presented by Carpio and Bonilla in Ref. [33]: redefine the gradient of the displacement vector in the strain tensor as a nonlinear periodic function of the corresponding finite differences that restores the translation invariance of the crystal and allows sliding of atomic chains as a dislocation moves. Far from defect cores differences become differentials and linear elasticity is recovered. In Ref. [33], this idea is applied to simple cubic (SC), body centered cubic (BCC) and face centered cubic (FCC) crystals with one-atom basis. The resulting equations describe static and moving-edge and screw dislocations, including their cores and profiles, and can be used to study interaction of dislocations. Extensions of these models to cubic crystals with two-atom basis and addition of damping and fluctuations can be found in Chapter 2 of this thesis.

1.4 RESULTS OBTAINED IN THIS THESIS

Chapter 2 presents the *formulation* of our models:

- We formulate the models given in Ref. [33], and generalize them adding dissipation and fluctuation effects.
- We propose new models for FCC crystals having a two-atoms basis, such as Si or GaAs.
- We illustrate the case of static dislocations in a GaAs lattice, both for a 60° dislocation and a pure screw one.

The work presented in chapter 2 has been published in Refs. [34, 35, 36]

Chapter 3 contains the central results of this thesis. It considers homogeneous nucleation of dislocations in sheared, initially dislocation-free, crystals. This is an important problem retained to be crucial in interpreting experiments related to incipient plasticity at the nanoscale. An important tool we use is bifurcation theory from the dislocation-free stationary state. Stationary solutions whose atom profile displays dislocations issue forth from this state, typically as subcritical bifurcations. For overdamped dynamics, several of these solutions may be simultaneously stable, and ramping the applied shear stress with different characteristic times we may attain different multistable solutions at the same final stress. For undamped dynamics, stable solutions are not asymptotically stable. Results from this chapter will appear in forthcoming publications [37, 38].

Chapters 4 and 5 contain applications of simple discrete models to understant misfit dislocations, generation of dislocation in crack tips and in nanoindentations. In chapter 4, the InAs/-GaAs (110) heteroepitaxy is modeled using 2D discrete elasticity and an algorithm to relabel atoms finding their actual neighbors, without having to use periodic functions of displacement differences as in chapter 3. Relabeling avoids some limitations of periodic functions and a fixed computational grid discussed in Appendix A. Firstly, coherent and dislocated energy densities are calculated as a function of the thin film thickness. Secondly, the critical thickness for the presence of interfacial misfit dislocations is calculated, in good agreement with the experimental value. Finally, the critical misfit is studied with a simplified scalar elasticity model in a region close to the interface, showing that the system becomes linearly unstable for this threshold value. The work in chapter 4 will appear in a forthcoming publication [39].

In chapter 5, possible applications to model dislocation nucleation in crack formation and nanoindentation experiments are

investigated. We show that simple scalar two dimensional models reproduce an elementary ductile behavior around crack tips and basic dislocation nucleation mechanisms in simple indentation tests.

Chapter 6 contains the conclusions of this thesis. Appendix A is concerned with the periodic functions of the displacement differences: their usefulness is illustrated by a simple example and their definitions are provided, as well as a discussion on the different problems in which it might be convenient either using them or a relabeling algorithm. Appendix B presents additional results on homogeneous nucleation of dislocations. Appendix C is devoted to technical matters related to numerical continuation methods. Appendix D contains a summary of the thesis written in Spanish.

2

FORMULATION OF DISCRETE MODELS FOR DISLOCATION DYNAMICS IN CRYSTAL LATTICES

2.1 OUTLINE

Discrete models of dislocations in cubic crystal lattices having one or two atoms per unit cell are presented in this chapter. These models have the standard linear anisotropic elasticity as their continuum limit and their main ingredients are the elastic stiffness constants of the material and a dimensionless periodic function that restores the translation invariance of the crystal and influences the dislocation size. For these models, conservative and damped equations of motion are proposed. In the latter case, the entropy production and thermodynamic forces are calculated and fluctuation terms obeying the fluctuation-dissipation theorem are added. Numerical simulations illustrate static perfect screw and 60° dislocations for GaAs and Si. The ideas contained in App. A might be helpful to understand this chapter.

2.2 INTRODUCTION

Discrete model of dislocations and their motion in cubic crystals with a one atom basis have been previously proposed [33]. In this chapter, we present an extension of this previous theory to treat crystals with two-atom basis in their primitive cells (such as the diamond and zinc-blende structures of silicon and gallium arsenide, respectively). Moreover, we explain how to include dissipation in the dynamics of the model and how to consider the effect of fluctuations by using the ideas of fluctuating hydrodynamics [40, 41, 42]. Our model covers length scales in the nanometer range. In principle, to make contact with existing mesoscopic theories [43, 44, 45], one should define a dislocation density tensor and coarse grain over length scales up to hundreds

of nanometers. This is outside the scope of the present work.

The main ingredients entering our discrete model are the elastic stiffness constants of the material and a dimensionless periodic function that restores the translation invariance of the crystal and influences the dislocation size. To be precise, consider a simple cubic symmetry with one atom per lattice point. Firstly, we discretize space along the primitive vectors defining the unit cell of the crystal $\mathbf{x} \equiv (x, y, z) = (l, m, n)a$, in which a is the length of the primitive cubic cell, and l, m and n are integer numbers. Secondly, we replace the gradient of the displacement vector $\tilde{u}_i(x, y, z, t) = a\, u_i(l, m, n; t)$ ($u_i(l, m, n; t)$ is a nondimensional vector) in the strain energy density by an appropriate periodic function of the discrete gradient, $g(D_j^+ u_i)$: We shall define the *discrete* distortion tensor as

$$w_i^{(j)} = g(D_j^+ u_i), \tag{2.1}$$

$$D_1^{\pm} u_i(l, m, n; t) = \pm\,[u_i(l \pm 1, m, n; t) - u_i(l, m, n; t)], \tag{2.2}$$

etc., where $g(x)$ is a periodic function of period one satisfying $g(x) \sim x$ as $x \to 0$. The strain energy density for the discrete model is obtained by substituting the strain tensor in the usual strain energy density:

$$W = \frac{1}{2} c_{ijkl} e_{ij} e_{kl}, \tag{2.3}$$

$$c_{ijkl} = C_{12}\, \delta_{ij}\delta_{kl} + \frac{C_{11} - C_{12}}{2}\,(\delta_{ik}\delta_{jl} + \delta_{il}\delta_{jk})$$

$$+H \left(\frac{\delta_{ik}\delta_{jl} + \delta_{il}\delta_{jk}}{2} - \delta_{1i}\delta_{1j}\delta_{1k}\delta_{1l} - \delta_{2i}\delta_{2j}\delta_{2k}\delta_{2l} \right. \tag{2.4}$$

$$\left. -\delta_{3i}\delta_{3j}\delta_{3k}\delta_{3l} \right), \tag{2.5}$$

$$H = 2C_{44} + C_{12} - C_{11}, \tag{2.6}$$

$$e_{ij} = \frac{1}{2}\,(w_i^{(j)} + w_j^{(i)}) = \frac{g(D_j^+ u_i) + g(D_i^+ u_j)}{2} \tag{2.7}$$

(sum over repeated indices is assumed). Here $\lambda = C_{12}$, $\mu = (C_{11} - C_{12})/2$ are the usual Lamé coefficients if $H = 0$ and therefore the crystal is isotropic. Summing over all lattice sites, we obtain the

potential energy of the crystal:

$$V(\{u_i\}) = a^3 \sum_{l,m,n} W(l,m,n;t), \tag{2.8}$$

in which we have considered the strain energy deensity to be a function of the point $W(\mathbf{u}) = W(l,m,n;t)$, $(l,m,n) = (x,y,z)/a$. Next, we find the equations of motion with or without dissipation by the usual methods of classical mechanics. For conservative dynamics:

$$\rho a^4 \, \ddot{u}_i(l,m,n;t) = -\frac{1}{a} \frac{\partial V(\{u_k\})}{\partial u_i(l,m,n;t)}, \tag{2.9}$$

or, equivalently (see Section 2.3)[33],

$$\rho a^2 \, \ddot{u}_i = \sum_{j,k,l} D_j^- [c_{ijkl} \, g'(D_j^+ u_i) \, g(D_l^+ u_k)], \tag{2.10}$$

Here $\ddot{u}_i \equiv \partial^2 u_i / \partial t^2$ and the displacement vector is dimensionless, so that both sides of Eq. (2.10) have units of force per unit area. Let us now restore dimensional units to Equation (2.10), so that $\tilde{u}_i(x,y,z) = a \, u_i(x/a, y/a, z/a)$, then let $a \to 0$, use Eq. (2.10) and that $g(x) \sim x$ as $x \to 0$. Then we obtain the usual Cauchy equations of linear elasticity:

$$\rho \frac{\partial^2 \tilde{u}_i}{\partial t^2} = \sum_{j,k,l} \frac{\partial}{\partial x_j} \left(c_{ijkl} \frac{\partial \tilde{u}_k}{\partial x_l} \right), \tag{2.11}$$

provided the components of the distortion tensor are very small. Far from the core of a defect, the discrete gradient approaches the continuous one. Then, provided the slope $g'(0)$ is one in the appropriate units, the spatially discrete equations of motion become those of the anisotropic elasticity.

The periodic function $g(x)$ ensures that sliding a plane of atoms an integer number of times the lattice distance a parallel to a

primitive direction does not change the potential energy of the crystal. In this chapter, we choose

$$g(x) = \begin{cases} x & \text{if } -\alpha \leq x \leq \alpha, \\ -\alpha \left(\frac{x-1/2}{\alpha-1/2} \right) & \text{if } \alpha \leq x \leq 1-\alpha. \end{cases} \tag{2.12}$$

which is periodically extended outside the interval $(-\alpha, 1-\alpha)$ for a given $\alpha \in (0, 1/2)$ and has period one. The parameter α controls the asymmetry of $g(x)$, which in turn determines the size of the dislocation core and the Peierls stress needed for a dislocation to start moving [33]. As α increases, so does the Peierls stress, whereas both the core size and the mobility of defects decrease. High values of α result in very narrow cores and large Peierls stresses. Note that there are many possible ways to choose $g(x)$. We define a whole family of functions in App. A.

The rest of this chapter is organized as follows. In Section 2.3, we review the derivation of the governing equations with conservative dynamics for simple cubic symmetry, and give the numerical constructions of screw and edge dislocations. We use the well known screw and edge dislocations for anisotropic elasticity to set up the boundary conditions far from the dislocation core and the initial conditions in overdamped equations of motion. Numerical solution of these equations yields the static dislocation configuration of our discrete elasticity model. In Section 2.4 we include dissipation and fluctuations in the equations of motion. Dissipation is described by a Rayleigh dissipative function that is a quadratic functional of the strain rate tensor, which, in turn, depends on the discrete distorsion tensor. Since the distortion tensor (containing finite differences of the displacement vector) and its rate are larger near the core of defects, we expect that dissipation will be stronger near the core of a moving dislocation than at its far field. Fluctuations are introduced via the fluctuation-dissipation theorem and they should be stronger near the core of moving dislocations. An extension of our ideas to crystals with more complicated symmetries requires formulating our equations in non-orthogonal coordinates, which is explained in Section 2.5. The equations of motion for two-atom bases are obtained in Section 2.6 and the corresponding screw and 60° perfect dislocations are calculated for diamond and zinc-blende structures. Section 2.7 contains our conclusions.

In this Section, we shall derive the equations of motion (2.10) for the conservative dynamics given by (2.9). Firstly, let us notice that

$$\begin{aligned}\frac{\partial W}{\partial u_i(l,m,n;t)} &= \frac{\partial W}{\partial e_{jk}}\frac{\partial e_{jk}}{\partial u_i(l,m,n;t)} = \\ &= \frac{\sigma_{jk}}{2}\frac{\partial[g(D_j^+u_k)+g(D_k^+u_j)]}{\partial u_i(l,m,n;t)} = \\ &= \frac{\sigma_{jk}}{2}\left[g'(D_j^+u_k)\frac{\partial(D_j^+u_k)}{\partial u_i(l,m,n;t)} + \right. \\ &\qquad \left. + g'(D_k^+u_j)\frac{\partial(D_k^+u_j)}{\partial u_i(l,m,n;t)}\right], \end{aligned} \tag{2.13}$$

where W is a function of the point (l',m',n'), and we have used the definition of stress tensor:

$$\sigma_{ij} = \frac{\partial W}{\partial e_{ij}}, \tag{2.14}$$

and its symmetry, $\sigma_{ij} = \sigma_{ji}$. Now, we have

$$\begin{aligned}\frac{\partial}{\partial u_i(l,m,n;t)}[D_1^+u_k(l',m',n';t)] = \\ = \delta_{ik}\left(\delta_{l\,l'+1} - \delta_{ll'}\right)\delta_{mm'}\delta_{nn'}, \end{aligned} \tag{2.15}$$

and similar expressions for $j = 2,3$. By using (2.13) - (2.15), we obtain

$$\begin{aligned}\frac{\partial}{\partial u_i(l,m,n;t)}\sum_{l',m',n'} W(l',m',n';t) = \\ = -\sum_j D_j^-\left[\sigma_{ij}\,g'(D_j^+u_i)\right]. \end{aligned} \tag{2.16}$$

In this expression, no sum is intended over the subscript i, so that we have abandoned the Einstein convention and explicitly included a sum over j. Therefore Eq. (2.9) for conservative dynamics becomes

$$\rho a^2 \ddot{u}_i = \sum_j D_j^- [\sigma_{ij} g'(D_j^+ u_i)], \tag{2.17}$$

which yields Eq. (2.10). Except for the factor $g'(D_j^+ u_i)$, these equations are discretized versions of the usual ones in elasticity [13].

2.3.1 *Static dislocations of the discrete model*

To find the dislocation solutions of our model, we need the stationary solution of the anisotropic elasticity equations at zero applied stress corresponding to the same type of dislocation. In all cases, the procedure to obtain numerically the dislocation from the discrete model is the same. We first solve the stationary equations of elasticity with appropriate singular source terms to obtain the *dimensional* displacement vector $\tilde{\mathbf{u}}(x, y, z) = (\tilde{u}_1(x, y, z), \tilde{u}_2(x, y, z), \tilde{u}_3(x, y, z))$ of the static dislocation *under zero applied stress*. This displacement vector yields the far field of the corresponding dislocation for the discrete model, which is the *nondimensional* displacement vector:

$$\mathbf{U}(l, m, n) = \frac{\tilde{\mathbf{u}}\left((l + \delta_1)a, (m + \delta_2)a, (n + \delta_3)a\right)}{a}. \tag{2.18}$$

Here $0 \leq \delta_i < 1$, $i = 1, 2, 3$, are chosen so that the singularity at $x = y = z = 0$ does not coincide with a lattice point. For a sc crystal, it is often convenient to select the center of a unit cell, $\delta_i = 1/2$. We use the nondimensional static displacement vector $\mathbf{U}(l, m, n)$ defined by (2.18) in the boundary and initial conditions for the discrete equations of motion.

Take for example, a pure screw dislocation along the z axis with Burgers vector $\mathbf{b} = (0, 0, \mathrm{b})$ has a displacement vector $\tilde{\mathbf{u}} = (0, 0, \tilde{u}_3(x, y))$ with $\tilde{u}_3(x, y) = \mathrm{b}\,(2\pi)^{-1} \tan^{-1}(y/x)$ [12]. The

discrete equation for the z component of the *nondimensional* displacement $u_3(l,m;t)$ is:

$$\begin{aligned}\rho a^2\,\ddot{u}_3 &= C_{44}\{D_1^-[g(D_1^+u_3)\,g'(D_1^+u_3)] \\ &\quad + D_2^-[g(D_2^+u_3)\,g'(D_2^+u_3)]\}. \end{aligned} \tag{2.19}$$

Numerical solutions of Eq. (2.19) show that a static screw dislocation moves if an applied shear stress surpasses the static Peierls stress, $|F| < F_{cs}$, but that a moving dislocation continues doing so until the applied shear stress falls below a lower threshold F_{cd} (dynamic Peierls stress); see Ref. [32] for a similar situation for edge dislocations. To find the static solution of this equation corresponding to a screw dislocation, we could minimize an energy functional. However, it is more efficient to solve the following overdamped equation:

$$\begin{aligned}\beta\dot{u}_3 &= C_{44}\{D_1^-[g(D_1^+u_3)\,g'(D_1^+u_3)] \\ &\quad + D_2^-[g(D_2^+u_3)\,g'(D_2^+u_3)]\}. \end{aligned} \tag{2.20}$$

The stationary solutions of Eqs. (2.19) and (2.20) are the same, but the solutions of (2.20) relax rapidly to the stationary solutions if we choose appropriately the damping coefficient β. We solve Eq. (2.20) with initial condition $u_3(l,m;0) = U_3(l,m) \equiv \mathrm{b}\,(2\pi a)^{-1}\tan^{-1}[(m+1/2)/(l+1/2)]$ (corresponding to $\delta_i = 1/2$), and with boundary conditions $u_3(l,m;t) = U_3(l,m) + F\,m$ at the upper and lower boundaries of our lattice. At the lateral boundaries, we use zero-flux Neumann boundary conditions. Here F is an applied dimensionless stress with $|F| < F_{cs}$ (the dimensional stress is $C_{44}F$). For this small stress, the solution of Eq. (2.20) relaxes to a static screw dislocation $u_3(l,m)$ with the desired far field. Figure 3 of Ref. [33] shows the helical structure adopted by the deformed lattice $(l,m,n+u_3(l,m))$ for an asymmetric piecewise linear $g(x)$ as in Eq. (2.11). The numerical solution shows that moving a dislocation requires that we should have $g'(D_j^+u_3) < 0$ (with either $j=1$ or 2) at its core [32], which is harder to achieve as α increases. A discusion of the changes in the size of the dislocation core and the Peierls stress due to α can be found in Sec. A.1.2 of App. A. Using the same technique, stationary planar edge dislocations for an isotropic sc material have been constructed and a variety of dipole and loops of edge dislocations have been numerically found [33].

2.4.1 *Equations of motion including dissipation*

Overdamped dynamics obtained by replacing the time differential of the displacement vector instead of the inertial term in the equation of motion (2.10) is not too realistic. Instead, we can add dissipation to the equations of motion by considering a quadratic dissipative function with cubic symmetry:

$$\begin{aligned} R &= \left(\zeta - \frac{2}{3}\eta\right)\frac{\dot{e}_{ll}^2}{2} + \eta\dot{e}_{ik}^2 + \\ &\quad + \frac{\gamma}{2}(\dot{e}_{ik} - \dot{e}_{11}\delta_{1i}\delta_{1k} - \dot{e}_{22}\delta_{2i}\delta_{2k} - \dot{e}_{33}\delta_{3i}\delta_{3k})^2 \end{aligned} \tag{2.21}$$

For an isotropic body, we have $\gamma = 0$ and then ζ and η are the usual viscosities; see Eq. (34.5) in Ref. [13]. The viscous part of the stress tensor is the symmetric tensor

$$\Sigma_{ik} = \frac{\partial R}{\partial \dot{e}_{ik}} = \eta_{iklm}\dot{e}_{lm}, \tag{2.22}$$

$$\begin{aligned} \eta_{iklm} &= \frac{1}{2}\left(\zeta - \frac{2}{3}\eta\right)\delta_{ik}\delta_{lm} + \frac{\eta}{2}\left(\delta_{il}\delta_{km} + \delta_{im}\delta_{kl}\right) \\ &\quad + \frac{\gamma}{2}\left(\frac{\delta_{il}\delta_{km} + \delta_{im}\delta_{kl}}{2} - \delta_{1i}\delta_{1k}\delta_{1l}\delta_{1m}\right. \end{aligned} \tag{2.23}$$

$$\left. - \delta_{2i}\delta_{2k}\delta_{2l}\delta_{2m} - \delta_{3i}\delta_{3k}\delta_{3l}\delta_{3m}\right). \tag{2.24}$$

In the cubic case, the viscosity tensor η_{iklm} is determined by the three scalar quantities ζ, η and γ. For isotropic sc crystals, $\gamma = 0$. Similarly to Eq. (2.16), we can show that

$$\frac{\partial}{\partial \dot{u}_i(l,m,n;t)} \sum_{l',m',n'} R(l',m',n';t) = -\sum_j D_j^- \left[\Sigma_{ij}\, g'(D_j^+ u_i)\right], \tag{2.25}$$

is minus the dissipative force acting on u_i. Then the equation of motion including dissipation becomes

$$\rho a^2 \ddot{u}_i = \sum_j D_j^- [(\sigma_{ij} + \Sigma_{ij})\, g'(D_j^+ u_i)]. \tag{2.26}$$

In the isotropic case and taking the continuum limit $a \to 0$, Eqs. (2.26) with (2.22) and (2.24) yield the viscous Navier's equations for isotropic elasticity [13]:

$$\rho \frac{\partial^2 \tilde{\mathbf{u}}}{\partial t^2} = \mu \Delta \tilde{\mathbf{u}} + (\lambda + \mu) \nabla(\nabla \cdot \tilde{\mathbf{u}}) + \eta \Delta \frac{\partial \tilde{\mathbf{u}}}{\partial t} + \\ + \left(\zeta + \frac{\eta}{3}\right) \nabla \left(\nabla \cdot \frac{\partial \tilde{\mathbf{u}}}{\partial t}\right). \tag{2.27}$$

2.4.2 *Entropy production and fluctuations*

Fluctuations may be included in our formulation by using the ideas of Fluctuating Hydrodynamics [40, 41]. We need to find the entropy production and write it as sum of generalized forces and fluxes. Then both the forces and the fluxes are identified. The linear relations between forces and fluxes then yield the correlations of the fluctuating quantities to be added to the equations of motion.

To find the production of entropy, we need to derive a few formulas. Multiplying the conservative equations of motion for the model (2.17) by $\dot{u}_i$ and summing, we obtain

$$\frac{d}{dt} \sum_{l,m,n} \left[\sum_i \frac{\rho a^2}{2} \dot{u}_i^2 + W(l,m,n;t) \right] = 0, \tag{2.28}$$

after some algebra. Provided viscous terms are included in the equation of motion, as in Eq. (2.26), we find

$$\frac{d}{dt} \sum_{l,m,n} \left[\sum_i \frac{\rho a^2}{2} \dot{u}_i^2 + W(l,m,n;t) \right] = \tag{2.29}$$

$$= \sum_{l,m,n} \sum_{i,j} \dot{u}_i\, D_j^- [\Sigma_{ij}\, g'(D_j^+ u_i)]. \tag{2.30}$$

Let $D_j^- \phi = \phi - \phi^-$, where $\phi = \phi(l,m,n)$ is a function of the point (l,m,n). (Then $\phi^- = \phi(l-1,m,n)$ for $j=1$, and so on). We have $\psi D_j^- \phi = D_j^-(\psi\phi) - \phi^- D_j^- \psi$, and

$$\begin{aligned}\sum_{l,m,n} \psi D_j^- \phi &= \sum_{l,m,n} D_j^-(\psi\phi) - \sum_{l,m,n} \phi^- D_j^- \psi = \\ &= \sum_{l,m,n} D_j^-(\psi\phi) - \sum_{l,m,n} \phi D_j^+ \psi, \end{aligned} \tag{2.31}$$

after a trivial relabelling of indices. Using this formula, Eq. (2.30) becomes

$$\begin{aligned}\sum_{l,m,n} \Bigg\{ &\frac{d}{dt}\left[\sum_i \frac{\rho a^2}{2} \dot{u}_i^2 + W(l,m,n;t)\right] \\ &- \sum_{i,j} D_j^- \left[\dot{u}_i \, \Sigma_{ij} \, g'(D_j^+ u_i)\right] \Bigg\} = \\ = &- \sum_{l,m,n} \sum_{i,j} \Sigma_{ij} \, g'(D_j^+ u_i) \, (D_j^+ \dot{u}_i) \\ &= - \sum_{l,m,n} \sum_{i,j} \Sigma_{ij} \, \dot{e}_{ij}, \end{aligned} \tag{2.32}$$

where the symmetry of the viscous stress tensor has been used to derive the last equality. Eq. (2.32) describes the production of internal energy due to viscous processes.

If the temperature is not homogeneous, we need to replace the strain energy density to leading order by the elastic Helmholtz free energy density:

$$F(\mathbf{u};T) = F_0(T) - (T - T_0)\alpha_{ij} e_{ij} + \frac{1}{2} c_{ijkl} e_{ij} e_{kl}, \tag{2.33}$$

in which the symmetric tensor α_{ij} describes anisotropic thermal expansion and sum over repeated indices is again implied [13]. Here the material is undeformed at temperature T_0 in the absence of external forces and we assume that the temperature change $(T - T_0)$ which accompanies thermoelastic deformation is small (linear thermoelasticity). The stress tensor is now

$$\sigma_{ij} = c_{ijkl} e_{kl} - \alpha_{ij}(T - T_0), \tag{2.34}$$

which should be inserted in the equations of motion (2.17) or (2.26). The entropy density is $S(\mathbf{u};T) = -dF_0/dT + \alpha_{ij}e_{ij}$ if we ignore the temperature dependence of the elastic constants. Heat conduction is governed by the equation $T\,\partial S/\partial t = -\partial q_i/\partial x_i$, i.e.,

$$\rho c\frac{\partial T}{\partial t} + \alpha_{ij}T\frac{\partial e_{ij}}{\partial t} = -\frac{\partial q_i}{\partial x_i}, \qquad q_i = -\kappa_{ij}\,\frac{\partial T}{\partial x_j}. \tag{2.35}$$

Here c is the specific heat of the solid and κ_{ij} is the symmetric thermal conductivity tensor. These equations become

$$\rho ac\,\dot{T} + a\,\alpha_{ij}T\,g'(D_j^+u_i)\,D_j^+\dot{u}_i = -D_i^-Q_i, \tag{2.36}$$

$$Q_i = -\kappa_{ij}\frac{D_j^+T}{a}, \tag{2.37}$$

after discretizing. Eq. (2.32) can be rewritten as

$$\sum_{l,m,n}\left\{\frac{d}{dt}\left[\sum_i\frac{\rho a^2}{2}\dot{u}_i^2 + W(l,m,n;t)\right]\right. \tag{2.38}$$

$$\left. -\sum_j D_j^-\left[\sum_i \dot{u}_i\Sigma_{ij}g'(D_j^+u_i) - \frac{Q_j}{a}\right]\right\} =$$

$$= -\sum_{l,m,n}\sum_j\left(\sum_i\Sigma_{ij}\,\dot{e}_{ij} - \frac{D_j^-Q_j}{a}\right). \tag{2.39}$$

The right side of this equation is related to the specific entropy (entropy per unit mass) s by

$$\rho aT\frac{\partial s}{\partial t} = a\sum_{ij}\Sigma_{ij}\,\dot{e}_{ij} - \sum_j D_j^-Q_j. \tag{2.40}$$

This can be written as

$$\rho\frac{\partial s}{\partial t} = \sum_{ij}\Sigma_{ij}\,\frac{\dot{e}_{ij}}{T} - \sum_j\frac{1}{aT}\,D_j^-Q_j =$$

$$= \sum_{ij}\Sigma_{ij}\,\frac{\dot{e}_{ij}}{T} + \sum_j Q_j^-D_j^-\frac{1}{aT} - \sum_j D_j^-\frac{Q_j}{aT}, \tag{2.41}$$

and summing over all points, we find the entropy production:

$$a^3 \sum_{l,m,n} \left[\frac{\partial(\rho s)}{\partial t} + \sum_j D_j^- \frac{Q_j}{aT} \right] = \\ = \sum_{l,m,n} \left[\sum_{ij} a^3 \Sigma_{ij} \frac{\dot{e}_{ij}}{T} + \sum_j Q_j D_j^+ \frac{a^2}{T} \right]. \qquad (2.42)$$

This means that the generalized forces associated to the generalized velocities Σ_{ij} and Q_j are $-a^3 \dot{e}_{ij}/T$ and $-a^2 D_j^+(1/T)$, respectively. Eqs. $\Sigma_{ij} = \eta_{ijlm}\dot{e}_{lm}$ and $Q_i = (T^2/a)\kappa_{ij} D_j^+(1/T)$ then imply that the kinetic coefficients associated to Σ_{ij} and Q_j are $k_B T \eta_{ijlm}/a^3$ and $k_B T^2 \kappa_{ij}/a^3$, respectively. Following Onsager's ideas as used in Fluctuating Hydrodynamics [40, 41, 42], we conclude that the equations of motion including thermoelastic effects, dissipation and zero-mean fluctuations are as follows

$$\rho a^2 \ddot{u}_i = \sum_j D_j^- [(\sigma_{ij} + \Sigma_{ij} + s_{ij})\, g'(D_j^+ u_i)], \qquad (2.43)$$

$$\langle s_{ij} \rangle = 0,$$

$$\langle s_{ij}(l,m,n;t) s_{ab}(l',m',n';t') \rangle = \\ = k_B T \frac{\eta_{ijab} + \eta_{abij}}{a^3} \delta_{ll'} \delta_{mm'} \delta_{nn'} \delta(t-t'), \qquad (2.44)$$

$$\rho c\, \dot{T} + T \sum_{ij} \alpha_{ij} g'(D_j^+ u_i)\, D_j^+ \dot{u}_i = -\frac{1}{a} \sum_i D_i^- (Q_i + \xi_i), \qquad (2.45)$$

$$\langle \xi_i \rangle = 0,$$

$$\langle \xi_i(l,m,n;t) \xi_j(l',m',n';t') \rangle = \\ = k_B T^2 \, \frac{\kappa_{ij} + \kappa_{ji}}{a^3} \, \delta_{ll'} \delta_{mm'} \delta_{nn'} \, \delta(t-t'), \qquad (2.46)$$

with σ_{ij} given by (2.34). In principle, fluctuations can be included in boundary conditions by using the nonequilibrium fluctuating hydrodynamics formalism as explained in [46] and in [47] for the case of semiconductor interfaces. In crystals with cubic symmetry, the elastic constants and the viscosity tensor are given by Eqs. (2.5) and (2.24), respectively. The thermal conductivity and thermal expansion tensors are isotropic, $\kappa_{ij} = \kappa \delta_{ij}$, $\alpha_{ij} = \alpha \delta_{ij}$. Note that the correlations of s_{ij} in (2.44) and of ξ_i in (2.46) are proportional to $1/a^3$, which becomes $\delta(\mathbf{x} - \mathbf{x}')$ in the continuum limit as $a \to 0$.

Note that in our model, dissipation and fluctuations affect all atoms of the cubic lattice although we would expect from phys-

ical considerations that dissipation and fluctuations should be more pronounced near the core of moving dislocations, as they are directly related to the motion of the atomic constituents in the core vicinity. However our model should also fulfill these expectations. Why? Dissipation is described by a Rayleigh dissipative function that is a quadratic functional of the strain rate tensor, which, in turn, depends on the discrete distorsion tensor. Since the distortion tensor (containing finite differences of the displacement vector) and its rate are larger near the core of defects, we expect that dissipation will be stronger near the core of a moving dislocation than at its far field. Fluctuations are introduced via the fluctuation-dissipation theorem and they should also be stronger near the core of moving dislocations.

2.5 MODELS OF FCC AND BCC CRYSTALS WITH ONE ATOM PER LATTICE SITE

In this Section, we explain how to extend our discrete models of dislocations to fcc or bcc crystal symmetry, assuming that we have one atom per lattice site [33]. For fcc or bcc crystals, the primitive vectors of the unit cell are not orthogonal. To find a discrete model for these crystals, we should start by writing the strain energy density in a non-orthogonal vector basis, a_1, a_2, a_3, instead of the usual orthonormal vector basis e_1, e_2, e_3 determined by the cube sides. Let x_i denote coordinates in the basis e_i, and let x'_i denote coordinates in the basis a_i. Notice that the x_i have dimensions of length while the x'_i are dimensionless. The matrix $\mathcal{T} = (a_1, a_2, a_3)$ whose columns are the coordinates of the new basis vectors in terms of the old orthonormal basis can be used to change coordinates as follows:

$$x'_i = \mathcal{T}^{-1}_{ij} x_j, \; x_i = \mathcal{T}_{ij} x'_j. \tag{2.47}$$

Similarly, the displacement vectors in both basis are related by

$$u'_i = \mathcal{T}^{-1}_{ij} \tilde{u}_j, \; \tilde{u}_i = \mathcal{T}_{ij} u'_j, \tag{2.48}$$

and partial derivatives obey

$$\frac{\partial}{\partial x'_i} = \mathcal{T}_{ji} \frac{\partial}{\partial x_j}, \; \frac{\partial}{\partial x_i} = \mathcal{T}^{-1}_{ji} \frac{\partial}{\partial x'_j}. \tag{2.49}$$

Note that u'_i and x'_i are nondimensional while $\tilde{u}_i$ and x_i have dimensions of length. By using these equations, the strain energy density $W = (1/2)c_{iklm}e_{ik}e_{lm}$ can be written as

$$W = \frac{1}{2}\, c_{ijlm}\frac{\partial \tilde{u}_i}{\partial x_j}\frac{\partial \tilde{u}_l}{\partial x_m} = \frac{1}{2}\, c'_{rspq}\frac{\partial u'_r}{\partial x'_s}\frac{\partial u'_p}{\partial x'_q}, \tag{2.50}$$

where the new elastic constants are:

$$c'_{rspq} = c_{ijlm}\mathcal{T}_{ir}\mathcal{T}^{-1}_{sj}\mathcal{T}_{lp}\mathcal{T}^{-1}_{qm}. \tag{2.51}$$

Notice that the elastic constants have the same dimensions in both the orthogonal and the non-orthogonal basis. To obtain a discrete model, we shall consider that the dimensionless displacement vector u'_i depends on dimensionless coordinates x'_i that are integer numbers $u'_i = u'_i(l, m, n; t)$. As in Section 2.3, we replace the distortion tensor (gradient of the displacement vector in the non-orthogonal basis) by a periodic function of the corresponding forward difference, $w_i^{(j)} = g(D_j^+ u'_i)$. As in Eq. (2.12), g is a periodic function with $g'(0) = 1$ and period 1. The discretized strain energy density is

$$W(l, m, n; t) = \frac{1}{2}\, c'_{rspq} g(D_s^+ u'_r)\, g(D_q^+ u'_p). \tag{2.52}$$

The elastic constants c'_{rspq} in (2.51) can be calculated in terms of the Voigt stiffness constants for a cubic crystal, C_{11}, C_{44} and C_{12}, which determine the tensor of elastic constants (2.5). The elastic energy can be obtained from Eq. (2.52) for W by means of Eqs. (2.8). Then the conservative equations of motion (2.9) are

$$\rho a^3 \frac{\partial^2 u'_i}{\partial t^2} = -\mathcal{T}^{-1}_{iq}\mathcal{T}^{-1}_{pq}\frac{\partial V}{\partial u'_p},$$

which, together with Eqs. (2.8) and (2.52), yield

$$\rho\, \frac{\partial^2 u'_i}{\partial t^2} = \mathcal{T}^{-1}_{iq}\mathcal{T}^{-1}_{pq}\, D_j^- [g'(D_j^+ u'_p)\, c'_{pjrs}\, g(D_s^+ u'_r)]. \tag{2.53}$$

This equation becomes (2.10) for orthogonal coordinates, $\mathcal{T}_{iq}^{-1} = \delta_{iq}/a$.

To add dissipation and fluctuations to these equations, we need to replace $c'_{pjrs}g(D_s^+u'_r)$ by $c'_{pjrs}g(D_s^+u'_r) - \alpha'_{pj}(T - T_0) + \eta'_{pjrs}g'(D_s^+u'_r)\, D_s^+\dot{u}'_r + s'_{pj}$, in which η'_{pjrs} is related to the viscosity tensor (2.24) in the same way as c'_{pjrs} is related to c_{ijlm} by (2.51). The random stress tensor s'_{pj} has zero mean and correlation given by (2.44) with the modified viscosity tensor η'_{ijab} instead of the viscosity tensor (2.24). The heat conduction equations are

$$\rho c\,\frac{\partial T}{\partial t} + T\,\alpha'_{ij}g'(D_j^+u'_i)\,D_j^+\frac{\partial u'_i}{\partial t} = \\ = D_i^-\left(\kappa'_{ij}D_j^+T + \frac{\xi'_i}{a}\right), \tag{2.54}$$

$$\langle\xi'_i\rangle = 0,$$

$$\langle\xi'_i(l,m,n;t)\xi'_j(l',m',n';t')\rangle = \\ = k_BT^2\,\frac{\kappa'_{ij}+\kappa'_{ji}}{a}\,\delta_{ll'}\delta_{mm'}\delta_{nn'}\,\delta(t-t'), \tag{2.55}$$

$$\kappa'_{pq} = \mathcal{T}_{pi}^{-1}\mathcal{T}_{qj}^{-1}\kappa_{ij}, \tag{2.56}$$

$$\alpha'_{pq} = \frac{1}{2}\left(\mathcal{T}_{ip}\mathcal{T}_{qj}^{-1} + \mathcal{T}_{jp}\mathcal{T}_{qi}^{-1}\right)\alpha_{ij}. \tag{2.57}$$

Note that the both the original and the modified tensors α_{ij} and κ_{ij} are symmetric.

Once we have derived the equations of motion, stationary dislocations can be calculated by first finding the corresponding solution to the equations of anisotropic elasticity and using it to set up initial and boundary conditions for overdamped equations of motion. For fcc and bcc crystals, screw and edge dislocations have been constructed in Ref. [33].

2.6 MODELS FOR DIAMOND AND ZINCBLENDE STRUCTURES

Silicon and gallium arsenide are semiconductors of great importance for industry that crystalize in the face centered cubic (fcc) system. Crystals of these materials can be described as a fcc Bravais lattice with a basis of two atoms per site, which constitute a diamond structure for Si and a zincblende structure for GaAs

[48]. When growing layers of these materials, defects are very important because they act as nucleation sites, and have to be eliminated after the growth process has ceased. Among defects, dislocations and misfit dislocations are often observed [49, 11]. Thus, it is desirable to have an economic description of these defects and their dynamics in terms of control parameters such as temperature [50]. A molecular dynamics description is very costly if we need to couple atomic details in the nanoscale to a mesoscopic description in larger scales that are important in the growth process [51]. In this Section, we extend the previous models for cubic crystals with an atom per lattice site to crystals having two atoms per site (extension to crystals with more than two atoms per site is straightforward). Having two or more atoms per site introduces new features that are better explained revisiting the classic Born-von Karman work on vibrations of a linear diatomic chain [52]. We shall show how to obtain the wave equation for acoustic phonons in the elastic limit, directly from the equations for the diatomic chain. A similar calculation allows us in Subsection 2.6.2 to obtain the Cauchy equations for anisotropic elasticity in the continuum limit of our discrete models, which are constructed with the aim of having exactly this property. Subsection 2.6.3 shows how to calculate static dislocations for GaAs and Si.

2.6.1 *Continuum limit for the linear diatomic chain*

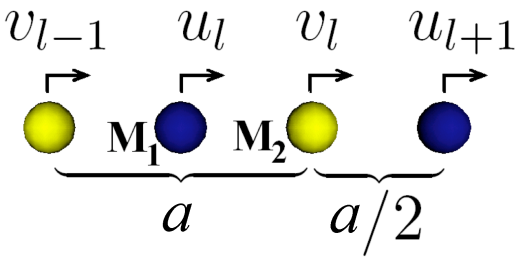

Figure 2. Linear diatomic chain comprising alternatively atoms of masses M_1 and M_2 whose equilibrium positions are separated a distance $a/2$.

We shall consider a diatomic chain comprising alternatively atoms of masses M_1 and M_2 whose equilibrium positions are

separated a distance $a/2$. The atoms are restricted to move only along the length of the chain. Their displacement with respect to their equilibrium positions will be denoted by $a\,u_l$ and $a\,v_l$, respectively, in which l is the cell index, and u_l and v_l are dimensionless. If ϕ is the quadratic potential of interaction between neighboring atoms, the equations of motion for the diatomic chain are [52]

$$\begin{aligned} M_1\ddot{u}_l &= \frac{1}{a}\Big[\phi'\big((v_l-u_l)\,a+a/2\big) \\ &\qquad -\phi'\big((u_l-v_{l-1})\,a+a/2\big)\Big] = \\ &= \phi''\,(a/2)\;[(v_l-u_l)-(u_l-v_{l-1})], \qquad (2.58) \\ M_2\ddot{v}_l &= \frac{1}{a}\Big[\phi'\big((u_{l+1}-v_l)\,a+a/2\big) \\ &\qquad -\phi'\big((v_l-u_l)\,a+a/2\big)\Big] = \\ &= \phi''\,(a/2)\;[(u_{l+1}-v_l)-(v_l-u_l)]. \qquad (2.59) \end{aligned}$$

If we assume that the solutions of these equations are plane waves,

$$u_l = U\,e^{i\,(2\pi\eta l-\omega t)}, \qquad v_l = V\,e^{i\,(2\pi\eta l-\omega t)}, \qquad (2.60)$$

the following dispersion relation is obtained

$$\omega^2 = \frac{\phi''(a/2)}{M_1M_2}\left[(M_1+M_2)\mp \mp\sqrt{(M_1+M_2)^2-4M_1M_2\sin^2\pi\eta}\right], \qquad (2.61)$$

in which the minus (resp., plus) sign corresponds to the acoustic (resp., optic) branch of the dispersion relation [52]. Moreover, the corresponding amplitude ratio for the acoustic branch is

$$\frac{U}{V} = \frac{-M_2\,(1+e^{-i\,2\pi\eta})}{(M_1-M_2)-\sqrt{(M_1+M_2)^2-4M_1M_2\sin^2\pi\eta}}, \qquad (2.62)$$

with a similar formula for the optical branch [52]. In the long wavelength limit, $\eta \to 0$, the acoustic vibrations satisfy

$$U = V, \quad \omega = c\,\frac{2\pi\eta}{a}, \tag{2.63}$$

$$c = \sqrt{\frac{\phi''(a/2)\,a^2}{2\,(M_1+M_2)}} = \sqrt{\frac{E}{\rho}}, \tag{2.64}$$

$$\rho = \frac{M_1+M_2}{a}, \quad E = \frac{\phi''(a/2)\,a}{2}. \tag{2.65}$$

In these equations, E and ρ are the Young modulus and the linear mass density, respectively [52]. In the limit as $\eta \to 0$, each cell comprising two atoms moves rigidly with a phase velocity c and a wave number $2\pi\eta/a$.

The continuum limit of the diatomic chain equations recovers the acoustic vibrations only. In this limit, $l \to \infty$ and $a \to 0$, with fixed $x = la$. Furthermore,

$$a\,u_l(t) = \tilde{u}(la,t) = \tilde{u}(x,t), \tag{2.66}$$

$$a\,v_l(t) = \tilde{u}\left(la+\tfrac{a}{2},t\right) = \tilde{u}\left(x+\frac{a}{2},t\right). \tag{2.67}$$

If we now add Eqs. (2.58) and (2.59) divide by a, and use (2.67) to approximate the result, we obtain the following wave equation in the continuum limit:

$$\rho\,\frac{\partial^2\tilde{u}}{\partial t^2} = E\,\frac{\partial^2\tilde{u}}{\partial x^2}, \tag{2.68}$$

provided ρ and E are given by Eq. (2.65). The wave speed c is then given by Eq. (2.64). Equation (2.68) is the elastic continuum limit of the diatomic chain equations, *which does not contain optical vibrations*.

2.6.2 *Discrete model for a fcc lattice with a two-atom basis*

We shall now propose a discrete model for a fcc lattice with a basis comprising two atoms, of masses M_1 and M_2, respectively.

Although this model is much more complicated to describe, the key ideas to show that it is compatible with anisotropic elasticity are the same as in Subsection 2.6.1 for the diatomic chain.

The main ideas needed to write a model for this crystal structure are the following:

1. Write the strain energy corresponding to a fcc crystal in a non-orthogonal basis with axes given by the usual primitive directions of the fcc Bravais lattice.
2. Write the corresponding strain energy for a fcc crystal with two atoms per lattice site.
3. Restore the periodicity of the crystal by defining the discrete distortion tensor as a periodic function (with period 1) of the discrete gradient of the displacement vector.
4. Define the potential energy of the crystal as the strain energy times the volume of the unit cell summed over all lattice sites. Then write down the equations of motion for the displacement vectors at each site.
5. Check that the continuum limit of the model yields the usual anisotropic elasticity.

We shall now carry out this program, which is an extension of that presented in Section 2.5 for a fcc lattice with a single atom per site; see also Ref. [33]. The primitive vectors of the fcc lattice are

$$a_1 = \frac{a}{2}(0,1,1), \quad a_2 = \frac{a}{2}(1,0,1), \quad a_3 = \frac{a}{2}(1,1,0), \quad (2.69)$$

in terms of the usual orthonormal vector basis e_1, e_2, e_3 determined by the cube. From these vectors, we determine the matrix $\mathcal{T}_{ij}$ to change coordinates as in (2.47) and (2.48). In the continuum limit, the strain energy is given by (2.50) with elastic constants given by (2.51) and (2.5).

Once we have written the strain energy of a fcc crystal in the non-orthogonal basis spanned by the primitive vectors, we

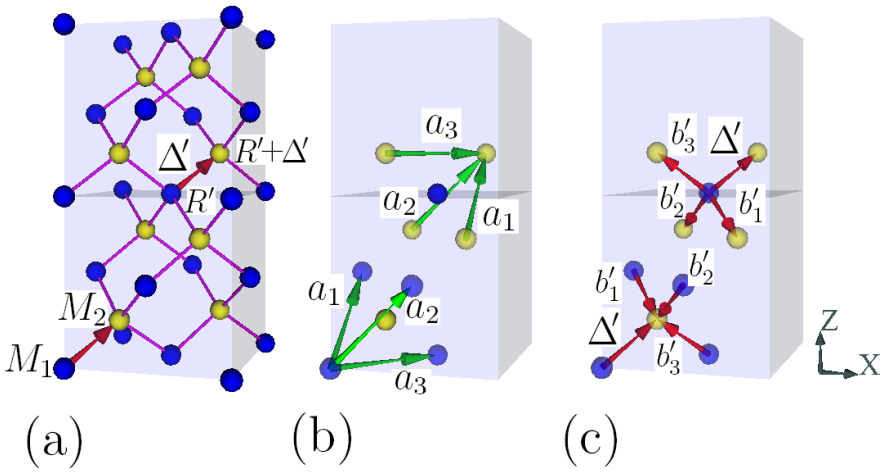

Figure 3. Relevant vectors joining lattice points that are needed to discretize the displacement field in a zincblende lattice. All coordinates are expressed in the non-orthogonal basis spanned by the primitive vectors a_1, a_2, and a_3. (a) The basis of a unit cell placed at $R' = (l, m, n)$ comprises one atom of mass M_1 with displacement vector $u'_i(R'; t)$ and one atom of mass M_2 and displacement vector $v'_i(R' + \Delta'; t)$. (b) Discrete gradients involving lattice points closest to R' (resp. $R' + \Delta'$) are backward differences from $R' + \Delta'$ (resp., forward differences from R') along the primitive directions: $D_j^- v'_i(R' + \Delta'; t)$, (resp., $D_j^+ u'_i(R'; t)$), $i, j = 1, 2, 3$. (c) The auxiliary vectors b'_i satisfy $a'_i + b'_i = \Delta'$, $i = 1, 2, 3$.

can introduce our discrete model. We shall consider a fcc lattice with a two-atom basis. In equilibrium, atoms with mass M_1 will be placed at the lattice sites, so that their displacement vectors will depend on integer numbers and time: $u'_i = u'_i(l, m, n; t)$. In equilibrium, atoms with mass M_2 will be placed at the sites of a fcc lattice which, in the orthonormal basis e_i, is rigidly displaced by a vector $\Delta = (a/4, a/4, a/4)$ with respect to the first fcc lattice; see Fig. 8. In terms of the non-orthogonal basis a_i, the vector $(a/4, a/4, a/4)$ becomes $\Delta' = (1/4, 1/4, 1/4)$.

We should define discrete differences of a displacement vector so that a discrete difference become the corresponding partial derivative in the continuum limit. This requirement can be satisfied in more than one way using different neighbors of a given

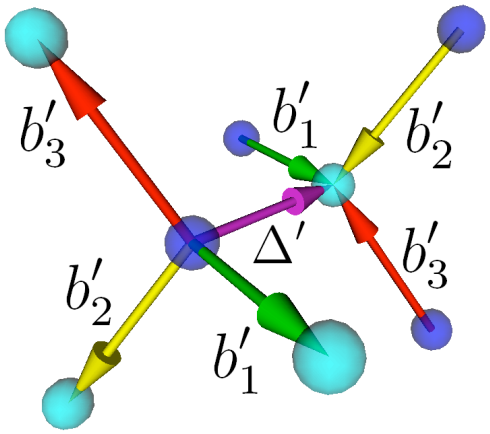

Figure 4. Another perspective in a zincblende lattice in which vectors b'_i and Δ' are shown. Only some atoms are depicted. $a'_i + b'_i = \Delta'$.

lattice point. We shall select only two neighbors of a lattice point for this purpose, using that the nearest neighbors of an atom with mass M_1 are atoms with mass M_2 and viceversa. Fig. 8 shows that each atom with mass M_1 (resp., M_2) is linked to its four nearest neighbors having mass M_2 (resp., M_1) by Δ', $b'_i = \Delta' - a'_i$ (resp., $-\Delta'$, $-b'_i$). Thus the nearest neighbors of an atom with displacement vector $v'_i(R' + \Delta'; t)$ have displacement vectors $u'_i(R'; t)$ and $u'_i(R' + a'_j; t)$, with $j = 1, 2, 3$, and the nearest neighbors of an atom with displacement vector $u'_i(R'; t)$ have displacement vectors $v'_i(R' + \Delta'; t)$ and $v'_i(R' + \Delta' - a'_j; t)$, with $j = 1, 2, 3$. These facts motivate our definition of discrete differences of a displacement vector. See also Fig. 4.

Let us define the standard forward and backward difference operators along the primitive directions as

$$D_j^{\pm} f(R') = \pm[f(R' \pm a'_j) - f(R')]. \tag{2.70}$$

Then $\Omega_{ij}^{(2)}(R' + \Delta'; t) = D_j^{+} u'_i(R'; t)$ is the discrete gradient of the displacement vector $v'_i(R' + \Delta'; t)$ which involves lattice points closest to $R' + \Delta'$, whereas $\Omega_{ij}^{(1)}(R'; t) = D_j^{-} v'_i(R' + \Delta'; t)$ is the discrete gradient of the displacement vector $u'_i(R'; t)$ which involves lattice points closest to R'. The distortion tensor of our discrete model at the cell R' could be defined as a weighted

average of $g(\Omega_{ij}^{(1)})$ and $g(\Omega_{ij}^{(2)})$, in which $g(x)$ is a period-one periodic function such that $g(x) \sim x$ as $x \to 0$. For simplicity, we shall adopt equal weights in our definition:

$$w_i^{(j)}(R';t) = \frac{g\left(D_j^+ u_i'(R';t)\right) + g\left(D_j^- v_i'(R'+\Delta';t)\right)}{2}. \quad (2.71)$$

Obviously, this is reasonable for materials such as Si having a diamond structure, and also in the case of atoms of similar size for materials with zincblende structure. In the continuum limit $a \to 0$, the distortion tensor tends to the gradient of the displacement vector:

$$w_i^{(j)} \sim \frac{\partial \tilde{u}_i'}{\partial x_j'}. \quad (2.72)$$

In practice, the period-one function g should be fitted to experimental or molecular dynamics data, such as the Peierls stress needed for a dislocation to move; see Fig. 1 of Ref. [33] for the variation of the Peierls stress as a function of the parameter controlling the shape of a piecewise linear function g. The positive potential energy of the crystal will therefore be

$$V = \frac{a^3}{4} \sum_{l,m,n} \frac{1}{8} c'_{rspq} [g(D_s^+ u_r') + g(D_s^- v_r')] \, [g(D_q^+ u_p') + g(D_q^- v_p')]. \quad (2.73)$$

Here $a^3/4$ is the volume spanned by the three primitive vectors.

The conservative equations of motion are

$$M_1 \frac{\partial^2 u_i'}{\partial t^2} = -\mathcal{T}_{iq}^{-1} \mathcal{T}_{pq}^{-1} \frac{\partial V}{\partial u_p'}. \quad (2.74)$$

$$M_2 \frac{\partial^2 v_i'}{\partial t^2} = -\mathcal{T}_{iq}^{-1} \mathcal{T}_{pq}^{-1} \frac{\partial V}{\partial v_p'}. \quad (2.75)$$

Using Eq. (2.73), these equations become

$$\frac{4M_1}{a^3}\frac{\partial^2 u_i'}{\partial t^2} = \\ = \frac{1}{4}\mathcal{T}_{iq}^{-1}\mathcal{T}_{pq}^{-1}D_j^-\{c'_{pjrs}\,g'(D_j^+u_p')\,[g(D_s^-v_r') + g(D_s^+u_r')]\}, \quad (2.76)$$

$$\frac{4M_2}{a^3}\frac{\partial^2 v_i'}{\partial t^2} = \\ = \frac{1}{4}\mathcal{T}_{iq}^{-1}\mathcal{T}_{pq}^{-1}D_j^+\{c'_{pjrs}\,g'(D_j^-v_p')\,[g(D_s^+u_r') + g(D_s^-v_r')]\}. \quad (2.77)$$

If $M_1 = M_2$ (the case of Si), this system of equations is invariant under the symmetry: $u_i'(R') \leftrightarrow -v_i'(R' + \Delta')$. To obtain the continuum limit, we add Eqs. (2.76) and (2.77), take into account the continuum limit (2.72), and use Eqs. (2.47) to revert to the dimensional orthogonal coordinates. Then the resulting equations are those of anisotropic elasticity:

$$\rho\,\frac{\partial^2\tilde{u}_i}{\partial t^2} \;=\; \frac{\partial}{\partial x_j}\left(c_{ijrs}\,\frac{\partial\tilde{u}_r}{\partial x_s}\right). \quad (2.78)$$

In this equation, the mass density ρ is the sum of the masses in the primitive cell divided by the volume thereof:

$$\rho = \frac{M_1 + M_2}{a^3/4}. \quad (2.79)$$

Fluctuations and dissipation can be added to these equations in the same way as for the models with one-atom basis. The derivation of these equations in non-orthogonal coordinates follows those in Sections 2.3 and 2.4, but using the following energy instead of (2.30):

$$\frac{d}{dt}\sum_{l,m,n}\left[\sum_i\frac{\rho}{2}\left(\sum_j\mathcal{T}_{ij}\dot{u}_j'\right)^2 + \sum_{rspq}\frac{1}{2}c'_{rspq}g(D_s^+u_r')\,g(D_q^+u_p')\right] = \\ = \sum_{l,m,n}\sum_{i,j}\dot{u}_i'\,D_j^-\,[\Sigma'_{ij}\,g'(D_j^+u_i')]. \quad (2.80)$$

In particular, (2.42) also holds in non-orthogonal coordinates, which then yields the same formulas for the fluctuations as in orthogonal coordinates. For a zincblende structure, the governing equations including dissipation and fluctuations are:

$$\rho c\,\frac{\partial T}{\partial t} + \frac{T}{2}\alpha'_{ij}\left(g'(D_j^+ u'_i)\,D_j^+\frac{\partial u'_i}{\partial t} + g'(D_j^- v'_i)\,D_j^-\frac{\partial v'_i}{\partial t}\right) = \\ = D_i^-\left(\kappa'_{ij}D_j^+ T + \frac{\xi'_i}{a}\right), \quad (2.81)$$

$$\langle \xi'_i\rangle = 0,$$

$$\langle \xi'_i(l,m,n;t)\xi'_j(l',m',n';t')\rangle = \quad (2.82)$$

$$= k_B T^2\,\frac{\kappa'_{ij}+\kappa'_{ji}}{a}\,\delta_{ll'}\delta_{mm'}\delta_{nn'}\,\delta(t-t'), \quad (2.83)$$

$$\frac{4M_1}{a^3}\,\frac{\partial^2 u'_i}{\partial t^2} = \frac{1}{2}\,\mathcal{T}_{iq}^{-1}\mathcal{T}_{pq}^{-1}D_j^-\{[\sigma'_{pj}+\Sigma'_{pj}+s'_{pj}]\,g'(D_j^+u'_p)\}, \quad (2.84)$$

$$\frac{4M_2}{a^3}\,\frac{\partial^2 v'_i}{\partial t^2} = \frac{1}{2}\,\mathcal{T}_{iq}^{-1}\mathcal{T}_{pq}^{-1}D_j^+\{[\sigma'_{pj}+\Sigma'_{pj}+s'_{pj}]\,g'(D_j^-v'_p)\}, \quad (2.85)$$

$$\langle s'_{ij}\rangle = 0,$$

$$\langle s'_{ij}(l,m,n;t)s'_{ab}(l',m',n';t')\rangle = \\ = k_B T\frac{\eta'_{ijab}+\eta'_{abij}}{a^3}\delta_{ll'}\delta_{mm'}\delta_{nn'}\,\delta(t-t'), \quad (2.86)$$

$$\sigma'_{pj} = c'_{pjab}e'_{ab} - \alpha'_{pj}(T-T_0), \quad \Sigma'_{pj} = \eta'_{pjab}\dot{e}'_{ab}, \quad (2.87)$$

together with (2.57). In these equations, $e'_{ab} = (w_a^{(b)} + w_b^{(a)})/2$ is the symmetric part of the distortion tensor (2.71).

2.6.3 *Dislocations in Si and GaAs*

Si and GaAs crystals are face-centred cubic with two atoms per lattice site, one at $(0,0,0)$ and the other one at $\Delta = (1/4,1/4,1/4)$. Both atoms are identical in Si (diamond structure), whereas they are different in GaAs: one atom is gallium and the other arsenic (zincblende structure). Each atom is tetrahedrally bonded to four nearest-neighbors, and the shortest lattice vector $\langle 110\rangle/2$ links a second neighbor pair, as shown in Figure 9. The covalent bond between two atoms is strongly localized and directional, and this feature strongly affects the characteristics of dislocations. In turn, dislocations influence both mechanical and electrical properties

of these semiconductors [11, 14]. In this Section, we shall construct straight dislocations for Si and GaAs using their elastic stiffnesses and a method for calculating their strain field.

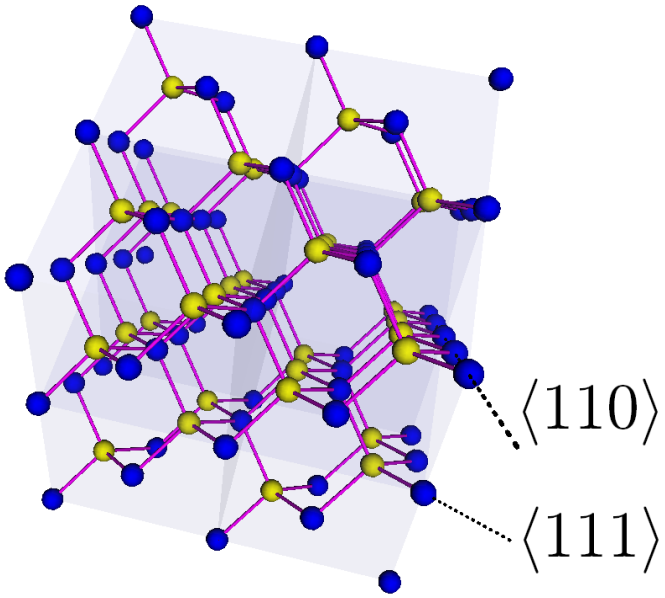

Figure 5. Relevant directions in a fcc lattice with a two-atom basis.

Perfect dislocations have Burgers vectors $\mathbf{b} = \langle 110 \rangle / 2$ (the same as in the case of fcc lattices with a one-atom basis) and slip on the close packed $\{111\}$ planes having normal vector $\mathbf{n}$. Their dislocation line vectors ¸ usually lie along $\langle 110 \rangle$ directions, forming 60° (perfect 60° dislocations) or 0° (perfect screw dislocations) with respect to the Burgers vector.

We will now construct a perfect screw and a perfect 60° dislocation for GaAs lattice, both having Burgers vector $\mathbf{b} = (1, 0, 1)/2$. Gliding dislocations having this Burgers vector will leave behind a perfect crystal, since it is a primitive vector of the lattice [11]. For Si the same construction can be used.

The tensor of elastic constants is given by (2.5) in terms of the Voigt elastic stiffnesses C_{ij} and the degree of anisotropy H of (2.6). We use the following values of the Voigt stiffnesses measured in

units of 10^9Pa at room temperature ($T = 298$ K) [53]:

$$C_{11} = 165.6, \quad C_{12} = 63.98, \quad C_{44} = 79.51, \quad \text{for Si;} \tag{2.88}$$
$$C_{11} = 118.8, \quad C_{12} = 53.8, \quad C_{44} = 58.9, \quad \text{for GaAs.} \tag{2.89}$$

Between 200 K and 800 K, these constants decrease linearly with increasing temperature, so that $-C_{ij}^{-1}\, dC_{ij}/dT \approx 10^{-4}\text{K}^{-1}$, $i, j = 1, 2, 3$, [54, 55, 56]. Such small corrections could be straightforwardly included in our calculations, modifying minimally our results.

To calculate the elastic far field of any stationary straight dislocation, we shall follow the method explained in Chapter 13 of Hirth and Lothe's book [14]. Firstly, we determine an orthonormal coordinate system e_1'', e_2'', e_3'' with $e_3'' = -\xi$ parallel to the dislocation line and $e_2'' = \mathbf{n}$ being the unitary vector normal to the glide plane. In terms of the new basis, the elastic displacement field (u_1'', u_2'', u_3'') depends only on x_1'' and on x_2''.

Secondly, we calculate the elastic constants in the reference system e_1'', e_2'', e_3'':

$$c''_{ijkl} = c_{ijkl} - H \sum_{n=1}^{3} (S_{in} S_{jn} S_{kn} S_{ln} - \delta_{in}\delta_{jn}\delta_{kn}\delta_{ln}). \tag{2.90}$$

Here the rows of the orthogonal matrix $S = (e_1'', e_2'', e_3'')^t$ are the coordinates of the e_i'''s in the old orthonormal basis e_1, e_2, e_3. In the new reference system, the Burgers vector has coordinates $(\mathrm{b}_1'', \mathrm{b}_2'', \mathrm{b}_3'')$.

Thirdly, the displacement vector (u_1'', u_2'', u_3'') is calculated as follows:

- Select three roots p_1, p_2, p_3 with positive imaginary part out of each pair of complex conjugate roots of the polynomial $\det[a_{ik}(p)] = 0$, $a_{ik}(p) = c''_{i1k1} + (c''_{i1k2} + c''_{i2k1})p + c''_{i2k2}p^2$.
- For each $n = 1, 2, 3$ find an eigenvector $A_k(n)$ associated to the zero eigenvalue for the matrix $a_{ik}(p_n)$.
- Solve $\mathrm{Re}\sum_{n=1}^{3} A_i(n)D(n) = \mathrm{b}_i''$, and $\mathrm{Re}\sum_{n=1}^{3}\sum_{k=1}^{3}(c''_{i2k1} + c''_{i2k2}p_n)A_k(n)D(n) = 0$, in which $i = 1, 2, 3$, for the imaginary and real parts of $D(1)$,$D(2)$,$D(3)$.

- For $k = 1, 2, 3$, $u''_k = \mathrm{Re}[-\frac{1}{2\pi i}\sum_{n=1}^{3} A_k(n) D(n) \ln(x''_1 + p_n x''_2)]$.

Lastly, we can calculate the displacement vector u'_k in the non-orthogonal basis a_i from u''_k.

For the perfect 60° dislocation, we have

$$e''_1 = \frac{1}{\sqrt{6}}(1, 1, 2), \tag{2.91}$$
$$e''_2 = \frac{1}{\sqrt{3}}(-1, -1, 1), \tag{2.92}$$
$$e''_3 = \frac{1}{\sqrt{2}}(-1, 1, 0), \tag{2.93}$$

and the resulting dislocation is depicted in Fig. 6.

For the pure screw dislocation, we have

$$e''_1 = \frac{1}{\sqrt{6}}(-1, -2, 1), \tag{2.94}$$
$$e''_2 = \frac{1}{\sqrt{3}}(-1, 1, 1), \tag{2.95}$$
$$e''_3 = \frac{1}{\sqrt{2}}(-1, 0, -1), \tag{2.96}$$

and the resulting dislocation can be observed in Fig. 7.

2.7 CONCLUSIONS

We have proposed discrete models describing defects in crystal structures whose continuum limit is the standard linear anisotropic elasticity. The main ingredients entering the models are the elastic stiffness constants of the material and a dimensionless periodic function that restores the translation invariance of the crystal (and together with the elastic constants determines the dislocation size). For simple cubic crystals, their equations of motion with conservative or damped dynamics (including fluctuations

according as in Fluctuating Hydrodynamics) are derived. For fcc and bcc metals, the primitive vectors along which the crystal is translationally invariant are not orthogonal. Similar discrete models and equations of motion are found by writing the strain energy density and the equations of motion in non-orthogonal coordinates. In these later cases, we can determine numerically stationary perfect edge and screw dislocations. We have also extended our discrete models to the case of fcc lattices with a two-atom basis, which includes important applications such as Si and GaAs crystals. For GaAs, we have calculated numerically two perfect dislocations which may be used to calculate the structure and motion of similar dislocations under stress as explained in Ref. [33]. Similarly to the case of the linear diatomic chain in which there are acoustic and optical branches of the dispersion relation, we expect that the dynamics of the discrete models with two-atom bases are richer than their continuum limits.

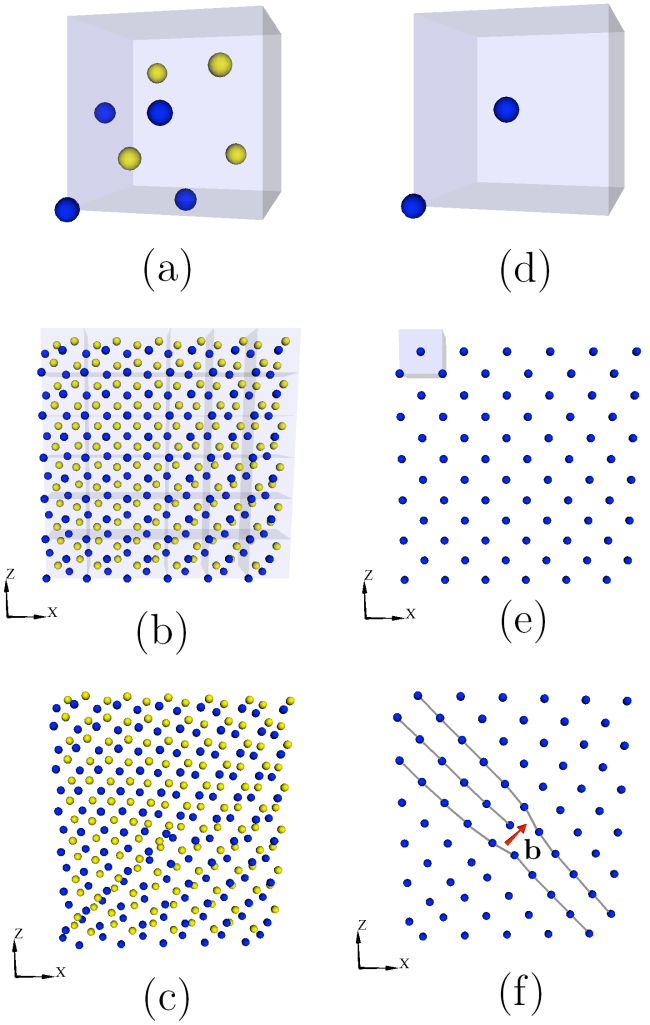

Figure 6. Displacement field in a GaAs lattice created by a perfect 60° dislocation of Burgers vector $\mathbf{b} = (1,0,1)/2$. (a) Reference cubic cell with its eight atoms. (b) One layer of a perfect undistorted lattice. (c) The same layer distorted by a perfect 60° dislocation. Panels (d), (e) and (f) correspond to (a), (b) and (c), respectively but we have depicted only two atoms per reference cubic cell.

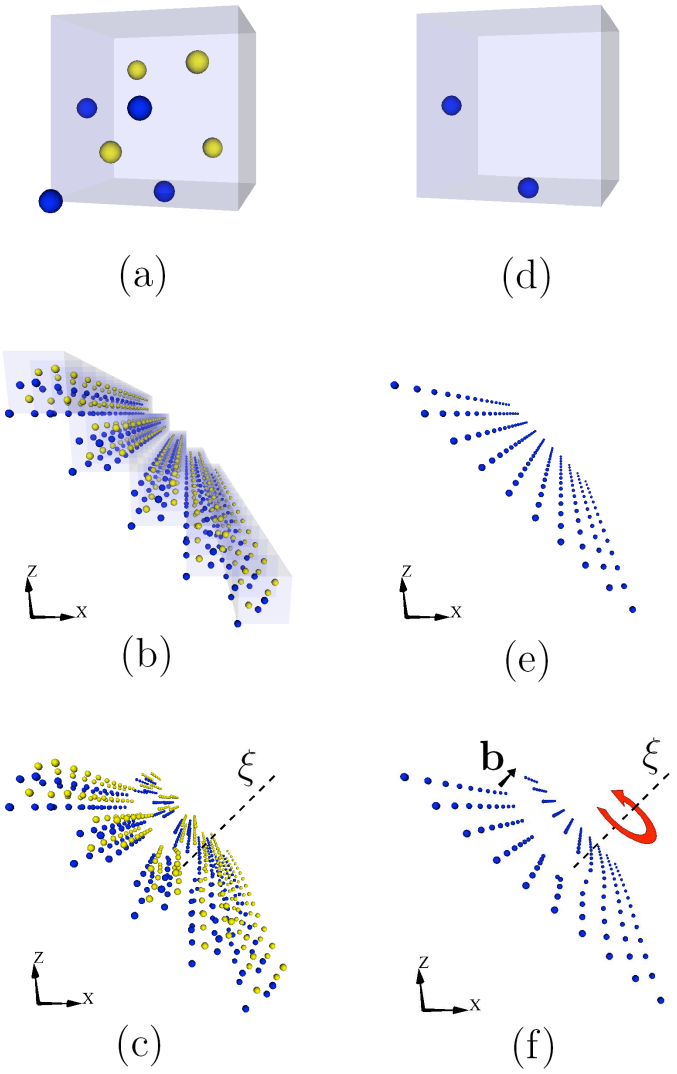

Figure 7. Displacement field in a GaAs lattice created by a perfect screw dislocation of Burgers vector $\mathbf{b} = (1,0,1)/2$. (a) Reference cubic cell with its eight atoms. (b) One layer of cubic cells normal to the Burgers vector for a perfect undistorted lattice. (c) The same layer distorted by a perfect screw dislocation. Panels (d), (e) and (f) correspond to (a), (b) and (c), respectively but we have depicted only two atoms per reference cubic cell.

3

A BIFURCATION ANALYSIS IN HOMOGENEOUS NUCLEATION

3.1 OUTLINE

When a two-dimensional crystal described by a dissipative discrete elasticity model is sheared beyond a critical stress $F = F_c$, the strained dislocation-free state becomes unstable via a subcritical pitchfork bifurcation. Numerical continuation shows that configurations containing two or four edge dislocations become simultaneously stable in appropriate stress ranges. Selecting a fixed final applied stress $F_f > F_c$, these stable configurations may be reached by setting $F = F_f t/t_r$ during different time intervals t_r. At a certain time after t_r, one or two dipoles are nucleated, split, and the resulting two edge dislocations move in opposite directions to the sample boundary. The critical stress for nucleation F_c is larger than the critical stress for dipole depinning. This explains why nucleated dipoles always split. In Sec. 3.2 we analyze the homogeneous nucleation of dislocation dipoles, whereas in Sec. 3.3 their splitting is studied.

3.2 HOMOGENEOUS NUCLEATION OF DISLOCATIONS AS BIFURCATIONS IN A DISCRETE ELASTICITY MODEL

3.2.1 *Introduction*

Homogeneous nucleation of dislocations is observed in different processes such as nanoindentation experiments [57, 58], heteroepitaxial crystal growth [59, 60] and indentation experiments in colloidal crystals [61] or soap bubble raft models [62]. Homogeneous nucleation of dislocations occurs in a perfect crystal and is therefore expected to have a much higher activation energy than heterogeneous nucleation at defect sites such as step

edges. Different types of calculations have been used to interpret homogeneous nucleation of dislocations in different situations, ranging from atomistic simulations to continuum mechanics interpretations or combinations thereof [6]. In all cases, a reliable nucleation criterion is needed to capture the nature of nucleated defects and the time and place at which such defects appear.

Experimental studies often use ad hoc criteria such as the critical resolved shear stress (CRSS) [57]. To use this criterion, the critical stress for nucleation has to be related to the applied force by other means, such as the Hertz contact theory in nanoindentation experiments [63, 57]. Moreover, the critical stress itself has to be calibrated independently and it cannot be a fixed value. Instead, the ideal shear stress for nucleation may depend strongly on the other stress components, not just on the shear stress component acting on the plane, as shown by density functional theory [64]. Zhu et al [5] use numerical simulations to argue that CRSS predicts nucleation of dislocations only in an approximate manner. However, some numerical simulations suggest that the CRSS is a reliable tool to predict motion of dislocations, but may not be reliable to predict nucleation. Instead, these authors minimize a scalar Λ formed by contracting a tensor $L_{ijkl} = C_{ijkl} + \tau_{il}\delta_{jk}$ with $w_i k_j w_k k_l$, where τ_{il} is the internal Cauchy stress and the plane wave $w_i e^{ik\cdot x}$ is assumed to be the local displacement vector. Minimization is done over all unit vectors w and k for each point of the computational domain. In turn, the elastic constants and the position dependent internal stress are calculated from atomistic simulations or from finite element calculations and the Cauchy-Born hypothesis to figure the motion of atoms [5]. Instability and nucleation according to the Λ criterion occur at those points at times at which Λ first vanishes.

While there is a widespread feeling that homogeneous nucleation of dislocations is related to some bifurcation occurring once the instability starts, no precise analysis and calculation of this bifurcation has been reported [5, 6]. In this letter, we tackle homogeneous nucleation of dislocations as a bifurcation problem in discrete elasticity. Discrete elasticity models of dislocations in cubic crystals [33, 34] describe dislocation cores in a natural way, their equations are asymptotic to the correct anisotropic elasticity far from defect cores and have been used to analyze dislocation depinning and motion at the Peierls stress in a precise manner [32].

3.2.2 *The model*

We consider a simple 2D discrete elasticity model that may describe homogeneous nucleation of edge dislocations and is amenable to detailed analysis. We consider a 2D simple cubic lattice with lattice constant normalized to 1, lattice points labelled by indexes (i, j), $i = 1, ..., N_x$ and $j = 1, ..., N_y$, and displacement vector $(u_{i,j}, 0, 0)$. At the boundary, a shear strain F is applied, so that the displacement $u_{i,j}$ for $j = 1, N_y$ and for $i = 1, N_x$ is $F\,[j - (N_y + 1)/2]$. When the system is homogeneously deformed, F is also the dimensionless shear stress. The components of the displacement vector in the y and z directions are ignored. $u_{i,j}$ obeys the following nondimensional equations:

$$m\frac{\partial^2 u_{i,j}}{\partial t^2} + \beta\frac{\partial u_{i,j}}{\partial t} = u_{i+1,j} - 2u_{i,j} + u_{i-1,j} + A\,[g_\alpha(u_{i,j+1} - u_{i,j}) + g_\alpha(u_{i,j-1} - u_{i,j})]. \tag{3.1}$$

Here $A = C_{44}/C_{11}$ for cubic crystals[1] with elastic constants C_{11}, C_{12}, C_{44}. Selecting a nondimensional time scale $C_{11}t/(\rho\gamma l^2) \to t$, we have $\beta = 1$, $\mu = C_{11}/(\rho l^2\gamma^2)$, where γ, ρ and l are a friction coefficient with units of frequency, the mass density and the dimensional lattice constant, respectively. The nondimensional displacement vector is measured in units of l. The overdamped case corresponds to $\mu = 0$. On the other hand, selecting a nondimensional time scale $C_{11}^{1/2}t/(l\rho^{1/2}) \to t$, we have $\mu = 1$, $\beta = l\gamma\sqrt{\rho/C_{11}}$. Then the conservative case corresponds to $\beta = 0$.

The nonlinear function g_α is periodic, with period equal to the space lattice and $g'_\alpha(0) = 1$. We have used in our simulations the continuous one-parameter family of periodic functions

$$g_\alpha(x) = \begin{cases} \frac{2\alpha}{\pi}\sin\left(\frac{\pi x}{2\alpha}\right), & \text{if } -\alpha \le x \le \alpha, \\ \frac{2\alpha}{\pi}\sin\left(\frac{\pi}{2}\frac{x-1/2}{\alpha-1/2}\right), & \text{if } \alpha \le x \le 1-\alpha, \end{cases} \tag{3.2}$$

with $0 < \alpha < 1/2$ and period 1. The parameter α controls the asymmetry of g_α, which in turn determines the size of the dislocation core and the Peierls stress needed for a dislocation to start

1 We have made numerical tests in the range $0.1 \le A \le 1$. For many cubic materials, $0.3 \le A \le 0.5$.

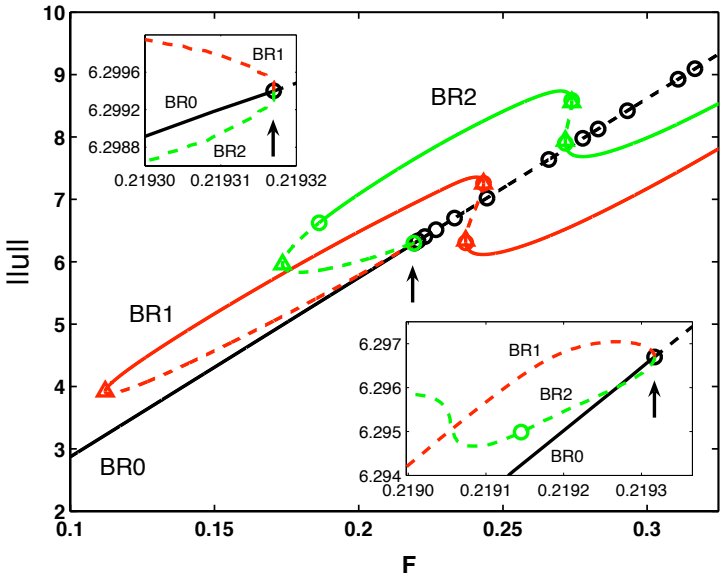

Figure 8. Bifurcation diagram showing only the primary stationary branches issuing from the homogeneous solution BR0. At F_c, branches BR1 and BR2 appear as a subcritical pitchfork bifurcation from BR0 (see the insets). In all cases, solid lines correspond to stable solutions, dashed lines to unstable solutions, limit points are marked as triangles and bifurcation points as circles.

moving [33] (See App. A). In the symmetric case $\alpha = 1/4$, (3.2) is the interacting atomic chains model [65], which is a simplification of the discrete elasticity models described in Ref. [33] and in Ch. 2 of this thesis.

3.2.3 *Results*

We consider the overdamped case, $m = 0$, $\beta = 1$ with $A = 0.3071$ (corresponding to tungsten), $\alpha = 0.2$. In the unstressed crystal configuration $F = 0$, a given initial condition evolves exponentially fast to a stable homogeneous dislocation-free stationary state BR0. As we select larger and larger positive stresses, the homogeneous stationary configuration is strained but continues

to be stable and dislocation-free until a critical stress F_c is reached. At F_c a subcritical pitchfork bifurcation occurs, as the global bifurcation diagram in Fig. 8 shows. The bifurcation diagram of the l^2 norm of the displacement vector versus F has been calculated using the AUTO program of numerical continuation of solutions [1]. We do not show here the complete bifurcation diagram, which is rather complex with many bifurcation points issuing from different stationary solution branches, most of which are unstable. Note in Fig. 8 that only two primary branches bifurcate from BR0 at $F = F_c = 0.219317$. As we will explain later, these branches are the main equilibrium solutions found in dynamical simulations in which stress values $F = 0.22$ are reached. These branches start being unstable for F close to F_c but become stable after limit points (BR1 exactly after the limit point, BR2 becomes stable after a secondary bifurcation point with $F > F_{l2}$), giving rise to intervals were several stationary solutions are simultaneously stable and, as we will see later, can be reached according to the stress history.

Consider the stable parts of BR1 and BR2:

- BR1 has two stable parts: one with larger norm than that of BR0, the other with smaller norm. The configuration of the solutions in the stable part of BR1 with norm larger than that of BR0 contains two edge dislocations of opposite Burgers vectors that originate from the splitting of *one dipole at* $y = 0$; see Fig. 9 (a). The configurations corresponding to the lower part of BR1 ($||u||_{BR1} < ||u||_{BR0}$, larger values of F in the diagram) contains four additional edge dislocations originating in the splitting of two additional dipoles appearing at $y = \pm 5$.
- Similar to BR1, BR2 has two stable parts with norms larger and smaller than that of BR0, respectively. The configurations corresponding to the upper part of BR2 have four edge dislocations with Burgers vectors $(\pm 1, 0, 0)$ originating from the splitting of *two dipoles at* $y = \pm 1$; Fig. 9(b). The configurations corresponding to the lower part of BR2 contain four additional edge dislocations originating from the splitting of two additional dipoles at $y = \pm 5$.

Not shown in Fig. 8, there is a third branch BR3 with stable configurations $||u||_{BR3} < ||u||_{BR0}$ for a certain interval of stresses close to F_c. We find it with the dynamical experiments that will be

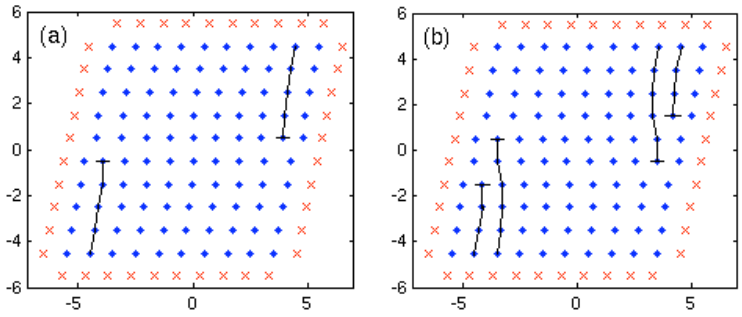

Figure 9. Configurations of the stationary solutions (a) BR1, (b) BR2, at $F_f = 0.22$. The crosses represent the positions of the boundary atoms which are fixed by the shear boundary condition. Panels (b) and (d) in Fig. 10 show the strain field associated to configurations (a) and (b), respectively.

described later, but it turned out to be quite elusive: we were not able to capture it using AUTO in all the simulations we did with different parameter values and lattice sizes. Fortunately, we found it with AUTO in the case presented in App. B and depicted in Fig. 30. This branch appears as a supercritical pitchfork bifurcation from the already unstable BR0 and its stable part contains four edge dislocations with opposite Burgers vectors originating from the splitting of *two dipoles at the boundaries*: $y = \pm 5$. Note that BR0, BR1 and BR2 have $0, 1$ and 2 dislocation dipoles, respectively. The third bifurcated branch that we find, BR3 has *two* dipoles, so our with our notation we count the branches that we find and not dislocation dipoles any more.

We have found ranges of F at which two or more stationary solutions are simultaneously stable. Let F_f be a stress slightly larger than the critical value F_c in Fig. 8. We would expect to evolve to a solution in BR1, BR2 or BR3 depending on the way we stress the sample. *Can we find a practical selection rule to attain these different stable solutions by reaching a final stress F_f in different way?*

One way to proceed is to start from the stable stationary configuration BR0 at $F = 0$. We then increase F to a small value ΔF, use the configuration BR0 for $F = 0$ as initial condition, solve

(3.3) and find the corresponding stable stationary configuration. Repeating this procedure, we follow BR0 until F_c and for $F > F_c$ we obtain the configuration BR2 at the corresponding value of F. Can we obtain other configurations doing things differently? The answer is yes. Suppose that we want to explore the stable stationary configurations at a stress $F_f = 0.22$ slightly larger than $F_c = 0.219317$. Starting with BR0 at $F = 0$, we turn in the stress according to a linear law: $F(t) = ct\,H(t_r - t) + F_f H(t - t_r)$, where $c = F_f/t_r$, t_r is the ramping time and $H(x)$ is the Heaviside unit step function. Same as in other multistable systems [66], the final configuration is either BR1, BR2 or BR3 depending on the final stress and the ramping time. See Table 1. At the time dislocations are nucleated, the displacement vector departs significantly from BR0.

Final stress, F_f	Ramping time, t_r	Nucleation height, y	Branch
0.2200	$t_r \geq 87$	± 1	BR2
0.2200	$82 \leq t_r \leq 86$	0	BR1
0.2200	$t_r \leq 81$	± 5	BR3
0.2247	$t_r \geq 325$	± 3	BR4
0.2247	$175 \leq t_r \leq 300$	0	BR1
0.2247	$120 \leq t_r \leq 150$	± 1	BR2
0.2247	$t_r \leq 115$	± 5	BR3

Table 1. Results obtained for a 10x10 lattice with $A = 0.3071$ and $\alpha = 0.2$. The final stress F_f, and the ramping time t_r, determine the height y at which the dislocation dipoles are nucleated. Only the branches BR1 and BR2 are depicted in the bifurcation diagram in Fig. 8.

Fig. 10 shows several snapshots of the strain component $2e_{12} = g_\alpha(u_{i,j+1} - u_{i,j})$ taken after the stress has reached its final value F_f and $u_{i,j}$ is evolving towards its final stationary configuration. A depression of the strain e_{12} at the sample center indicates nucleation of a dislocation dipole. At later times, this dipole is split in two edge dislocations of opposite Burgers vector that move towards the boundaries in opposite directions. The final configu-

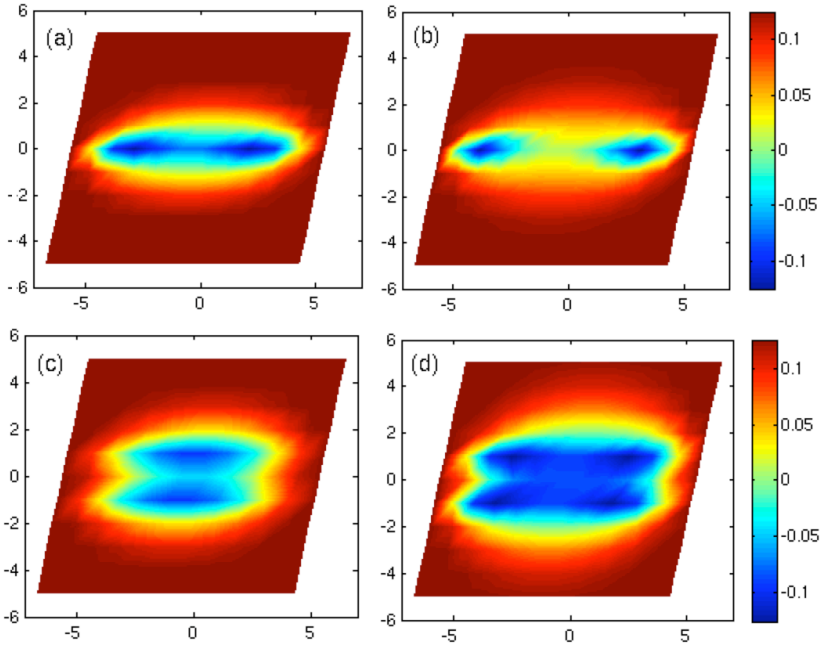

Figure 10. Four snapshots of the strain $2e_{12}$ at times (a) 1491.7 and (b) 1864.4 for the evolution towards BR1 at ramping time $t_r = 86$ ($c = 0.0026$), and at times (c) 2051.7 and (d) 2206.7 for the evolution towards BR2 at ramping time $t_r = 1000$ ($c = 2.2 \times 10^{-4}$). $F_f = 0.22$. Panels (a) and (b) in Fig 9 show the configurations corresponding to panels (b) and (d), resp., shown here.

ration is BR1. Similarly, for longer ramping times, two dislocation dipoles are nucleated, each splits into two edge dislocations with opposite Burgers vectors that then move towards the boundaries in opposite directions. The final result is BR2. It is interesting to observe that, at the time dipoles are nucleated, the strain components for the respective snapshots are very close to those of the unstable parts of the stationary solution branches BR1 and BR2. If we follow the unstable branch of BR1 backwards from the limit point for $F_{l1} \approx 0.11$ to the critical stress F_c, we observe that its strain e_{12} has a depression at the center of the sample corresponding to dipole nucleation for $F_{l1} < F < F_c$, but this depression becomes less and less observable as we approach F_c. Similarly, the unstable part of BR2 from its limit point $F_{l2} \approx 0.17$ to F_c first exhibits two symmetric depressions near the center of the sample corresponding to nucleation of two dipoles. Then these depressions diminish until the configuration of the unstable part of BR2 becomes very similar to that of BR1 as F approaches F_c. This is as it should be for BR1 and BR2 merge at F_c in a subcritical pitchfork bifurcation. Near F_c, BR1 and BR2 differ from BR0 by $\pm f\,\psi_{i,j}$. Here $f \propto \sqrt{F_c - F}$ and $\psi_{i,j}$ is the eigenvector corresponding to $\lambda_0(F_c) = 0$. It is interesting to observe how the components of this eigenvector present opposite sign for alternate rows of their corresponding lattice sites, $\psi_{i,j}\psi_{i,j+1} < 0$, maintaining the same sign along the same row, $\psi_{i,j}\psi_{i,k} > 0$. Regions in which dislocations may nucleate are then located in between rows j and $j+1$ for which $\psi_{i,j+1} - \psi_{i,j}$ is maximum ($y = 0, \pm 2$, for BR1) or minimum ($y = \pm 1, \pm 3$, for BR2). These differences are higher at the center of the sample: only one dipole is generated in BR1 (at $y = 0$) and, correspondingly, two in BR2 (at $y = \pm 1$).

The system in Eqs. 3.1 may be linearized about the homogeneous solution BR0 for any value of F. At $F = 0$, all the eigenvalues are negative, and the following sequence indicates at which values of F a new eigenvalue becomes positive:

$$\begin{aligned} 0.219317 &= F_c, \\ 0.220562, & \\ 0.222889, & \\ 0.226785, & \\ \cdots & \end{aligned}$$

The first value $F_f = 0.220000$ in Table 1 is right above the critical $F_c = 0.219317$, whereas for $F_f = 0.224700$ there are already three

positive eigenvalues of the Jacobian matrix. This seems to be the reason why a richer spectrum of attraction basins is observed: in this example, a new branch BR4 having dipoles at $y = \pm 3$ in found in the dynamical simulations (see Table 1).

We have presented numerical solutions corresponding to a 10x10 lattice. We have observed that the value of F_c and the type of the primary bifurcation do not change if we increase the computational domain. While for small samples we have $F_c > \alpha$, for increasing sizes of the domains we observe $F_c \to \alpha$. The branches acquire more limit points and similar slope to the one of BR0, many of them remaining really close to it. In some cases[2], the pitchfork bifurcation at F_c is supercritical, but both bifurcating branches have a limit point for a slightly higher stress and become unstable along decreasing values of F, repeating a similar pattern to the one described before. For $\alpha = 0.1$ and small samples[3], the pitchfork bifurcation remained supercritical, giving rise to stable branches spanned along increasing values of F. However, for larger samples and the same value of α, the pitchfork bifurcation at F_c was again subcritical[4]. For $\alpha = 0.4$ and a 10x10 lattice, the branches BR1 and BR2 contain a number of additional limit points and secondary bifurcations, but still have stable parts. Varying A in our simulations did not change much the resulting values of F_c.

The reflection symmetry with respect to the horizontal axis in the middle of the crystal is typical for lattices with an odd number N_y of atom rows. Therefore each branch in the bifurcation diagram using the l^2 norm of the displacement vector corresponds to two different solution branches with the same norm and symmetric configurations. For example, if we find in one branch a dislocation at height $+y$ with Burgers vector $b = +1$, the other branch will have at $-y$ a dislocation with $b = -1$.

In Appendix B, we show bifurcation diagrams corresponding to different parameters. While BR1 and BR2 persist in samples of different size, the location of secondary bifurcation and limit points and the configurations for secondary solution branches depend on the size and shape of the crystal.

Now what are the effects of inertia? The bifurcation diagram corresponding to stationary solutions is still the same as pre-

2 $\alpha = 0.2$, in a 10x40 lattice.

3 $\alpha = 0.1$, in 6x6 and 8x8 lattices.

4 $\alpha = 0.1$, in 10x10 and 14x14 lattice.

sented here. However, the stability character of the solutions changes. In the conservative case $m = 1$, $\alpha = 0$, stable solutions are no longer asymptotically stable. Linearizing (3.3) about a stable solution, we find a problem with purely imaginary eigenvalues. Therefore these solutions are centers: small disturbances about them give rise to small permanent oscillations about them. The linearized problem about unstable solutions has pairs of positive and negative eigenvalues and therefore these solutions are saddle-centers in general.

What have we learned about an instability and dislocation nucleation criterion from our bifurcation study? Clearly F_c marks the instability of the homogeneous solution branch BR0 and dislocations are nucleated at stress values more or less close to F_c, although the fact that the bifurcation is subcritical makes it important to determine the stresses at which the solution branches BR1 and BR2 become stable. This cannot be done by simple linear stability calculations: instead numerical continuation algorithms such as AUTO have to be employed. F_c is characterized as the stress value at which the largest eigenvalue of the linear eigenvalue problem about BR0 becomes zero. As it is well-known, we can determine the largest eigenvalue by solving the minimization problem of a quadratic functional $\sum_{ijkl} \varphi_{i,j} \mathcal{L}_{i,j,k,l} \varphi_{k,l}$ over the class of square summable vectors $\varphi_{i,j}$. The relation of this problem to the Λ criterion remains unclear. In the present case of a perfect lattice under shear, the CRSS criterion does not seem relevant.

3.3 CRITICAL STRESS FOR SPLITTING DISLOCATION DIPOLES

3.3.1 *Introduction*

In this section, we insert a dislocation dipole as initial condition in our problem, and then impose increasing shear strain F in the boundary. At a certain critical value, $F_{c,dip}$, the dislocation dipole starts to split. We find this critical value to be an order of magnitude lower than the previous one calculated for dislocation nucleation (Sec. 3.2), which explains why in that case the dislocation dipoles were always observed to split once they were nucleated.

3.3.2 *The Model*

As in the previous section, we use the following equations:

$$m\frac{\partial^2 u_{i,j}}{\partial t^2} + \beta\frac{\partial u_{i,j}}{\partial t} = u_{i+1,j} - 2u_{i,j} + u_{i-1,j} + A\left[g_\alpha(u_{i,j+1} - u_{i,j}) + g_\alpha(u_{i,j-1} - u_{i,j})\right], \tag{3.3}$$

where $m = 0$, $\alpha = 0.25$, $\beta = 1$, $A = 1$. The study of $F_{c,nuc}$ presented in the previous Sec. 3.2 uses $A = 0.3071$, which corresponds to tungsten. A similar nucleation study is reproduced for $A = 1$ in Sec. B.2 of App. B. Dislocation cores when $A = 1$ are narrower. This allows to perform numerical simulations in small lattices reducing the interaction with the boundaries. When $A = 0.3071$, cores are wider and the lattices have to be enlarged, increasing the computational cost. For comparing the order of magnitude between $F_{c,dip}$ and $F_{c,nuc}$ we choose $A = 1$.

3.3.3 *Initial and boundary conditions*

In this section we explain how we use as initial and boundary conditions the static field of two opposite edge dislocations that form the dipole. We add an extra shear strain field F at the boundary and look for the critical value $F_{c,dip}$ at which the dipole starts to split. We maintain the static elastic field of the dislocations centered at their original positions (to which the external shear F is added) as boundary condition, in spite the fact that they have started to move. This does not alter noticeably the value we obtain for $F_{c,dip}$, and results in the dislocations moving step by step for increasing F towards the boundaries. To have dislocations moving all at once to the boundaries, the elastic field used in the boundary conditions would need to be updated, so as to be centered in the actual location of the dislocations. Since we are interested in comparing $F_{c,dip}$ and $F_{c,nuc}$ and the former is not really affected by the boundary conditions that we choose, we just keep the original elastic far field of the dislocations centered in the original position at the beginning.

Given a perfect $N_x \times N_y$ grid of atoms with lattice spacing normalized to unity, it is possible to rigidly displace all of them

to positions (x, y) such that any of the atoms are located at the origin. It is possible then to insert an edge dislocation centered at the origin of coordinates having Burgers vector b, by using the following well known displacement fields [12]:

$$U_{[(0,0);b]}(x,y) = \frac{b}{2\pi}\left[tan^{-1}\left(\frac{y}{x}\right) + \frac{xy}{2(1-\nu)(x^2+y^2)}\right], \quad (3.4)$$

$$V_{[(0,0);b]}(x,y) = \frac{b}{2\pi}\left[-\frac{1-2\nu}{4(1-\nu)}\ln\left(\frac{x^2+y^2}{b^2}\right) + \right.$$
$$\left. + \frac{y^2}{2(1-\nu)(x^2+y^2)}\right], \quad (3.5)$$

along the x and y directions, respectively. Here ν is the Poisson ratio (for tungsten, $\nu = 0.278$). The subscript $[(0,0);b]$ indicates that a dislocation of Burgers vector b has been located at $(x_d, y_d) = (0,0)$. The displacement fields $U_{[(x_d,y_d);b]}(x,y)$, $V_{[(x_d,y_d);b]}(x,y)$ resulting from placing an edge dislocation at any coordinates (x_d, y_d) are computed substituting $x \to x - x_d$ and $y \to y - y_d$ in the right-hand side of Eqs. 3.4 and 3.5. In the example presented here we set initial conditions as follows:

$$\mathbf{u}(t_0) = \mathbf{U}_{[(1,+1);1]} + \mathbf{U}_{[(1,-1);-1]}, \quad (3.6)$$

$$\mathbf{v}(t_0) = \mathbf{V}_{[(1,+1);1]} + \mathbf{V}_{[(1,-1);-1]}, \quad (3.7)$$

so we have two opposite-sign ($b = +1, -1$) edge dislocations located at $(1,+1)$, $(1,-1)$ which constitute a dislocation dipole that is centered at $(1,0)$ (See Fig. 11 (a)). Here we used vector notation for $\mathbf{u} = u_{i,j}$ (resp., $\mathbf{v} = v_{i,j}$), and correspondingly for $\mathbf{U}$ (resp., $\mathbf{V}$).

The reduced scalar model Eq. 3.3 neglects vertical displacements. Thus, the vector field 3.4-3.5 simplifies and must be replaced by

$$U_{[(0,0);b]}(x,y) = \frac{b}{2\pi}\tan^{-1}\left(\frac{y}{x\sqrt{A}}\right), \quad (3.8)$$

which solves the scalar elasticity equations for the displacements with the singularity corresponding to an edge dislocation located

at $(0,0)$. The initial condition is then

$$\mathbf{u}(t_0) \quad = \quad \mathbf{U}_{[(1,+1);1]} + \mathbf{U}_{[(1,-1);-1]}. \tag{3.9}$$

Concerning the boundary conditions, we proceed similarly as in Sec. 3.2: An external shear strain F is applied, so the additional term $F\,[j-(N_y+1)/2]$ is added to the displacement 3.9 of atoms (i,j) with $j=1,N_y$ or $i=1,N_x$. Atoms in the boundary remain fixed, having the corresponding displacement associated to the shear strain F in addition to the far field of both dislocations, as indicated.

3.3.4 *Methodology and Results*

We implement a numerical continuation algorithm (see Appendix C) for a sequence of values of F (See Fig. 11). In Fig. 12, we plot the distance ΔX between the dislocations in the x direction for increasing F. To compute it, we count the integer number of lattice spacings that exist in between the dislocations forming the dipole. We linearize system 3.3 about the corresponding stationary solution $\mathbf{u}^*(F)$ and find the eigenvalues $\lambda(F)$ of the corresponding Jacobian matrix, $\mathbf{J}(\mathbf{u}^*(F))$. We plot $\lambda_{max}(F)$ in Fig. 13. When performing numerical relaxation, the right hand side terms of Eqs. 3.3 where never greater than 10^{-13} in absolute value for the equilibrium configurations that we found.

We observe:

- For $F \leq 0.025$, the distance (in the x direction) between the dislocations is zero: they are vertically aligned.
- $F = 0.025$ (label (a) in Figs. 11, 12, 13) is the last value of F recorded before λ_{max} becomes positive. We may approximate $F_{c,dip}$ by 0.025. For $F < F_{c,dip}$, $\lambda_{max} < 0$ is found for a sequence of configurations in which the dipole remains stable at its initial position.
- For slighly larger values of F, we observe the dislocations finding equilibrium separation distances of $\Delta X = 2, 4$. As an example, observe label (b) in Figs. 11, 12.

- The dislocations glide and are trapped at the boundaries of the domain (maximum separation between them, $\Delta X = 16$) for $F \geq 0.045$. The first of this configurations is marked with label (c) in Figs. 11, 12.

In nucleation simulations with $A = 1$ and $\alpha = 0.25$, we obtain $F_{c,nuc} = 0.258$ (see Sec. B.2). We actually find $F_{c,nuc} > \alpha$, regardless of the value of A. For large lattices, we observe $F_{c,nuc} \to \alpha$.

In our dipole experiment, we have $F_{c,dip} = 0.025 = \alpha/10$. So we observe that the threshold for depinning the dislocations comprised by a dipole is an order of magnitude lower than the critical value for nucleation. This explains why in nucleation experiments the nucleated dipoles are immediately split and migrate to the boundaries once they are nucleated.

3.4 CONCLUSIONS

We have analyzed homogeneous nucleation of dislocation dipoles and dipole splitting when a 2D sample is acted upon by an external shear field F. We used a simple discrete elasticity model.

In the first section (3.2), we find that under shear stress, the homogeneous dislocation-free stationary solution becomes lineally unstable at a critical stress $F_{c,nuc}$. At this stress two stationary branches bifurcate subcritically from it forming a pitchfork bifurcation. Consider overdamped dynamics first. One of these branches (far from the bifurcation point) becomes stable and its configuration corresponds to nucleation of a dislocation dipole, splitting thereof and motion of the resulting edge dislocations with opposite Burgers vectors to opposite sites in the sample boundary. The other branch eventually becomes stable too and its configuration corresponds to nucleation and splitting of two dislocation dipoles, that give rise to four edge dislocations. To obtain different stable branches that coexist at the same value of a supercritical stress, ramping the stress over a time period of variable duration is used. Slow ramping leads to the final configuration with four dislocations, whereas appropriately fast ramping leads to the stationary configuration with only two edge dislocations. This bifurcation picture seems to describe larger lattices and it describes the stationary solutions even if inertia is added.

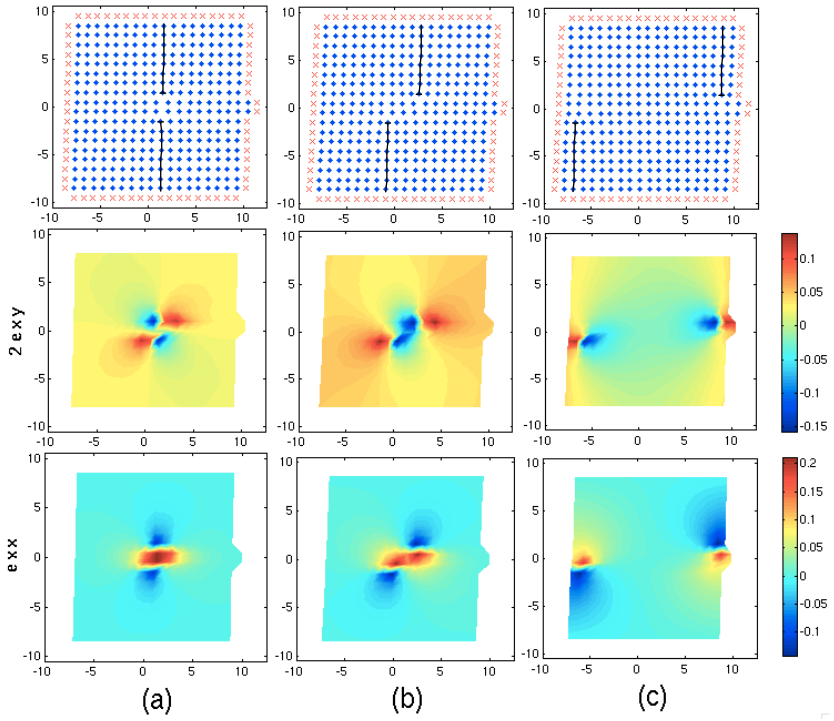

Figure 11. Positions and strain components $2e_{12}$ and e_{11} of relaxed equilibrium configurations found by numerical continuation for (a) $F_{c,dip} = 0.025$, (b) $F = 0.044$, (c) $F = 0.045$. The distance ΔX that separates the dislocations is depicted in Fig. 12, the labels of which correspond to the snapshots shown in this plot.

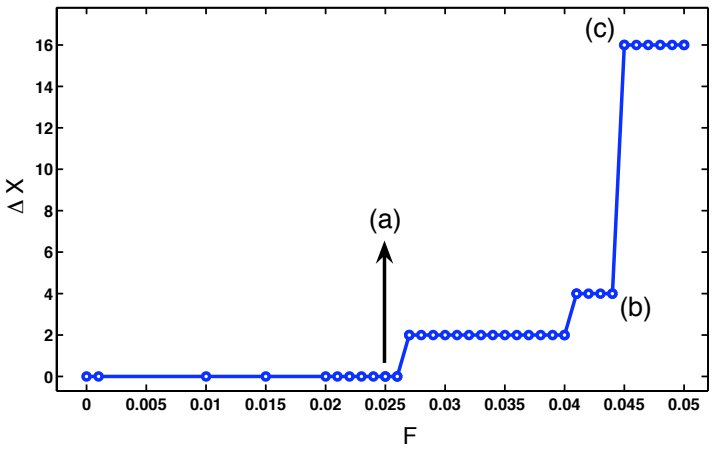

Figure 12. Separation ΔX of the dislocations in the x direction as a function of the external parameter F. Each dot represents an equilibrium configuration. Labels (a), (b), (c) mark data points corresponding to the configurations depicted in Fig. 11.

In the second section (3.3), we calculate a critical value $F_{c,dip}$ that gives rise to an instability after which the dipole starts to split. For large enough F, dislocations migrate to the sides of the domain. We compare the critical value for dipole splitting $F_{c,dip}$ to the one obtained for nucleation, $F_{c,nuc}$. We find these values to be of different order of magnitude: $F_{c,dip} \sim 0.1\alpha < F_{c,nuc} \sim \alpha$. This explains why in nucleation experiments the nucleated dipoles are immediately split and migrate to the boundaries once they are nucleated. Both threshold values are parametrized by α, the parameter in the periodic $g_\alpha(x)$ functions (see Appendix A).

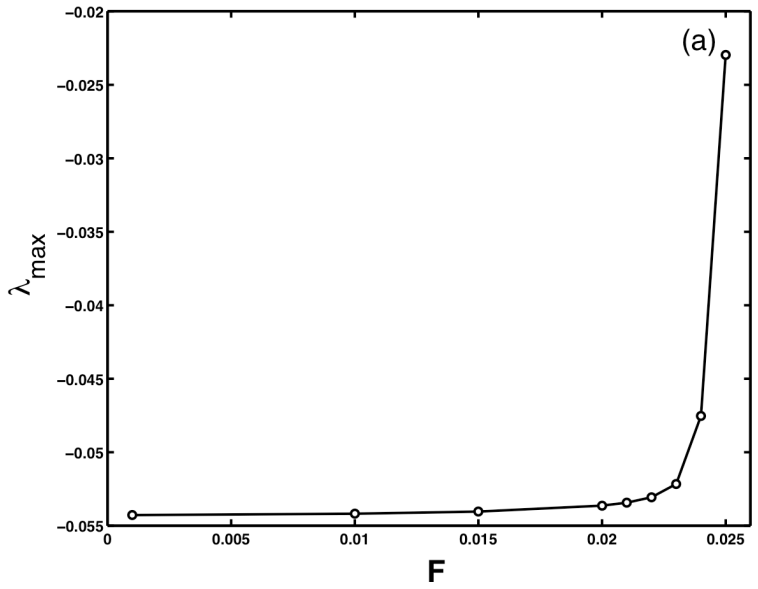

Figure 13. Maximum eigenvalue λ_{max} of the Jacobian matrix corresponding to the linearized system in Ecs. 3.3 as a function of the external strain field F. Label (a) marks the last value $F = 0.025$ found with $\lambda_{max} < 0$.

4

APPLICATION TO MISFIT DISLOCATIONS IN HETEROEPITAXIAL SYSTEMS

4.1 OUTLINE

This chapter is concerned with the concepts of critical thickness and critical misfit in heteroepitaxial systems. In the first section, a two-dimensional discrete elasticity model is used to compute the critical thickness at which interfacial pure edge dislocations are energetically preferred to form in the InAs/GaAs(110) heteroepitaxial system. The calculated critical thickness of six monolayers, is fairly close to the measured value in experiments, five. In the second section, we use a simple scalar discrete elasticity model to illustrate the concept of critical misfit in a substrate-film interface.

4.2 CRITICAL THICKNESS FOR MISFIT DISLOCATION FORMATION IN INAS/GAAS(110) HETEROEPITAXY

4.2.1 *Introduction*

Heteroepitaxial growth of InAs on GaAs(110) [67] has been examined in detail using different techniques, including scanning tunneling microscopy (STM) and transmission electron microscopy (TEM). The strain relief mechanisms depend strongly on the orientation of the substrate over which layers are being grown. In the case of a (110) substrate, growth of the InAs film occurs in three different stages, depending on the film thickness, h_f:

- $1 \leq h_f \leq 3$ monolayers (ML). A uniform network of very small 1 ML high InAs islands is formed.
- $3 \leq h_f \leq 200$ ML. The islands formed during the first stage coalesce and the film grows layer by layer so that no three-

dimensional (3D) structures on top of the last layer are created. Early on, for $3 \leq h_f \leq 5$ ML, an array of pure edge misfit dislocations (90° MDs) is formed at the interface, and it induces a lattice distortion that is visible at the surface. The dislocation lines have the [100] direction, whereas their Burgers vectors lay along the $[1\bar{1}0]$ direction. This stage is called the $[1\bar{1}0]$-relaxed stage.

- $h_f \geq 200$ ML. The [001] direction is also relaxed by an array of 60° MDs directed along $[1\bar{1}0]$. This array is perpendicular to the previous one, and thus a complete dislocation network has been formed at the interface [68].

In this section, we consider the second stage of film growth. According to experiments [69, 70], the first interfacial dislocations are found for $h_f = 3$ ML, and a complete array of 90° MD has been formed when $h^*_{f,exp} \sim 5$ ML. By using energy arguments and a discrete elasticity model of heteroepitaxial growth in InAs/GaAs(110), we compute the critical film thickness h^*_f necessary to create the MD array. We find $h^*_f = 6$ ML.

4.2.2 *The model*

We model atoms on a plane perpendicular to the dislocation lines (parallel along [001]) that contains the Burgers vector of MDs (along $[1\bar{1}0]$). Each layer of the resulting 2D square lattice comprises two layers of the 3D zincblende structure of the material. We choose the slice of InAs/GaAs (110) so that indium atoms are grown on a Ga substrate, both on square lattices that have different lattice constants. Cartesian axes on our 2D lattice will be chosen along $[1\bar{1}0]$ and [110], as indicated in Fig. 14. The elastic constants and the lattice constant referred to these axes are related to those in the [100] direction according to the formulas (cf. Eq. 13-43 in [14], $H = 2C^{[100]}_{44} + C^{[100]}_{12} - C^{[100]}_{11}$ is the anisotropy factor):

$$C^{[1\bar{1}0]}_{11} = C^{[100]}_{11} + H/2, \tag{4.1}$$
$$C^{[1\bar{1}0]}_{12} = C^{[100]}_{12} - H/2, \tag{4.2}$$
$$C^{[1\bar{1}0]}_{44} = C^{[100]}_{44} - H/2, \tag{4.3}$$
$$a^{[1\bar{1}0]} = a^{[100]}/\sqrt{2}. \tag{4.4}$$

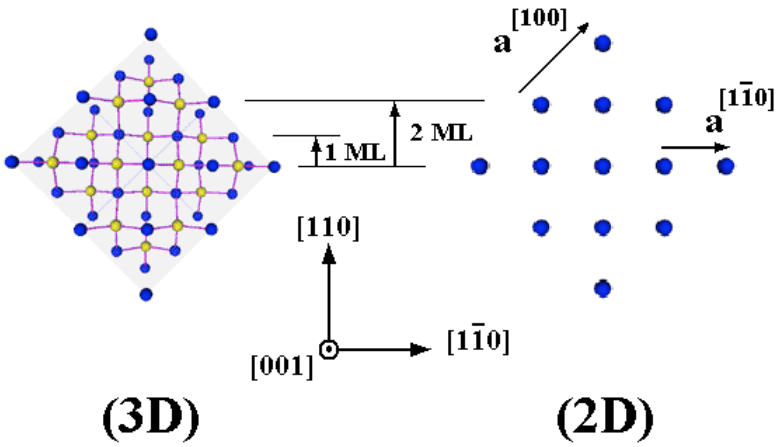

Figure 14. Extracting a plane of atoms from the three-dimensional (3D) zincblende lattice results in a two-dimensional (2D) square lattice. Each layer of the 2D lattice represents 2 ML of the real crystal.

Table 2. Elastic constants in 10^9 N/m^2 and lattice parameters in Å corresponding to the (100) direction.

	$C_{11}^{[100]}$	$C_{12}^{[100]}$	$C_{44}^{[100]}$	$a^{[100]}$
InAs	83	45.0	39.5	6.05
GaAs	118	53.5	59.0	5.65

Our computational domain comprises M layers: layers $1, ..., p$, correspond to the substrate, and layers $p+1, ..., M$, to the film. Each computational layer represents two physical monolayers, as shown in Fig. 14. A cell in the square lattice, labeled by indices (l, m), contains one atom located at coordinates $x_i(l, m; t)$, $i = 1, 2$ at time t. The side of a square cell containing a substrate atom is $a(l, m) = a^-$ $(m \leq p)$, and it is $a(l, m) = a^+$ for a cell containing a film atom $(m > p)$. The lattice misfit is $\epsilon = (a^+ - a^-)/a^+ = 7\%$.

In our model, we consider a discrete energy $V(\{x_i(l, m; t)\})$,

$$V = \sum_{l,m} a^3(l, m) W(l, m; t) = \frac{1}{2} \sum_{l,m,i,j,r,s} a^3(l, m)\, c_{ijrs} \nabla_{ij} \nabla_{rs}, \qquad (4.5)$$

Table 3. Elastic constants in 10^9 N/m^2 and lattice parameters in Å corresponding to the $[1\bar{1}0]$ direction.

	$C_{11}^{[1\bar{1}0]}$	$C_{12}^{[1\bar{1}0]}$	$C_{44}^{[1\bar{1}0]}$	$a^{[1\bar{1}0]}$
InAs	$C_{11}^{+} = 103.50$	$C_{12}^{+} = 24.50$	$C_{44}^{+} = 19.00$	$a^{+} = 4.28$
GaAs	$C_{11}^{-} = 144.75$	$C_{12}^{-} = 26.75$	$C_{44}^{-} = 32.25$	$a^{-} = 4.00$

in which the strain energy density W depends on the tensor of elastic constants c_{ijrs} and on displacement differences that become $\partial u_i/\partial x_j$ in the continuum limit (u_i is the displacement field):

$$\nabla_{ii} = g\left(\frac{D_i^+ x_i(l,m;t)}{a(l,m)} - 1\right) \sim \frac{\partial u_i}{\partial x_i}, \tag{4.6}$$

$$\nabla_{ij} = g\left(\frac{D_j^+ x_i(l,m;t)}{a(l,m)}\right) \sim \frac{\partial u_i}{\partial x_j}, \quad i \neq j, \tag{4.7}$$

$i,j = 1,2$. Here $D_1^+ x_i(l,m;t) = x_i(l+1,m;t) - x_i(l,m;t)$ and $D_2^+ x_i(l,m;t) = x_i(l,m+1;t) - x_i(l,m;t)$ and $g(x) \sim x$ for small x. Note that the x_i are absolute coordinates, not displacements from equilibrium positions. The atoms at the top layer do not have any other ones above them, so that $D_2^+ x_i(l,M;t) = 0$, which represents a free surface boundary condition. In the continuum limit, W agrees with anisotropic linear elasticity:

$$W(l,m;t) \rightarrow \frac{C_{11}^{\alpha}}{2}\left(\frac{\partial u_1}{\partial x_1}\right)^2 + \frac{C_{11}^{\alpha}}{2}\left(\frac{\partial u_2}{\partial x_2}\right)^2 + C_{12}^{\alpha}\frac{\partial u_1}{\partial x_1}\frac{\partial u_2}{\partial x_2} + \frac{C_{44}^{\alpha}}{2}\left(\frac{\partial u_2}{\partial x_1} + \frac{\partial u_1}{\partial x_2}\right)^2. \tag{4.8}$$

Here $\alpha = -,+$ depending on whether cell (l,m) belongs to the substrate $(m \leq p)$ or to the film $(m > p)$, respectively.

4.2.3 *Methodology*

The potential energy V yields a force $-\partial V/\partial x_i$ on the atom located at x_i and Newton's second law provides the equations of

motion for our model. Local equilibrium configurations can be found from stationary solutions or from energy minima. It is computationally more efficient to seek for stationary configurations of the equations of motion by solving the overdamped equations:

$$\beta \frac{dx_i(l,m;t)}{dt} = -\frac{\partial V}{\partial x_i(l,m;t)}, \quad i = 1,2, \tag{4.9}$$

where $\beta = 1$ is the damping coefficient. The relaxation method starts from an initial guess $\{x_i(l,m;t_0)\}$ and Eqs. 4.9 are solved until a stationary configuration $\{x_i(l,m;t_\infty)\}$ is reached. Then its *energy density* is the corresponding energy V in Eq. 4.5 divided by the sample volume. We will compare the energy densities of the coherent (i.e., without dislocations) and dislocated configurations.

Initial conditions are chosen as close as possible to a stationary solution to which the system is observed to relax. The substrate is set so as to have its equilibrium lattice constant a^- as bond length. In the coherent configuration, epilayer atoms are set to be vertically aligned to those in the substrate, and they have their own lattice spacing a^+ in the dislocated configuration. The difference between the substrate and film lattice constants causes the formation of a MD array at the interface. At both sides of the domain boundary conditions are periodic, atoms in the substrate lower layer $(m = 1)$ do not move, and the top layer is a free surface; cf. section 4.2.2.

To ensure that the depressions at surfaces are found right above dislocation cores, we need to relabel atoms in dislocated configurations. The right hand side of Eqs. 4.9 includes the coordinates of first and second neighbors of the atom (l,m). These neighbors determine a stencil of dependence, which may be updated. When dislocations are present at the interface, we compute the lists of neighbors, *upper-neighbor*(l) and *lower-neighbor*(l), for atoms at layers p and $p+1$, respectively. The upper neighbor of a given atom (l,p) will be that minimizing

$$|x_1(\textit{upper-neighbor}(l), p+1; t) - x_1(l,p;t)|. \tag{4.10}$$

Similarly, an atom $(l, p+1)$ will find its first neighbor at the layer p by minimizing

$$|x_1(l, p+1; t) - x_1(\textit{lower-neighbor}(l), p; t)|. \tag{4.11}$$

This allows to update the stencil of dependence. The corresponding change in the energy V is introduced by redefining the gradients at layer p: $D_2^+ x_i(l,p;t) = x_i(\textit{upper-neighbor}(l), p+1;t) - x_i(l,p;t)$. The critical thickness h_f^* is the minimum number of film layers for which the dislocated configuration has lower stationary energy density than the coherent one. Recall that each computational layer in $h_{f,2D}$ represents 2ML of the 3D crystal (Figs. 14 and 15). In our simulations, we inserted 8 dislocations ($N_x = 121$

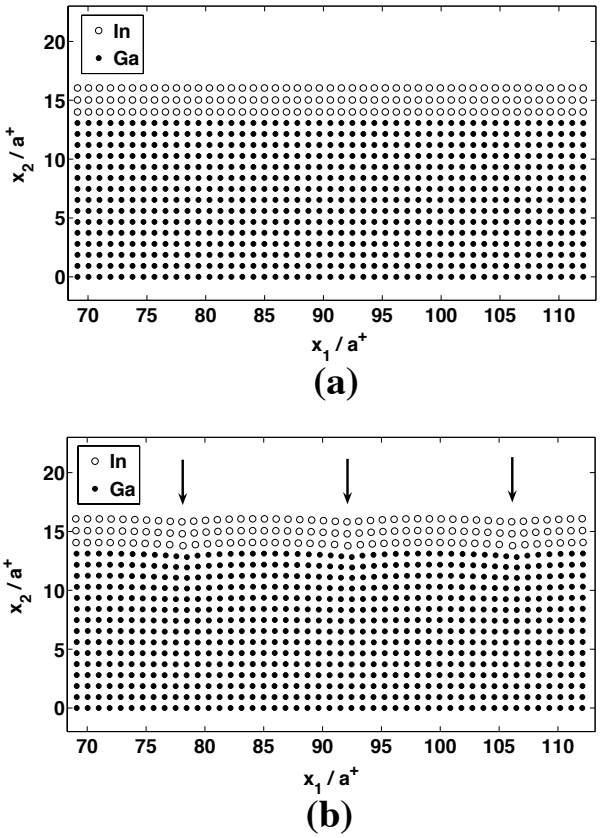

Figure 15. Partial view of (a) coherent and (b) dislocated relaxed configurations with $g_2(x) = \tan^{-1}(\pi x)/\pi$. The arrows point towards the valleys formed above dislocation core regions. Three computational layers $h_{f,2D} = 3$ represent six 3D MLs.

columns of atoms for the substrate, only 113 for the film) and 15 substrate layers. This value is similar to the inter-dislocation distance, hence the substrate may be considered infinitely extended. No dependence of h_f^* on the system size was observed.

4.2.4 *Results*

Fig. 16 shows our results. We inserted two different functions: the first one, $g_1(x) = x$, is purely linear, and $g_2(x) = \tan^{-1}(\pi x)/\pi$, is anharmonic. The simulations with both functions yield qualitatively similar results: the energy density of the dislocated configuration increases as the epilayer thickness increases, whereas the energy density of the coherent configuration decreases. Besides, in the relaxed dislocated configurations (see Fig. 15), valleys are formed above the dislocation lines, in agreement with the experimental observations.

In the linear case, the energy density of the dislocated configuration is lower than that of the coherent one starting from a critical thickness $h^*_{f,2D,1} = 5$, that corresponds to $h^*_{f,1} = 10$ ML. For the other function, we have $h^*_{f,2D,2} = 3$, $h^*_{f,2} = 6$ ML. The latter is closer to the experimental value, $h^*_{f,exp} \sim 5$, as shown in Fig. 15(b).

4.3 CRITICAL MISFIT FOR DISLOCATION FORMATION AT THE SUBSTRATE-FILM INTERFACE

4.3.1 *Introduction*

In this section, we present a very simple example that evidences the existence of a critical misfit ϵ_c, above which the defect-free configuration becomes unstable and interfacial misfit dislocations are formed.

4.3.2 *The model*

We will restrict the analysis to a 2D region that comprises a part of the substrate-film interface. Atoms (l, m) will be assumed to move only along the x direction and their displacements will be $x(l, m)$

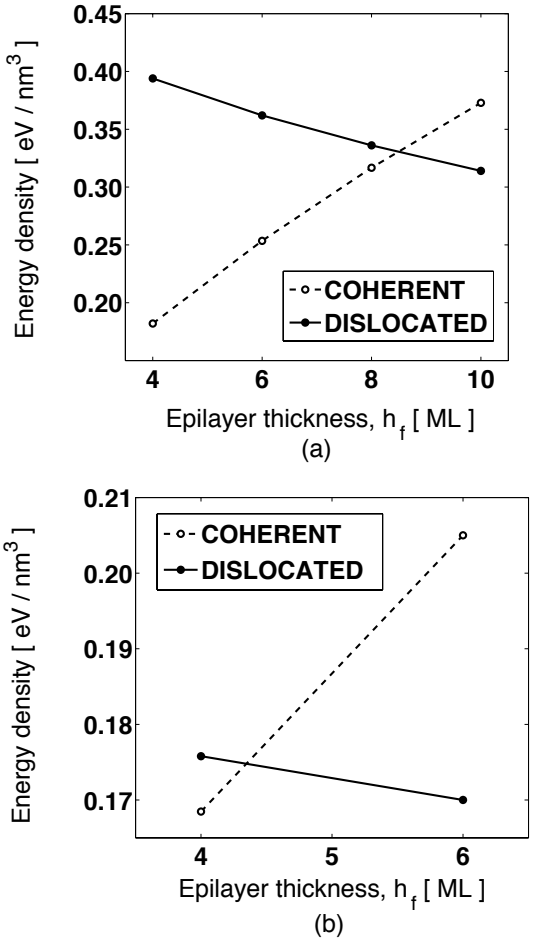

Figure 16. Energy density vs film thickness for (a) the linear case, $g_1(x) = x$, and (b) for $g_2(x) = \tan^{-1}(\pi x)/\pi$.

We have the following set of equations:

$$\begin{aligned}\beta\frac{\partial x(l,m;t)}{\partial t} &= x(l+1,m;t) - 2x(l,m;t) + x(l-1,m;t) \\ &\quad + A\Big\{ g_{\alpha,\epsilon}\big[x(l,m+1;t) - x(l,m)\big) \\ &\quad + g_{\alpha,\epsilon}(x(l,m-1) - x(l,m)\big]\Big\}. \quad (4.12)\end{aligned}$$

Here, $\epsilon = 0$ for atoms in the substrate ($m = 1, ..., p$) and $\epsilon \geq 0$ for those in the film ($m = p+1, ..., N_y$). In the interface, we will compute $g_{\alpha,0}\left[x(l,p+1) - x(l,p)\right]$. A particular material should

be modeled inserting $A = C_{44}/C_{11}$ but, for simplicity, we take $A = 1$ and choose $\alpha = 0.25$, $\beta = 1$. So we are presenting a very simple example in which all the discrepancy between substrate and film relies on the difference in their lattice parameters.

4.3.3 *Methodology and Results*

We will proceed to perform numerical continuation as explained in Appendix C, taking the misfit ϵ as the continuation parameter. The sequence will be $\epsilon_0 = 0 < \epsilon_1 < ... < \epsilon_c < \epsilon_n$, so $\mathbf{x}^*(\epsilon_i)$ will be the corresponding relaxed equilibrium configurations and $\mathbf{J}(\mathbf{x}^*(\epsilon_i))$ the Jacobian matrix of the system 4.12 linearized about $\mathbf{x}^*(\epsilon_i)$.

How do we set initial and boundary conditions? We set $\mathbf{x}^*(\epsilon_0 = 0)$ as a perfect lattice with period one. All atoms in the boundary have fixed positions, and are represented by crosses in Fig. 18. For any misfit, the lower row of substrate atoms has unity lattice spacing, whereas the upper row of film atoms has lattice spacing $1 + \epsilon$. Left and right sides of the domain are located in imaginary straight lines of slopes that scale as $-\epsilon^{-1}$ and ϵ^{-1}, respectively. These conditions do not capture any surface effect, they just describe the interface in the bulk of a hetereoepitaxial system.

We consider the critical ϵ_c to be the last negative $\lambda_{max}(\epsilon_c)$ that we find (ϵ_i is the maximum eigenvalue of $\mathbf{J}(\mathbf{x}^*(\epsilon_i))$; see Fig. 17). A further value $\epsilon_n > \epsilon_c$ is used to illustrate that dislocations form at the interface. In this case, there is no physical increase of ϵ and no intention to model dislocation nucleation, but just to demonstrate that the system becomes unstable at a critical misfit, ϵ_c. In this example, we find $\epsilon_c = 0.137865$ and illustrate the presence of dislocations for $\epsilon_n = 0.137866$.

Fig. 18 shows the presence of two edge dislocations at the center of the lattice, separated by 9 lattice spacings. Those dislocation nucleate near the boundary, at locations where the eigenvector associated to the zero eigenvalue attains its largest values. Then, they migrate to the interior of the crystal and stop when an equilibrium distance between them is reached. The final location of the dislocations is better appreciated in Figure 18 (b)-(c), where the discrete strains are visualized. The pattern does not change qualitatively by increasing the size of the lattice. The critical

misfits ϵ_c and ϵ_n increase with the size, in such a way that a barrier of equidistant dislocations is not formed with this procedure. Only two dislocations are generated as a result of a boundary instability at the edges of the lattice.

Nucleation of dislocations is strongly sensitive to the way loads are applied on lattices. Notice that in real heteroepitaxial growth, the misfit between the upper and the lower lattices is fixed. This fact forces the formation of a barrier of dislocations separated by an equilibrium distance determined directly by the misfit ($\sim 1/\varepsilon$). We conjecture that the critical height at which the barrier is formed might be found by a bifurcation analysis with respect to the height of the upper layer, similar to the one we have performed for the misfits with fixed height, but keeping the misfit fixed and varying the height instead. This would provide an analytical basis for the studies carried out in the previous section by energy methods.

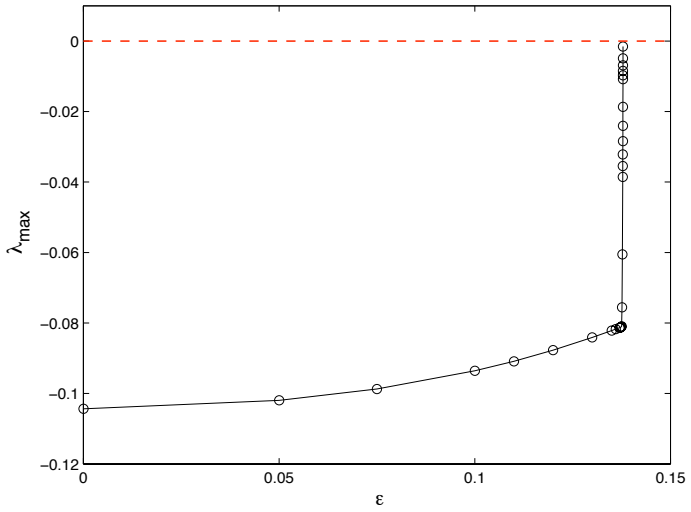

Figure 17. Maximum eigenvalue $\lambda_{max}(\epsilon)$ of the Jacobian matrix $\mathbf{J}(\mathbf{x}^*(\epsilon))$ associated to the linearized system about the corresponding stationary solution, $\mathbf{u}^*(\epsilon)$.

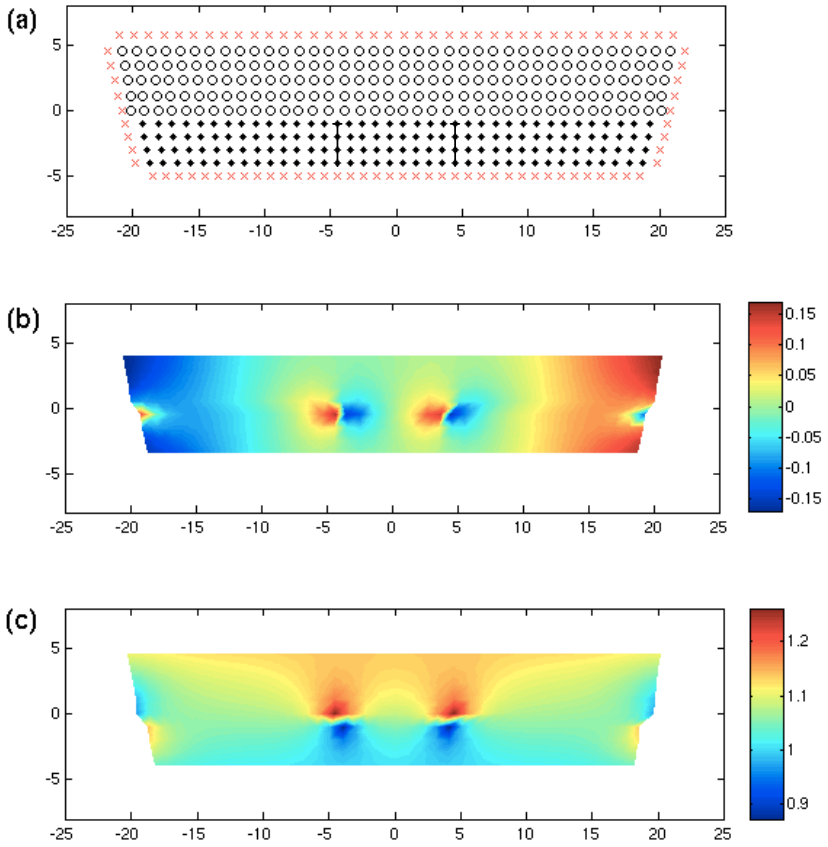

Figure 18. (a) Atomic positions and strain components (b) $2e_{12} = g\,[u(l,m+1) - u(l,m)]$, and (c) $e_{11} = u(l+1,m) - u(l,m)$, for the dislocated configuration found at $\epsilon = 0.137866 > \epsilon_c$.

4.4 CONCLUSIONS

We have presented results concerned with critical values for the film thickness and misfit in a heteroepitaxial system.

In the first part of this chapter, we used a simple 2D discrete elasticity model to compute the critical thickness at which it is energetically preferred for the InAs/GaAs(110) heteroepitaxial system to form interfacial pure edge dislocations. Despite its simplicity, the model provides qualitatively correct critical thickness (6 ML to experimentally observed 5ML), and coherent and dislocated energy densities as functions of film thickness.

In the second part, we show by linear stability analysis of a 2D scalar elasticity model, that the defect free-interface is no longer stable after a critical value of the misfit. We are currently devising a procedure to perform a similar stability analysis with respect to the height of the layers for a fixed misfit. This would provide an analytical basis for the energy studies carried out in the first part of this chapter.

5

APPLICATION TO CRACKS AND NANOINDENTATIONS

5.1 OUTLINE

In this chapter possible applications to model dislocation nucleation in crack formation and nanoindentation experiments are investigated. We show that simple scalar two dimensional models reproduce an elementary ductile behavior around the tip of cracks and basic nucleation mechanisms in simple indentation tests.

5.2 CRACK: TYPE I

5.2.1 *The model*

A really simple model for the openning of a crack is presented in this section. Let us consider a 2D rectangular computational grid of atoms labeled with $i = 1, ..., N_x$ and $j = 1, ..., Ny$ with a crack placed at the center of the upper half, as in Figure 19. We seek to gradually open the crack by numerical continuation (see App. C). The opening of the crack scales with F, since F^{-1} is the slope of the right-hand side of the crack. Due to the symmetry of the problem with respect to $i = p_x$, we mat restrict our computational model to the right half of the domain, by imposing adequate boundary conditions in the artificial boundary. Our computational grid is formed by atoms with indices $i = p_x, ..., N_x$ and $j = 1, ..., N_f(i)$ which is actually the right-hand half of the domain shown in Fig. 21 in next section (5.3), where we will model the whole domain, $i = 1, ..., N_x$. We have defined a list $N_f(i)$ indicating which is the highest atom for each column i meeting the crack. They define the crack wall. For example: $N_f(p_x) = p_y$ (crack tip), $N_f(p_2) = N_y$.

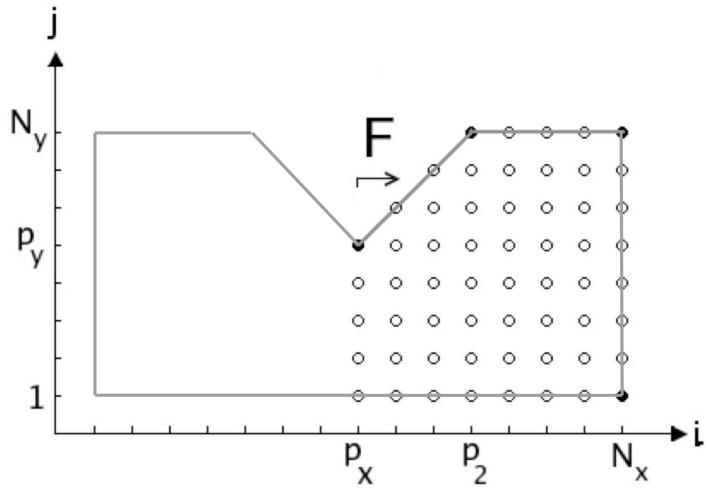

Figure 19. Simple model of a type I crack, in which only the right-hand half of it is modeled due to the symmetry of the problem. The atoms aligned below the crack tip are assumed to remain fixed, as well as those in the bottom layer. The opening of the crack is proportional to the parameter F, which fixes the positions of those atoms forming the upper boundary. The opening F of the crack is prescribed. A Neumann-type boundary condition is imposed at the right-hand side of the domain.

The atoms will be assumed to move only in the x direction, having displacements $u_{i,j}$ which are governed by the equations:

$$\begin{aligned} \beta \frac{\partial u_{i,j}}{\partial t} &= u_{i+1,j} - 2u_{i,j} + u_{i-1,j} + \\ &\quad + A\left[g_\alpha(u_{i,j+1} - u_{i,j}) + g_\alpha(u_{i,j-1} - u_{i,j})\right] \end{aligned} \tag{5.1}$$

where $\beta = 1$ is the damping coefficient, and we also have $\alpha = 0.25$ and $A = 1$. The use of overdamped dynamics is a numerical trick to reach the equilibrium configurations to which the system relaxes for long simulation times (the so-called 'relaxation' method). It is computationally simpler than solving a nonlinear stationary system and then checking the stability of the solutions.

5.2.2 *Boundary conditions*

See Figs. 19 and 20:

- We just model atoms $i = p_x, ..., N_x$.
- Atom (p_x, p_y) is at the crack tip; we locate it at the origin of coordinates in Fig. 20.
- We prescribe the opening of the crack in the x direction by the external parameter F, so that $u_{p_x,j} = (j - p_y) \cdot F$ when $j > p_y$ and $u_{i,1} = 0$ and $u_{i,N_y} = (N_y - p_y) \cdot F$ when $1 \leq i \leq N_x$. Bottom and top layers are fixed according to the crack opening.
- Finally, the column of atoms below the crack tip, $1 < j \leq p_y$ will have fixed $u_{p_x,j} = 0$. These atoms maintain the symmetry of the problem, remaining aligned at $x = 0$, and constitute the left hand side boundary of our problem (see Fig. 20).
- An extra column of virtual atoms are set to have $u_{N_x+1,j} = u_{N_x,j}$, so they act as a Neumann boundary condition.

Initial conditions for the numerical continuation algorithm are as follows: for $j \leq p_y$ atoms form a perfect undistorted lattice with $u_{i,j} = 0$; atoms above them with $j > p_y$ are displaced according to the homogenous deformation, $u_{i,j} = (j - p_y) \cdot F$. As the crack opening F is increased (i.e., the slope F^{-1} of the crack wall decreased), so is the tensional stress in the x direction.

In this very simple way, we prescribe the opening of a crack and observe how the inner atoms accommodate the induced stress and adjust in order to reach equilibrium configurations.

5.2.3 *Methodology and Results*

We use F as a numerical continuation parameter (see Appendix C), in order to compute subsequent equilibrium configurations for increasing crack widths that scale proportionally to F.

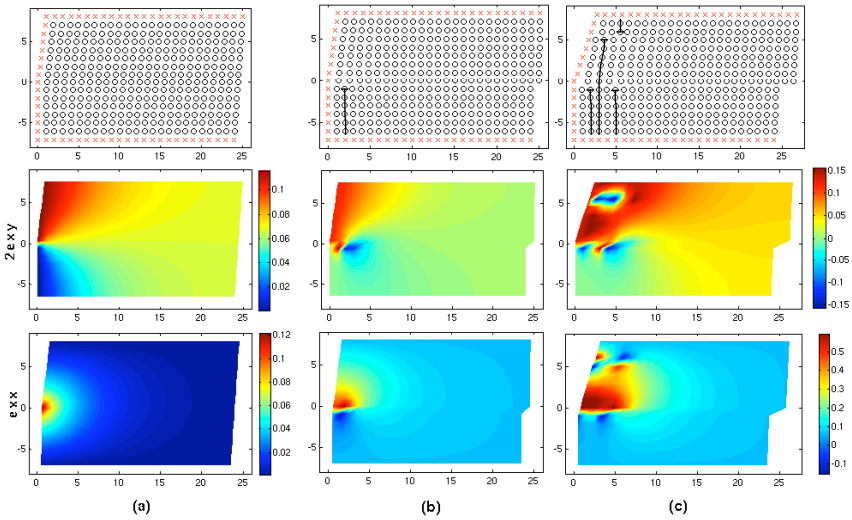

Figure 20. Atomic positions and strain field components $2e_{12}$ and e_{11} corresponding to equilibrium configurations found by numerical continuation for increasing openings of the crack: (a) $F_c = 0.13$, (b) $F = 0.14$ and (c) $F = 0.34$. While (a) is still defect-free, in (b) a dislocation already has nucleated, remaining close to the crack tip until a new dislocation is generated at $F = 0.27$. Then, it is slightly shifted in the along the $+x$ axis, due to the repulsion between equal-sign dislocations. The last configuration (c) shows a dislocation dipole at $y = 5.5$ that seems to have been homogeneously nucleated.

Fig. 20 shows the final configuration for $F = 0.34$. What do we observe when increasing F from zero?

- Firstly, a defect-free stage in which the strain field is concentrated at the crack tip.
- When a critical stress $F_c = 0.13$ is surpassed, the first dislocation is formed (for $F = 0.14$). This dislocation remains rather close to the crack tip, even though the crack width is further increased.
- At $F = 0.27$, a second dislocation is nucleated at the crack

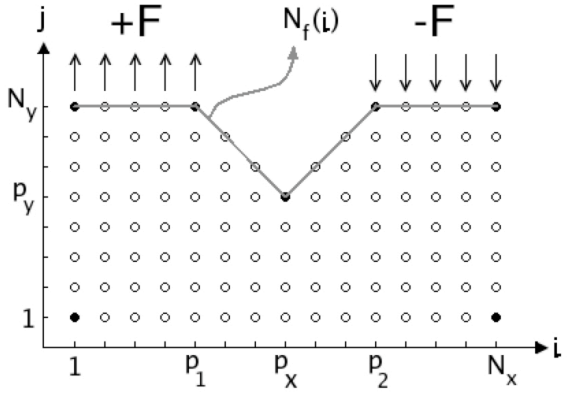

Figure 21. Simple model of a type II crack. The external parameter F controls the strength of the tension/compression stress field. $N_f(i)$ is an auxiliary list of atoms that belong to the faces of the crack.

tip and remains close to it, so the first one is slightly shifted in the $+x$ direction.

- At $F = 0.34$ a dislocation dipole is nucleated in the upper part of the domain. Its nucleation would be induced by the stress field due to the crack and the existing dislocations at its tip. It seems to be have been homogeneously nucleated when observed in the equilibrium configuration of Fig. ch5-crack-i, and its dislocations migrate gradually to the left and right-hand sides of the domain when F is further increased.

5.3 CRACK: TYPE II

5.3.1 *The model*

A type II crack may be modeled by the simplified picture shown in Fig. 21. We consider a system of dimensions $N_x \times N_y$. Atoms are labeled as (i, j). Some of them are missing between columns p_1 and p_2, due to the presence of a crack. The atom initially located at the crack tip is (p_x, p_y). The walls of the crack initially form 90°, and we have $p_x = (N_x - 1)/2$. We define a list $N_f(i)$ indicating which is the highest atom for each column i meeting

the crack. They define the crack wall. For example: $N_f(p_1) = N_y$, $N_f(p_x) = p_y$, $N_f(p_2) = N_y$.

The components of the displacement vector in the x and z directions are ignored. Only the vertical component of the displacement $v_{i,j}$ is considered, obeying the following overdamped equations:

$$\frac{dv_{i,j}}{dt} = v_{i,j+1} - 2v_{i,j} + v_{i,j-1} \quad + \quad A\big[g_\alpha(v_{i+1,j} - v_{i,j}) - g_\alpha(v_{i,j} - v_{i-1,j})\big]. \tag{5.2}$$

Recalling the discrete differences $D_1^{\pm} v_i^j = \pm[v_{i\pm1}^j - v_i^j]$ and $D_2^{\pm} v_i^j = \pm[v_i^{j\pm1} - v_i^j]$, the system 5.2 is rewritten as:

$$\frac{dv_{i,j}}{dt} = D_2^+ v_{i,j} - D_2^- v_{i,j} + A\big[g_\alpha(D_1^+ v_{i,j}) - g_\alpha(D_1^- v_{i,j})\big]. \tag{5.3}$$

5.3.2 *Boundary conditions*

Atoms in the boundary of the computational domain, will have the following prescribed values for the discrete differences, which will be substituted in their corresponding equations of motion 5.3:

- Left side: $D_1^- v_{1,j} = 0$.
- Right side: $D_1^+ v_{N_x,j} = 0$.
- Left-hand side of the top layer: $(1 \leq i \leq p_1)$: $D_2^+ v_{i,N_y} = F$. Here F is a non-dimensional force that pulls upwardly this side of the sample.
- Right hand-side of the top layer: $(p_2 \leq i \leq N_x)$: $D_2^+ v_{i,N_y} = -F$. Now F is the force pushing downwardly this side of the sample.
- Left-hand side face of the crack $(p_1 \leq i < p_x)$: $D_2^+ v_{i,N_f(i)} = 0$, $D_1^+ v_{i,N_f(i)} = 0$.
- Crack tip: $D_2^+ v_{p_x,p_y} = 0$.

- Right hand-side face of the crack ($p_x < i \leq p_2$): $D_2^+ v_{i,N_f(i)} = 0$, $D_1^- v_{i,N_f(i)} = 0$.
- Bottom layer of the domain: $D_2^- v_{i,1} = v_{i,1}$. This would be equivalent to have an extra row of fixed atoms below the sample (at $y = 0$).

5.3.3 *Methodology and Results*

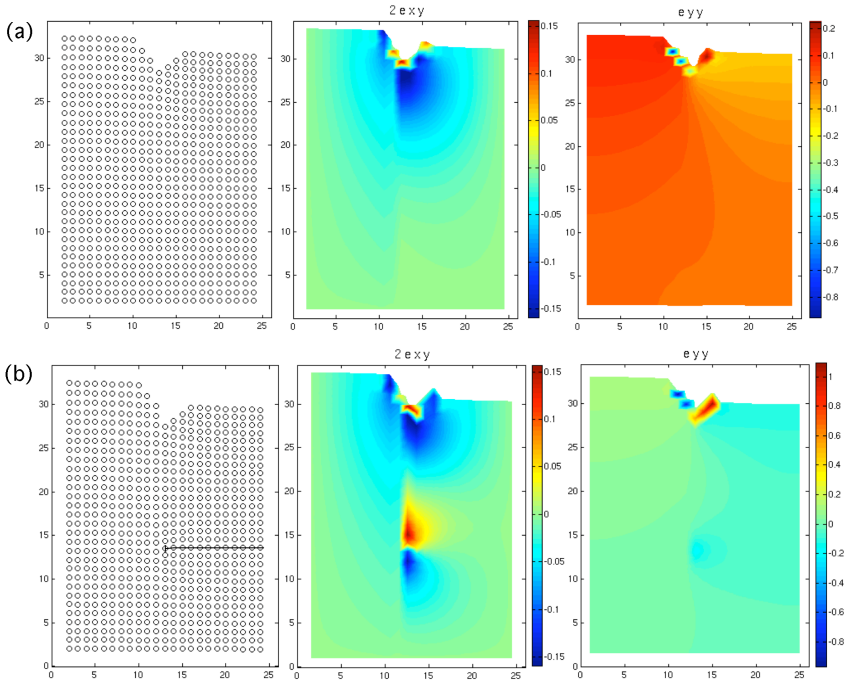

Figure 22. Equilibrium configurations of a type II crack obtained by numerical continuation for increasing values of the force field: (a) $F_c = 0.11$ is still defect-free, whereas for (b) $F = 0.12$ an edge dislocation has been nucleated. The final relaxed configuration shows that the dislocation finds its equilibrium position some distance apart from the crack tip.

We use a sequence $F_1 < F_2 < ... < F_n$ using F as numerical continuation (see Appendix C) parameter. We monitor the following components of the distortion tensor:

- $e_{22} = v_{i,j+1} - v_{i,j}$,

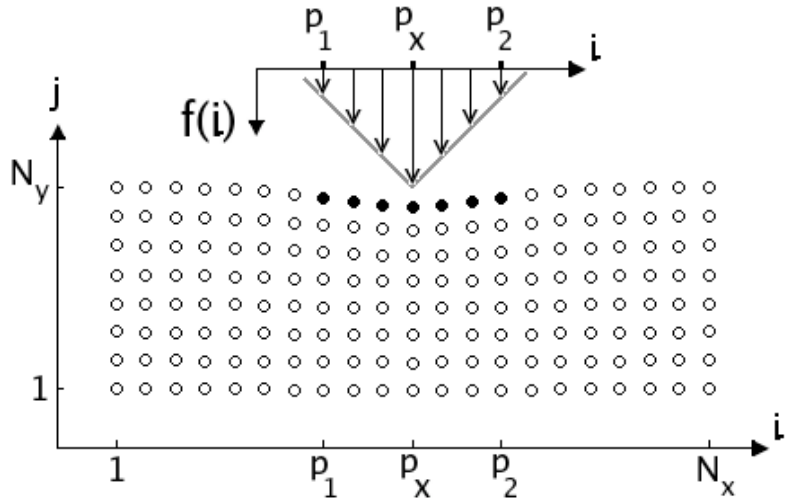

Figure 23. Modeling of a nanoindentation experiment. The force field $f(i)$ scales with the numerical continuation parameter F, reaching its maximum $f(p_x) = F$ right above the atom (p_x, N_y).

- $2e_{12} = g_\alpha(v_{i+1,j} - v_{i,j})$

Here $\alpha = 0.25$, $g_{0.25}(x) = \sin(2\pi x)/(2\pi)$ and $A = 1$.

We find a single dislocation being nucleated at the crack tip for $F = 0.12 > F_c = 0.11$. Configurations of the system are shown for both equilibrium configurations. Therefore, we found a critical value F_c. Incresing the deformation stress above this value, results in dislocation generation. We actually continued the experiment and found a sequence of dislocations following the first one. They do not remain close to the crack tip but travel to the bulk of the material, where they are finally found to be in equilibrium.

5.4.1 *The model*

Let us consider a $N_x \times N_y$ domain of atoms with vertical displacements $v_{i,j}$ obeying the following equations:

$$\frac{dv_{i,j}}{dt} = D_2^+ v_{i,j} - D_2^- v_{i,j} + A\left[g_\alpha(D_1^+ v_{i,j}) - g_\alpha(D_1^- v_{i,j})\right]. \quad (5.4)$$

5.4.2 *Boundary conditions*

We set the boundary conditions of this problem as follows (see Fig. 23):

- Left-hand side: $D_1^- v_{1,j} = 0$.
- Right-hand side: $D_1^+ v_{N_x,j} = 0$.
- Left-hand-side of the top layer: $(1 \leq i < p_1)$: $D_2^+ v_{i,N_y} = 0$.
- Right-hand-side of the top layer: $(p_2 < i \leq N_x)$: $D_2^+ v_{i,N_y} = 0$.
- Bottom layer of the domain: $D_2^- v_{i,1} = v_{i,1}$. This would be equivalent to have an extra row of fixed atoms below the sample (at $y = 0$).
- Central atoms ($p_1 \leq i \leq p_2$) are pushed downwards according to: $D_2^+ v_{i,N_y} = -f(i)$, where $f(i)$ is a dimensionless piece-wise linear force field that simulates the effect of a nanoindentation tip in that region.

The force field $f(i)$ is defined as (see Fig. 23):

- $f(p_1) = 0.25 \cdot F$,
- $f(p_1 + 1) = 0.50 \cdot F$,

- $f(p_1 + 2) = 0.75 \cdot F$,
- $f(p_x) = F$,
- $f(p_2 - 2) = 0.75 \cdot F$,
- $f(p_2 - 1) = 0.50 \cdot F$,
- $f(p_2) = 0.25 \cdot F$,

where $p_1 + 3 = p_x = p_2 - 3$, and F is an external parameter that controls the intensity of the applied force.

5.4.3 *Methodology and Results*

We use F as a numerical continuation parameter (see. Appendix C) following a sequence $F_0 < ... < F_t < ... < F_c < ...$ and monitor

- $e_{22} = v_{i,j+1} - vi, j$,
- $2e_{12} = g_\alpha(v_{i+1,j} - vi, j)$,
- $\delta = \frac{-1}{7} \sum_{i=p_1}^{p_2} v_{i,N_y}$,

for each equilibrium configuration. Here δ is the nanoindentation penetration depth into the sample. δ is computed averaging the height of those atoms (seven, in this case) on which the force field is acting. We use $A = 1$, $\alpha = 0.25$.

Fig. 24 shows F versus δ in our simulations. Even though our model assumes the crystal lattice to be square and $A = 1$, we find a behavior already observed in nanoindentation experiments [57, 71]. The curve F versus δ presents a sequence of jumps corresponding to nucleation of dislocations.

We find first a fairly linear deformation. At $F_t = 0.4$ ($\delta_t = 3.771$), we observe a transition to other regime which could be fit to a $\delta^{3/2}$ rule (dashed red line in Fig. 24):

$$F - F_t = 0.04 \cdot (\delta - \delta_t)^{3/2}, \tag{5.5}$$

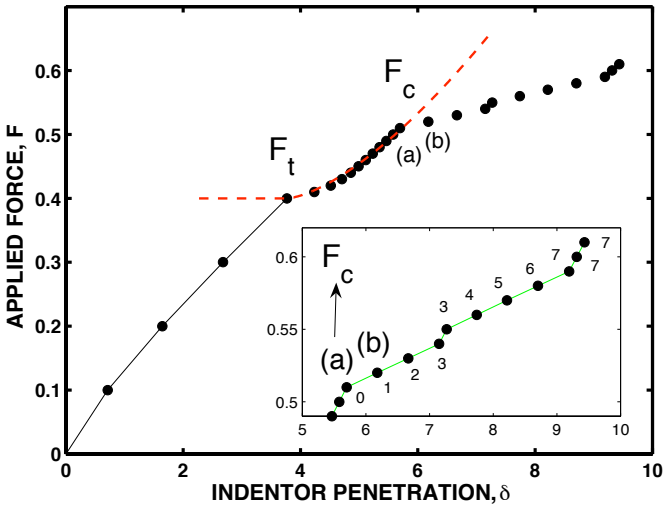

Figure 24. Applied force versus penetration depth: general view and zoom in the first critical region. We find a fairly linear initial stage for $F < F_t$, followed by a second stage $F_t < F < F_c$ that can be fit to a $\delta^{3/2}$ rule (red dashed line, see Eq. 5.5) and does not present any qualitative change in the system configurations with respect to the first stage, since both are defect-free. In a third stage $F > F_c$, we observe dislocation loops nucleation. The increasing number of dislocation loops that are found at $F > F_c$ are shown for each equilibrium configuration in the inset, beginning with (a) 0 at $F_c = 0.51$ and continuing with (b) 1 dipole at $F = 0.52$. These configurations are depicted in panels (a) and (b) of Fig. 25. Here we measure the penetration depth in units of the lattice parameter. In spite of the different scales, this plot is similar to the experimental one found in Fig. 1 of Ref. [57].

similar (but not necessarily related) to the one found in Fig. 1 of Ref. [57]. In this experiment, two different regimes are found: firstly, a $\delta^{3/2}$ rule fits a defect-free stage; secondly, dislocations are formed at discontinuities (horizontals jumps). Due to the different scales, one single experimental discontinuity would correspond to the whole region that we show in the inset of Fig. 24.

Increasing the force to $F = 0.52 > F_c = 0.51$ results in the creation of a dislocation loop that comprises two dislocations that are nucleated at both sides of the nanoindentation tip and then travel reaching an equilibrium location some distance apart from the stress field created by the tip. The creation of this loop results in a discontinuity the $F(\delta)$ plot (a fairly horizontal jump), which is observed right after F_c.

This study is just an attempt to gain some insight into this problem. A model allowing for vertical an horizontal displacements would be required to account for other dislocation configurations. However, a bifurcation analysis of this simple scalar model should yield a characterization of the threshold for nucleation and provide information on other possible configurations. More sophisticated approaches would be needed to handle a bigger sample with more dislocations.

5.5 CONCLUSIONS

We have presented simple examples of the application of a discrete scalar elasticity model to describe nucleation of edge dislocations in cracks of type I and II, and also in a nanoindentation experiment.

In the type I crack, we observed that after a certain opening of the crack, edge dislocations are nucleated at is tip. For a larger crack width, we seem to observe homogeneous nucleation of a dislocation dipole induced by the stress fields that are present, the dislocations of which gradually migrate to the boundaries of the domain for larger openings of the crack.

For the type II crack, we found an edge dislocation nucleated at its tip, which travels some distance apart from the crack tip and remains at equilibrium in the bulk of the sample.

Finally, we computed the critical value of the nanoindentation

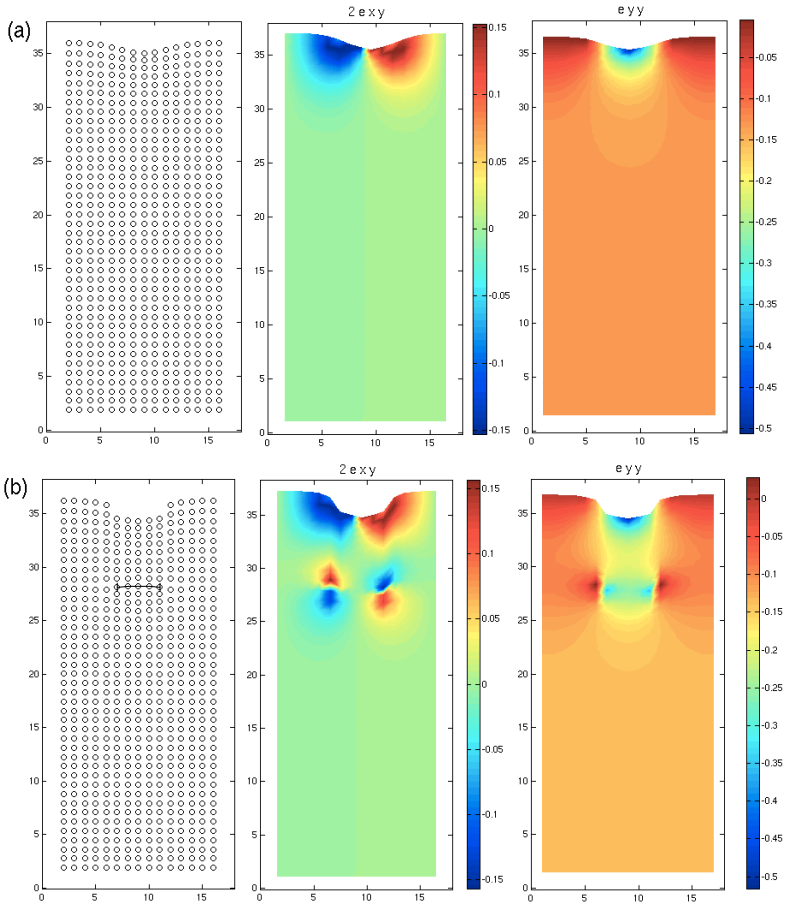

Figure 25. Atomic positions and strain field components $2e_{12}, e_{22}$ for relaxed equilibrium configurations obtained by numerical continuation for (a) $F_c = 0.51$ and (b) $F = 0.52$, corresponding to the data sets having the same labels in Fig. 24. In the latter, two dislocations have been nucleated at both sides of the nanoindentation tip, forming a dislocation loop that finds its equilibrium location some distance apart from the stress field generated by the tip.

load after which dislocation loops are generated, each one comprising two dislocations that are nucleated at both sides of the tip. These edge dislocations travel inward into the bulk of the sample, finding an equilibrium location some distance apart from the stress field generated by the tip. Monitoring the applied external force against the nanoindentation penetration depth shows in principle good qualitative agreement with experiments, at least for the stage in which dislocation loops are being generated. This may suggest that the simple model presented in this section might be refined in order find quantitative agreement.

6

CONCLUSIONS AND FUTURE WORK

In this thesis, we have formulated, analyzed and applied discrete models of dislocations in crystal lattices. Our main original results and conclusions are as follows.

In Chapter 2, we have generalized the discrete elasticity model of Ref. [33] for dislocations in cubic crystals in several directions. Firstly, we have shown how to treat fcc crystal lattices with a two-atom basis, such as those of silicon (diamond structure) and gallium arsenide (zincblende structure). Secondly, we have considered dissipative dynamics, thermal effects and fluctuations following the ideas of fluctuating hydrodynamics. Thirdly, we have illustrated perfect 60° and screw dislocations for fcc crystal lattices with two-atom basis.

In Chapter 3, we have studied homogeneous nucleation of edge dislocations in a sheared crystal lattice as the applied shear increases. We have used a much simpler model of scalar elasticity in two space dimensions: an overdamped IAC model [72] which is a caricature of the models in Chapter 2: the displacement vector has only one non-zero component (that along the x axis): $(u_{ij}, 0, 0)$, the distortion tensor has only two non-zero components, $D_1^+ u$ and $g_\alpha(D_2^+ u)$, and the derivatives of the periodic function g_a are dropped from the equations of motion. With these constraints the possible edge dislocations have Burgers vectors parallel to the x axis. The simplicity of the model allows a detailed study of bifurcations from the dislocation-free stationary configuration of the sheared lattice by using the AUTO program of numerical continuation. We have found multistable stationary configurations containing two or four edge dislocations for certain ranges of the applied shear stress. These solution branches issue from the dislocation-free solution branch via subcritical pitchfork bifurcations. Furthermore, we have been able to select these stable solutions by connecting the shear from zero stress to its final value according to a linear function of time that acts during a certain ramping time. Depending on the ramping time, numerical solution of the model shows that either one or two

edge dislocation dipoles are nucleated and split into dislocations with opposite Burgers vectors that then move to the lattice edges. We have also calculated the critical threshold of shear stress for dipole splitting to be one order of magnitude below the one for nucleation.

In Chapter 4, we have considered the problem of the appearance of dislocations in the InAs/GaAs(110) heteroepitaxy. This system was described by a two-dimensional discrete elasticity model without periodic functions. Instead, an algorithm to relabel atoms and calculate first neighbors was used. With this model, we have calculated the coherent and dislocated energy densities as functions of the thin film thickness. We have also calculated the critical thickness for the presence of interfacial misfit dislocations, in good agreement with the experimental value. By changing the misfit, we have shown by a simplified interface model that the system becomes linearly unstable for a certain critical misfit.

In Chapter 5, we have studied how dislocations may be generated near cracks and nanoindentors. We have used simplified scalar elasticity models adapted to the geometry of the problem at hand and solved them numerically. We have found that a crack of type I presents a critical opening width for which dislocations start nucleating at the crack tip and then remain close to it. For a crack of type II, when the external shear stress surpasses a critical value, a dislocation is nucleated at the crack tip and then travels to a certain distance apart from it. A nanoindentation experiment has been modeled so that the indentor penetrates in a two-dimensional sample with a certain dimensionless force that acts as a control parameter. When this force surpasses a critical value, a dislocation loop is nucleated at the sides of the indentor tip. Then the loop travels some distance apart from the indentor. The indentor force-penetration plot that we obtain has some resemblance with those measured in real experiments.

This thesis has shown how dislocations can be described by simple discrete elasticity models and ascertained how dislocations, dislocation dipoles and loops can be nucleated in different contexts. A lot of work can be done in the future work following the path open here. A possible list of future tasks is:

1. Extend the models in Chapter 2 to other crystal symmetries.
2. Study the effects of inertia on the homogeneous nucleation of dislocations in a sheared crystal. Clearly the stationary

solutions obtained in Chapter 3 are still solutions of the problem even if the dynamics is conservative. However, the stability of solutions will be different and oscillatory solutions about the stationary ones may appear and be important. The mechanisms to select different stable solutions will be different in the conservative case and it would be interesting to study the role of the energy as given by the initial conditions.

3. In the case of a heteroepitaxy considered in Chapter 4, develop an analytical theory of the critical thickness and possible bifurcations involving the appearance of dislocations. Considering the successful agreement with experiments that has been obtained, the discrete approach presented could be coupled with models describing island dynamics at larger scales [51].

4. Use numerical continuation of bifurcations to study the problems considered in Chapter 5, nanoindentation and dislocations generated at crack tips. Extend these studies to more realistic two and three-dimensional models.

A

THE PERIODIC FUNCTIONS IN THE DISCRETE MODELS

In this appendix we define the periodic functions which are used throughout the thesis to define the discrete gradients in the discrete elasticity models. We present a simple example of homogeneous shear to illustrate how these functions restore the translational invariance of the lattice. The experienced reader interested in definitions may skip it and go directly to Sec. A.2.

A.1 A PERIODIC LATTICE POTENTIAL

A.1.1 *Discretization of the strain energy*

Let us consider a two-dimensional crystal extended along the xy plane. In a continuum elasticity description, the strain energy density W depends on the displacement vector (u, v):

$$W = \frac{1}{2}C_{11}\left[\left(\frac{\partial u}{\partial x}\right)^2 + \left(\frac{\partial v}{\partial y}\right)^2\right] + C_{12}\frac{\partial u}{\partial x}\frac{\partial v}{\partial y} + \frac{C_{44}}{2}\left(\frac{\partial v}{\partial x} + \frac{\partial u}{\partial y}\right)^2 \tag{A.1}$$

where C_{11}, C_{12}, and C_{44} are the usual elastic constants.

Let us look for a discrete version of this energy. We have atoms labeled with indices (i, j) and displacements $(u_{i,j}, v_{i,j})$. Using the discrete differences $D_1^+ f_{i,j} = f_{i+1,j} - f_{i,j}$ and $D_2^+ f_{i,j} = f_{i,j+1} - f_{i,j}$

for any $f_{i,j}$, we define the following discrete strain energy:

$$\begin{aligned} V &= a^3 \sum_{i,j} \left\{ \frac{C_{11}}{2} \left[g\left(\frac{D_1^+ u_{i,j}}{a}\right)^2 + g\left(\frac{D_2^+ v_{i,j}}{a}\right)^2 \right] + \right. \\ &\quad + C_{12}\, g\left(\frac{D_1^+ u_{i,j}}{a}\right) g\left(\frac{D_2^+ v_{i,j}}{a}\right) + \\ &\quad \left. + \frac{C_{44}}{2} \left[g\left(\frac{D_1^+ v_{i,j}}{a}\right) + g\left(\frac{D_2^+ u_{i,j}}{a}\right) \right]^2 \right\}, \end{aligned} \tag{A.2}$$

where a is the lattice spacing and $g(x) \sim x$ for small x. Note that Eq. A.2 recovers the continuum limit in Eq. A.1 as $a \to 0$:

$$g\left(\frac{D_1^+ u}{a}\right) \sim \frac{\partial u}{\partial x}, \qquad g\left(\frac{D_2^+ u}{a}\right) \sim \frac{\partial u}{\partial y}, \tag{A.3}$$

and similarly for the v components. Notice that in Ch. 2 we normalize the discrete displacements $u_{i,j}/a \to u_{i,j}$ to the lattice parameter, so Eq.A.2 is rewritten in terms of $g(D_j^+ u_i)$.

A.1.2 *A periodic potential in homogeneous shear*

Let us consider now a simple system comprising only two chains of atoms extended along the x direction, such that $i = 1, ..., N_x$ and $j = 1, 2$. When the upper chain is displaced rigidly a distance x with respect to the lower one, the following energy results:

$$V(x) = N_x \frac{C_{44}}{2} g(x)^2, \tag{A.4}$$

since $D_2^+ u_{i,1} = x$ for all $i = 1, ..., N_x$ and any other discrete difference in Eq. A.2 vanishes. In more complex examples, the strain energy depends on many variables, but this case shows the importance of plotting $g(x)^2$ versus x. This plot provides a first insight into the influence of $g(x)$ in the energy profile

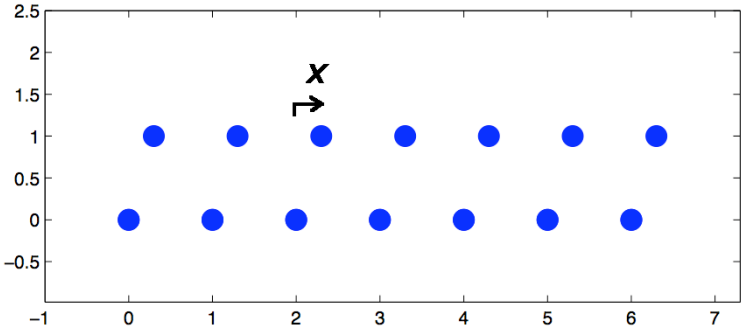

Figure 26. A system comprising only two chains of atoms spanned along the x direction, such that $i = 1, ..., N_x$ and $j = 1, 2$. The upper chain ($j = 2$) is displaced rigidly a distance x with respect to the lower one

.

arising from a relative displacement[1] of two chains of atoms. The resulting energy profile $V(x) \sim g(x)^2$ is the lattice potential associated to the shear displacement, x. Since $V(x)$ must have the lattice periodicity $a = 1$, we define functions with period one, $g_\alpha(x) = g_\alpha(x + 1)$. Fig. 27 shows plots corresponding to functions $g_\alpha(x)$ whose definition is given in Sec. A.2.1. In this section, we are interested in having a first insight into how the lattice potential shown in Eq. A.4 depends on 2α, which is the width of the positive-slope regions of $g_\alpha(x)$.

Note that $\alpha = 0.25$ corresponds to

$$g_{0.25}(x) = \sin(2\pi x)/(2\pi), \tag{A.5}$$

as shown in Fig. 27 (a). It is observed that $g(x)^2$ has minima not only at integer values of x, but also at semi-integer ones, which might correspond to actual potential curves (see Eq. 8-40 and Fig. 8-9 (b) in Ref. [14]).

The functions $g_\alpha(x)$ may be calibrated to fit different atomic-bond strengths. Note the wide potential wells at integer values of

1 This relative displacement is performed along a periodic (i.e., primitive) direction.

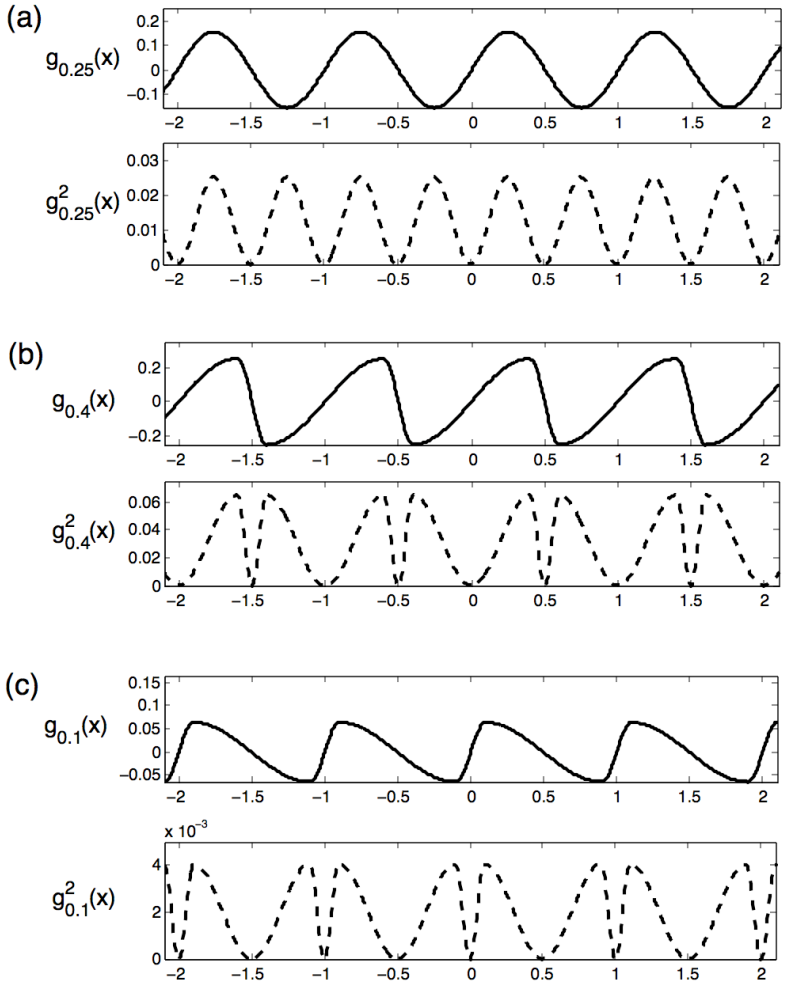

Figure 27. (see Ch. 5)

x and the high barriers obtained for $\alpha = 0.4$ (Fig. 27 (b)), whereas for $\alpha = 0.1$ these valleys are narrower and the barriers are lower (Fig. 27 (c)). Perfect lattice configurations correspond to integer values of x, and are easier to be reached for higher values of α. In the other hand, non-perfect lattice configurations which correspond to semi-integer values of x, are easier to be found for lower values of α.

Concerning the motion of dislocations, the parameter α determines the size of the dislocation core and the Peierls stress needed for a dislocation to start moving [33]. As α increases, so does the Peierls stress, whereas both the core size and the mobility of defects decrease. High values of α result in very narrow

cores and large Peierls stresses.

A.2 DEFINITIONS

A.2.1 *Sinusoidal functions*

Let us define the periodic function $g_{\alpha,\epsilon}(x) = g_{\alpha,\epsilon}(x+1+\epsilon)$ with $0 < \alpha < 1/2$ and $0 < \epsilon < 1$ as the periodic extension of

$$g_{\alpha,\epsilon}(x) =$$

$$\begin{cases} \frac{2\alpha(1+\epsilon)}{\pi} \sin\left(\frac{\pi x}{2\alpha(1+\epsilon)}\right), & -\alpha(1+\epsilon) \le x \le \alpha(1+\epsilon), \\ \frac{2\alpha(1+\epsilon)}{\pi} \sin\left(\frac{\pi}{2} \cdot \frac{\frac{x}{1+\epsilon}-1/2}{\alpha-1/2}\right), & \alpha(1+\epsilon) \le x \le (1-\alpha)\cdot(1+\epsilon), \end{cases} \tag{A.6}$$

in subsequent intervals $((-\alpha+p)\cdot(1+\epsilon), (1-\alpha+p)\cdot(1+\epsilon))$, ($p$ being any integer). The derivative of this function is the corresponding periodic extension of:

$$g'_{\alpha,\epsilon}(x) =$$

$$\begin{cases} \cos\left(\frac{\pi x}{2\alpha(1+\epsilon)}\right), & -\alpha(1+\epsilon) \le x \le \alpha(1+\epsilon), \\ \frac{\alpha}{\alpha-1/2} \cos\left(\frac{\pi}{2} \cdot \frac{\frac{x}{1+\epsilon}-1/2}{\alpha-1/2}\right), & \alpha(1+\epsilon) \le x \le (1-\alpha)\cdot(1+\epsilon). \end{cases} \tag{A.7}$$

We use $g_{\alpha,\epsilon}(x)$ in problems concerned with heteroepitaxial growth, where there are two different lattice spacings: the substrate with lattice constant equal to one, and the film whose lattice parameter is $1+\epsilon$. We use $g_{\alpha,0}(x)$ to define the gradients within the substrate and $g_{\alpha,\epsilon}(x)$ within the epilayer. See Sec. 4.3 in Ch. 4.

In cases where there is only one type of material, its lattice spacing is normalized to unity and we use a simplified notation:

$$g_\alpha(x) \equiv g_{\alpha,\epsilon=0}(x), \quad g'_\alpha(x) \equiv g'_{\alpha,\epsilon=0}(x). \tag{A.8}$$

As an example, $g_{0.25}(x) = \sin(2\pi x)/(2\pi)$, $g'_{0.25}(x) = \cos(2\pi x)$. We are merely extending the definition of sinusoidal functions. See Fig. 27. Note that the functions we define are c^∞, so the resulting models in which they are used are suitable for analysis and in principle well-behaved in numerical schemes.

A.2.2 *Piecewise linear functions*

It is possible to define also a piecewise linear set of functions as:

$$g_\alpha(x) = \begin{cases} x & \text{if } -\alpha \leq x \leq \alpha, \\ \\ -\alpha \left(\frac{x-1/2}{\alpha-1/2} \right) & \text{if } \alpha \leq x \leq 1-\alpha. \end{cases} \tag{A.9}$$

These functions recover $g_\alpha(x)^2$ profiles similar to those of the sinusoidal functions, but now they give rise to a sequence of quadratic wells. The piecewise linear $g_\alpha(x)$ have positive slope in regions whose width is 2α. This fact allows us to compare the definitions in Eqs. A.9 and those in A.6 easily. See comment on other definitions[2].

A.2.3 *Non-periodic functions*

In Sec. 4.2 of Ch. 4, a relabeling algorithm is used and no periodic functions are needed. We use two different functions: $g_1(x) = x$, which is purely linear, and $g_2(x) = \tan^{-1}(\pi x)/\pi$, is not harmonic.

2 The reader interested in definitions of the piecewise linear functions in Refs. [33, 34] should note that $\alpha_{\text{Refs. [33, 34]}} = 1/2 - \alpha_{thesis}$. This is due to the fact that in those references, $2\alpha_{\text{Refs. [33, 34]}}$ is the width of those regions having *negative* slope.

Any discrete model presents advantages and limitations. In the following, we analyze the advantages (Sec. A.3.1) of the discrete elasticity models using periodic functions, then explain why we needed to introduce relabeling of atoms due to the limitations of the periodic-functions approach (Sec. A.3.2) and discuss which of these models might be convenient depending on the purposes to be achieved (Sec. A.3.3).

A.3.1 *Periodic functions: advantages*

The main reason to use periodic functions was illustrated with the previous example in homogeneous shear (Sec. A.1): when two chains of atoms are rigidly displaced with respect to one another, a periodic strain energy profile is recovered. Defining the discrete gradients as a periodic function of the discrete differences, $g(D_j^+ u_i)$, accounts for that. As already mentioned, the definitions we present (Eqs. A.6) may be fit to different atomic-bond strengths.

Let us illustrate the advantage of using periodic functions in Sec. 3.2 of Ch. 3.

Observe panel (b) in Fig. 10 of Ch. 3, in which the strain field component has been defined as $2e_{12} = g_\alpha(u_{i,j+1} - u_{i,j})$. This definition was introduced in order to have consistency with the dynamical system of equations

$$m\frac{\partial^2 u_{i,j}}{\partial t^2} + \beta\frac{\partial u_{i,j}}{\partial t} = u_{i+1,j} - 2u_{i,j} + u_{i-1,j} + A\left[g_\alpha(u_{i,j+1} - u_{i,j}) + g_\alpha(u_{i,j-1} - u_{i,j})\right]. \tag{A.10}$$

In Ch. 3, we defined the discrete strain components as $2e_{12} = g_\alpha(u_{i,j+1} - u_{i,j})$. *What would the usual discrete elasticity strain field* $2e_{12} = u_{i,j+1} - u_{i,j}$ *have looked like?* The answer is shown in Fig. 28 (b). It is clear that the usual discrete elasticity definition does not describe correctly the strain fields. While in panel (b) the strain field is affected uniformly in a wide range in the x axis, in panel (c) our definition for $2e_{12}$ accurately localizes the spots

where dislocations are present. In between them, the strain field is close to zero, which corresponds to regions where a fairly perfect lattice is found. This represents a great advantage: in panel (a) we have to interpret the information and draw by hand the $\top$ and $\perp$ symbols where we find the dislocations, but in panel (c) we immediately see their location. So we may run our simulations and identify spots in the e_{12} plot where nucleation might take place.

Another advantage of using continuous functions in system A.10 is related to avoiding atomic relabeling. On the one hand, this may become a problem when several dislocations are present in the system, as will be discussed in Sec. A.3.2. On the other hand, if we agree on panel (c) in Fig. 28 being a good representation of the strain field of the configuration shown in panel (a), then we acknowledge system A.10 as a good approximation for describing the dynamics in our lattice. Since no atomic relabelling is performed, the computational grid remains unchanged and the dynamical system is the same during all the simulation. This means that *instabilities, bifurcations and topological transitions can be analyzed in a precise manner*, as we did for the first time in the homogeneous nucleation problem [37]. This certainly represents an advantage of this discrete elasticity approach.

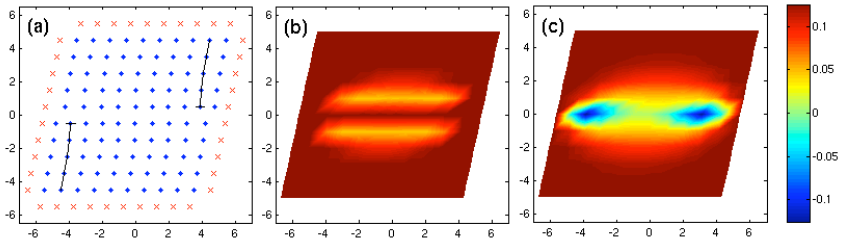

Figure 28. Three representations corresponding to the same relaxed configuration: (a) Atomic positions corresponding to the displacement field u_i, and strain component (b) $2e_{12} = u_{i,j+1} - u_{i,j}$ in usual discrete elasticity and (c) $2e_{12} = g_\alpha(u_{i,j+1} - u_{i,j})$ using Eq. A.6. Parameters: $A = 0.3071$, $\alpha = 0.2$ and final shear strain at the boundary $F_f = 0.22$ reached after a ramping time interval $t_r = 85$ (see Ch. 4).

.

A.3.2 *Periodic functions: limitations*

In Ch. 4 no periodic functions are used and a relabeling algorithm is implemented. In Ch. 4 it is mentioned that this is done in order to ensure the surface depressions to be found right above the corresponding dislocation which induces the strain field. What would had happened if periodic functions had been used? Maintaining the computational grid unchanged, results in leaving as *computational neighbors* atoms that are already far apart. In principle, this would still allow the system to recover minima of the strain energy density in regions where a perfect lattice is found, but may cause *shifts of information* of the order of the total Burgers vector.

See Fig. 29. An example of heteroepitaxial growth is shown, in which five layers of epilayer have been deposited onto a substrate. Even though the Ge/Si heteroepitaxy typically forms mountains, for illustrative purposes we inserted the lattice constants of Ge and Si assuming that a layer by layer growth takes place in a square lattice. Anyhow, the important issue is that the epilayer has 4% larger lattice constant than the substrate.

Arrows (a) and (b) in Fig. 29 point towards the valleys which are induced by the buried dislocations. At the interface, atoms close to the dislocation core which are *computational neighbors* are highlighted in black color. What do we mean here by computational neighbors? Look at atoms in black below label (a). Let their displacements be $u(a,p)$ for the one in the substrate and $u(a,p+1)$ for the one in the thin film. The computational grid is a $N_x \times N_y$ *square* lattice, so atoms (a,p) and $(a,p+1)$ are *vertically* connected whenever a *vertical* discrete difference $D_2^+ u(a,p) = u(a,p+1) - u(a,p)$ is computed. In the case of these two atoms, they may be considered as vertically aligned below arrow (a) with an error of at most one lattice period. The actual core structure of an edge dislocation does not require that these atoms be aligned, since two atoms of the film should lie above three atoms of the substrate, roughly speaking. The subtle issue is to compute the largest error that we are doing when assuming that D_2^+ is a *vertical* discrete difference. We observe this error to be at most of the order of the Burgers vector $b \sim 1$. We could trust the dislocation core found below arrow (a) as a good approximation.

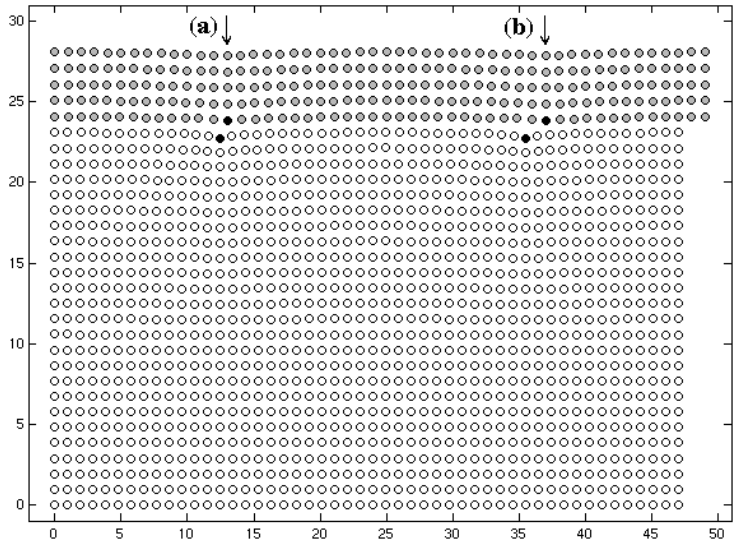

Figure 29. Heteroepitaxial system with 4% misfit ($\epsilon = 0.04$) described by periodic functions. As opposed to the results shown in Fig. 15 (Sec. 4.2 in Ch. 4), the valleys (a) and (b) formed on top the dislocations are not vertically aligned with them. This is due to the fact that the computational grid remains unchanged: atoms colored in black are computational neighbors. The shifts of information at the interface are smaller than ~ 1 and ~ 2 lattice periods below arrows (a) and (b), respectively. The upper bound for these shifts of information is the total Burgers vector, $b = 2$.

In the case of arrow (b), it points towards atom $(b, p+1)$, which is not right above atom (b, p). So the valley observed in the surface below arrow (b) is not vertically aligned on top of the dislocation core (b, p) atom in the substrate. In this case, taking $D_2^+ u(b, p) = u(b, p+1) - u(b, p)$ as a *vertical* difference is a stronger assumption. The error of assuming atoms $(b, p+1)$ and (b, p) to be vertically aligned (as they are in the computational grid) results in a shift of the physical information of at most two lattice periods, which is the total Burgers vector of the system.

A more clear way to understand this idea is to look at the atoms at the right boundary in the sample: the one belonging to the substrate (N_x, p) is found at $x \sim 47$, while the one in the film

is at $x \sim 49$. There is a gap in their x coordinates of around two lattice positions, so the fact that they remain as computational neighbors results in $D_2^+ u(N_x, p) = u(N_x, p+1) - u(N_x, p)$ not being an actual *vertical* discrete difference, so the assumption of it recovering the continuum gradient $\partial u / \partial y$ is not really accurate at the interface.

These issues are efficiently handled in Sec. 4.2 of Ch. 4 by doing a careful relabeling of the atoms, ensuring that computational neighbors are actual neighbors in the crystal lattice. An accurate description is achieved, recovering the appropriate qualitative behavior and good quantitative agreement with the experimental critical thickness measured in the InAs/GaAs(110) heteroepitaxial system. We modeled $8, 16, 24$ and even 32 dislocations finding the valleys right on top of the dislocation cores.

In Sec. 4.3 of Ch. 4, we use again the periodic-functions approach in order to have a dynamical system that remains unchanged and allows us to perform a linear stability analysis and find the critical misfit for which the defect-free system becomes unstable.

A.3.3 *What model should be chosen?*

Hopefully, the advantages and limitations in the models used throughout this thesis could help the interested reader to choose a convenient model for his/her own use:

- **Discrete elasticity models using periodic functions:**
  - The computational grid and the dynamical system remain unchanged: bifurcation analysis is possible, but shifts of information scaling with the total Burgers vector may represent a limitation for increasing number of dislocations.
  - These models have been proven useful to model nucleation of dislocations efficiently. There is no need of a priori knowledge of the location where dislocations may nucleate, since nucleation is precisely the output phenomenon found in the simulations.
- **Discrete elasticity models with relabeling algorithms:**

– An accurate description of the strain fields is obtained, regardless of the number of dislocations. Atoms which are neighbors in the crystal are also neighbors in the computational grid.
– The dislocations must be set a priori in the system, with special attention to areas where slip may take place, in order to develop an algorithm to update the first neighbors stencil of dependencies in the computational grid.
– No nucleation process can be observed as a natural output, and no stability analysis seems to be possible, since the dynamical system would change when slip of atoms takes place.

B

ADDITIONAL RESULTS ON NUCLEATION

B.1 BIFURCATION DIAGRAM FOR $\alpha = 0.4$ AND $A = 0.3071$ IN A 6X6 LATTICE

We present here the results found for $\alpha = 0.4$, $A = 0.3071$ in a 6x6 lattice, where $F_c = 0.402701$. See the bifurcation diagram shown in Fig. 30. Here we depict three branches. Their unstable parts usually have depressions in the e_{12} strain component similar to those observed in dynamical simulations where dipoles are being formed.

Consider their stable parts:

- BR1 has two stable parts: one with larger norm than that of BR0, the other with smaller norm. The configuration of the solutions in the stable part of BR1 with norm larger than that of BR0 contains two edge dislocations of opposite Burgers vectors that originate from the splitting of *one dipole at* $y = 0$. The configurations corresponding to the lower part of BR1 ($||u||_{BR1} < ||u||_{BR0}$, larger values of F in the diagram) contains four additional edge dislocations originating in the splitting of two additional dipoles appearing at $y = \pm 3$.
- Similar to BR1, BR2 has two stable parts with norms larger and smaller than that of BR0, respectively. The configurations corresponding to the upper part of BR2 have four edge dislocations with Burgers vectors $(\pm 1, 0, 0)$ originating from the splitting of *two dipoles at* $y = \pm 1$. The configurations corresponding to the lower part of BR2 contain four additional edge dislocations originating from the splitting of two additional dipoles at $y = \pm 3$.
- The main stable part of BR3 has norm smaller than BR0 and contains two edge dislocations of opposite Burgers vectors that originate from the splitting of *two dipoles at* $y = \pm 3$; see Fig. 31.

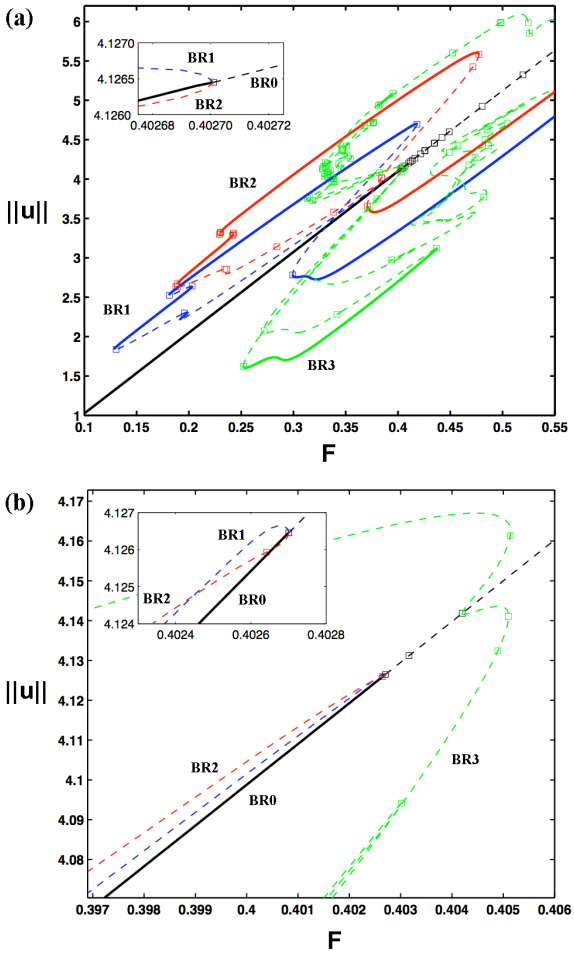

Figure 30. (a) Bifurcation diagram showing the stationary branches BR1, BR2 and BR3, which have dislocation dipoles at $y = 0$, $y = \pm 1$ and $y = \pm 3$, respectively. The stable parts of BR1 and BR2 which have l^2-norm smaller than $||u||_{BR0}$ have also dipoles at $y = \pm 3$. (b) A closer view showing BR1 and BR2 issuing from $F_c = 0.4027$ and BR3 issuing from the third bifurcation point found in BR0 at $F = 0.4042$. In all cases, solid lines correspond to stable solutions, dashed lines to unstable solutions and bifurcation points are marked as squares.

Table 4 shows our results in the ramping experiments. There is no intermediate ramping time t_r giving rise to BR1 configurations.

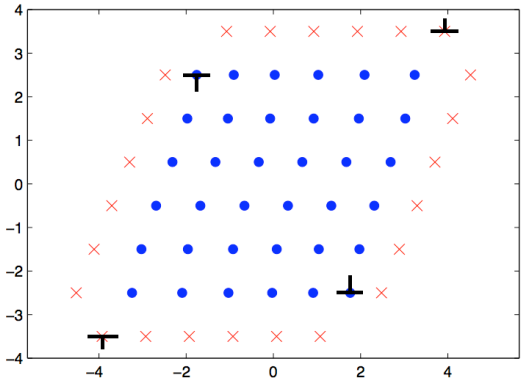

Figure 31. Equilibrium configuration for $F = 0.40778$ corresponding to the stable part of branch BR3 found in Fig. 30 for a 6x6 lattice with $A = 0.3071$ and $\alpha = 0.4$. The dipoles are formed at $y = \pm 3$ and they are split: they comprise dislocations which find equilibrium locations at the sides of the domain.

Only BR2 and BR3 were found in our dynamical experiments.

Final stress, F_f	Ramping time, t_r	Nucleation height, y	Branch
0.402701	$t_r \geq 645$	± 1	BR2
0.402701	$t_r \leq 640$	± 3	BR3
0.402705	$t_r \geq 645$	± 1	BR2
0.402705	$t_r \leq 640$	± 3	BR3
0.403500	$t_r \geq 811.5$	± 1	BR2
0.403500	$t_r \leq 811.0$	± 3	BR3
0.402900	$t_r \geq 675.6145$	± 1	BR2
0.402900	$t_r \leq 675.6144$	± 3	BR3

Table 4. Results obtained for a 6x6 lattice with $A = 0.3071$ and $\alpha = 0.4$. The final stress F_f, and the ramping time t_r, determine the height y at which the dislocation dipoles are nucleated. As opposed to the results shown in Table 1 for the $\alpha = 0.4$ case in a 10x10 lattice, here we find no t_r giving rise to a BR1 configuration.

B.2 SECONDARY BRANCHES FOR $\alpha = 0.25$ AND A $= 1$ IN A 6X6 LATTICE

In this case we show two secondary branches SBR1 and SBR2 which bifurcate from BR2. They are stable in certain stress ranges as shown in Fig. 32 (b). Actually, each of these lines represent two solution branches having the same l^2 norm. In their stable ranges, the configurations of SBR1 and SBR2 exhibit two and four edge dislocations originating from splitting of one and two dipoles, respectively. The configurations of SBR1 mimic those of BR1, but their two edge dislocations are not centered: they are shifted upwards (for one of the solution branches having the same norm) and downwards (for the other solution branch). A reflection from the horizontal axis crossing the lattice center transforms one configuration in the other. In the case of SBR2, there are only two narrow ranges of F in which the stationary solutions are stable. The range closer to the upper part of branch BR2 is

similar to that described before for SBR1, but now there are four edge dislocations instead of two. The other range with smaller values of F produces configurations that are more curious: while two edge dislocations have moved to the boundaries in opposite directions, the other two dislocations form either a dipole or a dislocation loop *inside the lattice*, depending on which of the two solutions with the same l^2 norm is considered. It turns out that the strain fields of these two solutions have opposite signs at each lattice point.

The main branches BR1 and BR2 and the results obtained in the overdamped dynamics experiments are similar to those explained in Ch. 3 for the 10x10 lattice with $A = 0.3071$ and $a = 0.2$, as Fig. 33 shows. In panels (a) and (d), we include snapshots of the early stages. The critical shear here is $F_c = 0.258295$.

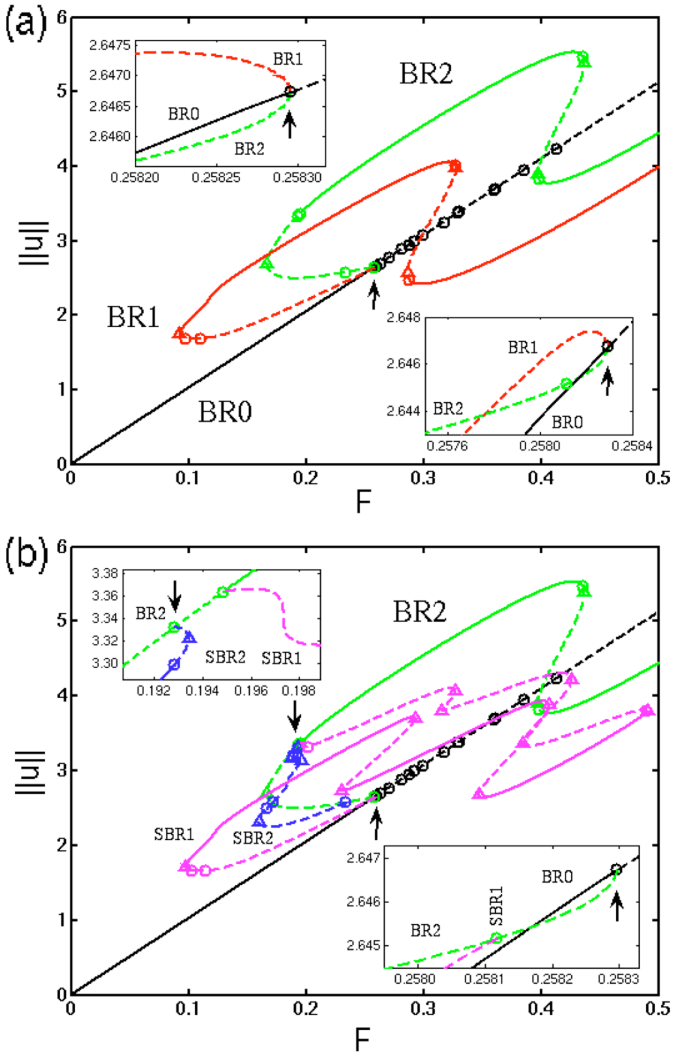

Figure 32. (a) Bifurcation diagram showing only the primary stationary branches issuing from the homogeneous solution BR0. At F_c, branches BR1 and BR2 appear as a subcritical pitchfork bifurcation from BR0 (see the insets). (b) Bifurcation diagram in which BR1 has been omitted and secondary bifurcation branches SBR1 and SBR2 issuing from BR2 are shown. Zooms near the bifurcation points are shown in the insets. In all cases, solid lines correspond to stable solutions, dashed lines to unstable solutions, limit points are marked as triangles and bifurcation points as circles. Parameter values are: $A = 1$, $a = 0.25$.

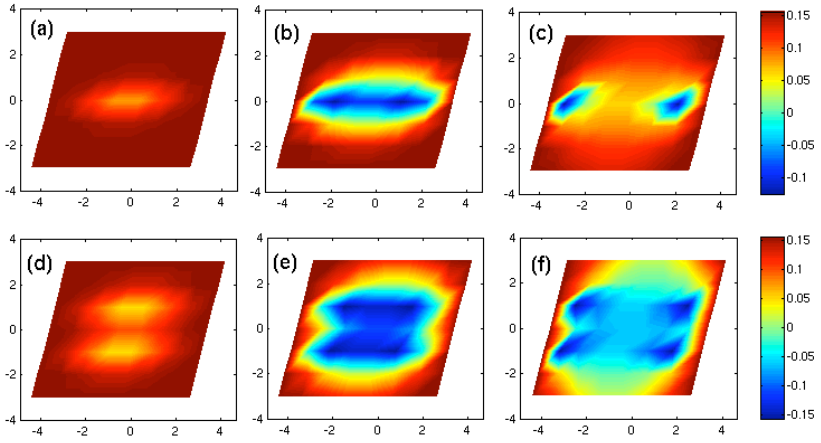

Figure 33. Dipole nucleation in overdamped dynamics for a 6x6 lattice with $A = 1$ and $\alpha = 0.25$. Upper panel from left to right: Snapshots of the strain $2e_{12}$ at times (a) 280.8, (b) 282.9, (c) 377.8 for the evolution towards BR1 with ramping time $t_r = 85$ ($c = 3.047 \times 10^{-3}$). Lower panel from left to right: Same at times (a) 302.4, (b) 304.7, (c) 393.0 for the evolution towards BR2 with ramping time $t_r = 100$ ($c = 2.59 \times 10^{-3}$). $F_f = 0.259$.

C

NUMERICAL CONTINUATION

The numerical continuation technique which is widely used throughout this thesis is explained in this appendix.

Let us consider the following N-dimensional dynamical system for the vector $\mathbf{u}(t)$:

$$\frac{d\mathbf{u}}{dt} = \mathbf{f}(\mathbf{u}; F), \tag{C.1}$$

in which F is a constant parameter.

We want to study the linear stability of the stationary solutions of the system C.1 for different values of F. Starting with a given fixed value $F = F_0$ for which the system has a linearly stable stationary solution $\mathbf{u}^*(F_0)$, we set an initial condition $\mathbf{u}(t_0)$, and then solve:

$$\begin{aligned} \frac{d\mathbf{u}}{dt} &= \mathbf{f}(\mathbf{u}; F_0), & \text{(C.2)} \\ \mathbf{u}(t_0) &= \mathbf{u}_0. & \text{(C.3)} \end{aligned}$$

This system evolves until a stationary configuration $\mathbf{u}(\mathbf{t}_\infty) \rightarrow \mathbf{u}^*(\mathbf{F_0})$ is reached[1].

We find the Jacobian matrix $\mathbf{J}(\mathbf{u}^*(F_0))$ of the system C.2-C.3 linearized about the stationary solution $\mathbf{u}^*(F_0)$ and calculate its eigenvalues. The linear stability of $\mathbf{u}^*(F_0)$ depends on the sign of the maximum eigenvalue, $\lambda_{max}(F_0)$ (or the maximum real part, in case of complex eigenvalues). Configurations $\mathbf{u}^*(F_0)$ are linearly stable when $\lambda_{max}(F_0) < 0$, and unstable if $\lambda_{max} \geq 0$.

1 We use the same letter for the general $\mathbf{u}(t)$ and the relaxed $\mathbf{u}^*(F)$, since the asterisk tells the difference.

Starting with F_0, we follow a sequence $F_0 < F_1 < ... < F_n$, firstly inserting $\mathbf{u}^*(F_0)$ as initial condition for a new problem with $F = F_1$,

$$\frac{d\mathbf{u}}{dt} = \mathbf{f}(\mathbf{u}; F_1), \tag{C.4}$$

$$\mathbf{u}(t_0) = \mathbf{u}^*(F_0), \tag{C.5}$$

and solving the subsequent problems for increasing values of F. When do we stop? We monitor $\lambda_{max}(F)$ and identify the critical value F_c for which $\lambda_{max}(F_c) = 0$. We can also perform one more step for $F_n > F_c$, in order to observe the new configuration reached by the system after the instability.

In order to proceed numerically, F_c may be taken as that F whose corresponding $\lambda_{max}(F)$ more closely approaches zero from negative values. Other possibility is to perform the numerical continuation without analyzing the linearized system, in order to get a faster but more superficial impression about the dependence of the stationary solutions on F.

D

RESUMEN EN ESPAÑOL

D.1 INTRODUCCIÓN

La comprensión del comportamiento de los defectos presentes en las redes cristalinas es esencial para el diseño y fabricación de dispositivos nanoelectrónicos porque afectan fuertemente sus propiedades electrónicas, ópticas y magnéticas. Asimismo, defectos como las dislocaciones son esenciales para el proceso de crecimiento de estructuras heteroepitaxiales, para entender la propagación de fisuras o en experimentos de nanoindentación que tratan de aclarar el comienzo de la plasticidad.

En la presente tesis doctoral se formulan modelos discretos de dislocaciones en redes cristalinas del sistema cúbico (simple, centrado en las caras o centrado en el cuerpo, con la posibilidad de incluir una base de varios átomos en cada nodo de la red) que recuperan la elasticidad lineal anisotrópa en su límite continuo. En la tesis se analiza la nucleación homogénea de dislocationes en un cristal bidimensional sujeto a tensiones de cizalladura y se concluye que los estados con dislocaciones aparecen como bifurcaciones subcríticas del estado estacionario sin dislocaciones. Las ramas bifurcadas multiestables se calculan por métodos de continuación numérica y se estudia su selección mediante ramping de la tensión de cizalla. También se calculan valores críticos para la formación de dislocaciones en sistemas heteroepitaxiales, así como en fisuras y experimentos de nanoindentación.

A continuación se resume el contenido de los capítulos 2, 3, 4 y 5 de la tesis explicando las aportaciones originales del trabajo, la metodología empleada y las conclusiones alcanzadas. Por último, se explican las líneas de trabajo futuro que se abren a raíz del trabajo presentado en esta memoria.

D.2 RESUMEN DEL CAPÍTULO 2

D.2.1 *Aportaciones originales*

En el capítulo 2, se generalizan los modelos de elasticidad discreta de la Ref. [33] para cristales con simetría cúbica en diversos sentidos:

- Se proponen modelos para describir cristales fcc cuya base conste de dos átomos, como es el caso del silicio (estructura de diamante) y del arseniuro de galio (estructura de cinc-blenda).
- Se formulan dichos modelos considerando dinámica disipativa, efectos térmicos y fluctuaciones.
- Se define una familia de funciones sinusoidales (Apéndice A) que permiten calibrar la dureza de los enlaces y son C^∞, siendo aptas para el análisis matemático y la implementación numérica.
- Se construyen dislocaciones perfectas de 60° y en hélice para redes fcc con una base de dos átomos (GaAs).
- De igual forma que en el caso de la cadena lineal diatómica, en cuya relación de dispersión aparecen ramas acústicas y ópticas, se espera que la dinámica de los modelos discretos propuestos para cristales con una base de dos átomos aporte mayor información que sus límites continuos.

D.2.2 *Metodología*

Los modelos discretos [33] se basan en la sustitución de los gradientes en la expresión de la energía elástica por una función periódica de las diferencias discretas expresadas en las coordenadas primitvas. Así, se aprovecha la periodicidad de la red a lo largo de estas coordenadas para que la función periódica reestablezca los mínimos de la energía elástica cada vez que una cadena de átomos se desplace un número entero de veces a lo largo de una dirección primitiva (A). Por otro lado, se insertan las

constantes elásticas que permiten recuperar la elasticidad lineal anisotrópa como límite continuo de estos modelos.

La formulación de los modelos discretos para las estructuras de cinc-blenda y diamante se desarrolla definiendo las diferencias discretas atendiendo a la geometría de la red. Se introducen vectores auxiliares que conectan los átomos de las dos redes fcc que conforman el cristal. El tensor de deformaciones es definido en cada nodo de la red promediando las diferencias discretas asociadas a los dos átomos que conforman la celda unidad del cristal.

La disipación se añade a los modelos considerando una función cuadrática disipativa con simetría cúbica. En cuanto a las fluctuaciones, se incluyen recurriendo a las ideas provenientes de la hidrodinámica [40, 41]. Se calcula la producción de entropía como la suma generalizada de fuerzas y flujos. Entonces se identifican fuerzas y flujos y las relaciones lineales entre ellos conllevan las correlaciones de las magnitudes fluctuantes que deben añadirse a las ecuaciones del movimiento.

Se define en el apéndice A un nuevo conjunto de funciones sinusoidales g_α que permiten calibrar la dureza de los enlaces atómicos. Al igual que en las funciones lineales a trozos, el parámetro α determina el tamaño del núcleo de las dislocaciones y la barrera de Peierls necesaria para poner una dislocación en movimiento. La tensión de Peierls aumenta con α, mientras que el tamaño del núcleo y la movilidad de las dislocaciones decrecen. Valores altos de α conllevan núcleos de dislocación estrechos y barreras de Peierls altas [33, 34]. Las nuevas funciones son C^∞, resultando aptas para el análisis matemático y la implementación numérica.

D.3 RESUMEN DEL CAPÍTULO 3

D.3.1 *Aportaciones originales*

- Al aplicar una deformación de cizalla a un cristal descrito en dos dimensiones por un modelo de elasticidad escalar, distintas configuraciones de equilibrio bifurcan respecto de la rama que corresponde a la deformación homogénea. Una

bifurcación *pitchfork* subcrítica tiene lugar para un valor crítico $F = F_c$ de la tensión aplicada.

- La continuación numérica de soluciones estacionarias muestra que las ramas que bifurcan de la principal en F_c corresponden a configuraciones en las que se han nucleado dos o cuatro dislocaciones.

- Seleccionando un valor final de la tensión aplicada $F_f > F_c$, el sistema puede evolucionar hasta una u otra configuración aplicando una tensión $F = F_f\, t/t_r$ durante diferentes intervalos de tiempo t_r. Transcurrido cierto tiempo tras t_r, se nuclean uno o dos dipolos y las dislocaciones de que se componen viajan en sentidos opuestos hacia las paredes del dominio computacional.

- La tensión crítica $F_{c,dip}$ necesaria para separar las dislocaciones de un dipolo insertado como condición inicial es $F_{c,dip} \sim \alpha/10$, un orden de magnitud por debajo del valor crítico $\sim \alpha$ obtenido para la nucleación. El parámetro α es el definido para las funciones g_α (Ap. A). Esto explica por qué los dipolos al nuclearse se disgregan inmediatamente, viajando sus dislocaciones en direcciones opuestas según el signo de su vector de Burgers.

D.3.2 *Metodología*

Se utiliza el programa AUTO para la continuación numérica de soluciones [1]. Ello permite la elaboración de un diagrama de bifurcación en el que se representa la norma l^2 frente a la deformación aplicada en la frontera del sistema. Se representan las diferentes ramas encontradas en el diagrama, hallándose que las dos ramas principales emergentes como inestables del primer punto crítico corresponden a dipolos de dislocaciones nucleados en las regiones centrales del dominio. Se presentan experimentos de dinámica sobreamortiguada con distintas rampas en cuanto al aumento en el tiempo de la tensión de cizalladura, observándose que para un mismo valor final de la tensión de cizalladura el sistema puede evolucionar a distintas configuraciones finales.

El valor crítico de la tensión de nucleación F_c se halla también mediante el procedimiento de continuación numérica descrito en el Ap. C, coincidiendo con el valor hallado con AUTO.

Se analiza el autovector ψ asociado al autovalor $\lambda_{max}(F_c) = 0$, encontrándose que sus componentes son mayores para regiones centradas en la muestra. El estudio de las componentes de dicho vector permite identificar que las ramas nacen como $+\psi$ o $-\psi$, lo cual determina, tras otras bifurcaciones que sufren estas ramas, la formación de uno o dos dipolos, respectivamente.

En un nuevo experimento, estableciendo un dipolo de dislocaciones como condición inicial, se calcula el valor de la tensión crítica $F_{c,dip}$ necesaria para separar sus dislocaciones. La condición inicial es el campo lejano de deformación usual simplificado al caso que cumple las ecuaciones de la elasticidad escalar. A dicho campo se le añade el valor adicional de la deformación F en la frontera, que se mantiene fijo en cada simulación. Relajando al equilibrio sucesivos valores crecientes de F, se halla el valor crítico $F_{c,dip} \sim \alpha/10$.

En el Apéndice B se muestra un estudio más detallado sobre una tercera rama estacionaria a la que se llega en los experimentos de dinámica sobreamortiguada para t_r menores. Asimismo, se muestra un ejemplo en el que se estudian algunas ramas secundarias.

D.4 RESUMEN DEL CAPÍTULO 4

D.4.1 *Aportaciones originales*

- Se presenta un modelo de elasticidad discreta en dos dimensiones capaz de describir el campo de deformaciones en la superficie del sistema heteroepitaxial InAs/GaAs(110).
- Se calcula con dicho modelo las densidades de energía elástica correspondientes a la configuración del sistema con dislocaciones y sin ellas, calculando un valor del espesor crítico de la película delgada muy próximo al experimental.
- Se ilustra el concepto de discrepancia crítica (*misfit* crítico) entre los parámetros de red del sustrato y de la película crecida sobre el mismo, mediante argumentos de estabilidad lineal.

D.4.2 *Metodología*

En primer lugar, se explican las diferentes etapas del crecimiento InAs/GaAs(110). En la primera parte del capítulo, se modela la segunda etapa, correspondiente a un grosor de entre 3 y 100 monocapas. Puesto que el crecimiento es capa a capa, no es necesario tener en cuenta efectos de reconstrucciones ni otros accidentes en la superficie. Mediante una rotación de coordenadas, se logra seleccionar un plano representativo que simplifica extraordinariamente el problema, reduciéndolo a dos redes cuadradas con distinto parámetro de red, una de In crecida sobre otra de Ga. Se consideran los desplazamientos de los átomos en las dos dimensiones contenidas en el plano que conforma el dominio seleccionado. Se definen los gradientes discretos siguiedo la metodología expuesta en el capítulo 1, pero en este caso no se utilizan funciones periódicas, sino que se recurre a un algoritmo que actualiza las listas de primeros y segundos vecinos. De esta manera, se evita mantener como vecinos en la malla computacional a aquellos átomos cuyas posiciones quedan alejadas (Ap. A). Esto es importante para asegurar que los valles superficiales debidos al campo de deformación creados por las dislocaciones se observen verticalmente alineados sobre las mismas, tal y como ocurre en el experimento de referencia [69]. Se imponen como condición inicial configuraciones con distinto número de capas, las cuales se relajan al equilibrio mediante una dinámica sobreamortiguada (es entonces cuando se forman los valles sobre las dislocaciones), y se calcula la energía resultante del sistema. Dicho proceso se realiza para las configuraciones con y sin dislocaciones, y la comparación de energías permite dilucidar cuál es energéticamente más favorable.

Dicha metodología tiene éxito tanto a nivel cualitativo como cuantitativo:

- Las densidad de energía del sistema con dislocaciones disminuye para un número creciente de capas crecidas sobre el sustrato, mientras que la energía del sistema sin defectos aumenta.
- Se recupera con buena aproximación el valor del espesor crítico experimental.

En la segunda parte del capítulo, se utiliza un modelo simplificado con desplazamientos horizontales (elasticidad escalar) y con

condiciones de frontera fijas, para modelar la intercara que separa el sustrato y la película. Se aumenta gradualmente la discrepancia entre los parámetros de red (el *misfit*), mediante continuación numérica (Ap. C). En análisis de la estabilidad lineal del sistema muestra la existencia de un valor crítico del *misfit* para el que el sistema sin defectos se torna inestable. Para *misfits* mayores que el crítico, el sistema forma dislocaciones en la intercara.

D.5 RESUMEN DEL CAPÍTULO 5

D.5.1 *Aportaciones originales*

En este capítulo, se describen mediante modelos simplificados de elasticidad escalar la nucleación de dislocaciones generadas en fisuras y en experimentos de nanoindentación. Dichos modelos se adaptan a la geometría concreta de cada problema y permiten describir dislocaciones en arista (tipo *edge*) en dominios bidimensionales. La resolución numérica muestra los siguientes resultados:

- Para una fisura de tipo I se encuentra una apertura crítica a partir de la cual se generan dislocaciones en su vértice, las cuales permanecen cerca del mismo.
- En la fisura tipo II existe un valor crítico de la tensión aplicada que genera una dislocación en su vértice, la cual viaja alejándose cierta distancia del mismo.
- Un modelo sencillo de nanoindentación se obtiene introduciendo una fuerza externa que simula el efecto del nanoindentador y actúa como parametro de control. Cuando la fuerza sobrepasa cierto valor crítico, se nuclea un lazo (*loop*) con dislocaciones en los bordes de la punta. Dicho lazo encuentra su posición de equilibrio alejándose cierta distancia del nanoindentador. Pese a la sencillez del modelo, la gráfica que muestra la profundidad de penetración en función de la fuerza aplicada tiene cierto parecido con las observadas en experimentos reales.

D.5.2 *Metodología*

Los modelos propuestos en este capítulo consideran una única dirección a lo largo de la cual los átomos pueden desplazarse, ya sean con desplazamientos horizontales (u) o verticales (v). Las condiciones de contorno se establecen con átomos fijos (condiciones tipo Dirichlet) o con gradientes $g_\alpha(D_j^+ u_i)$ prescritos (condiciones tipo Neumann).

La fisura tipo I se modela aprovechando la simetría respecto al eje vertical al que pertenece el vértice de la misma (Fig. 20). Sólo la mitad derecha del dominio interviene en el modelo, siendo la otra mitad la imagen especular respecto del eje de simetría. Ello define un dominio computacional cuyos átomos en la frontera quedan fijos según la apertura de la fisura. La pared derecha del dominio tiene condiciones tipo Neumann, $D_1^+ u = 0$. La apertura crítica de la fisura a la que se forma la primera dislocación se halla mediante continuación numérica (Ap. C).

La fisura tipo II impone una deformación de cizalla (Fig. 21), de intensidad F. Los átomos de las paredes de la fisura constituyen una superficie libre, $D_2^+ v = 0$ y aquellos en las paredes laterales cumplen $D_1^+ v = 0$ (pared derecha) y $D_1^- v = 0$ pared izquierda. Los átomos en la frontera inferior permanecen fijos. La tensión crítica a la que se forma la primera dislocación se halla mediante continuación numérica.

En la nanoindentación se consideran desplazamientos verticales, v. Las fronteras izquierda y derecha cumplen $D_1^- v = 0$ y $D_1^+ v = 0$, repectivamente, al igual que la fisura tipo II. Asimismo, los átomos en la frontera inferior permanecen fijos. Tenemos igualmente una superficie libre con $D_2^+ v = 0$, salvo para los átomos i localizados bajo el indentador, que cumplen $D_2^+ v_i = -f(i)$ y están sometidos al campo de fuerza externa $f(i)$. Se hallan configuraciones de equilibrio para valores crecientes de $f(i)$ mediante continuación numérica y se representa la gráfica de la fuerza frente a la profundidad de penetración del indentador. Alcanzado cierto valor crítico de la fuerza, se produce una discontinuidad en dicha gráfica, que corresponde a la generación de un primer lazo. Este lazo está formado por dos dislocaciones nucleadas en los lados de la punta del indentador, las cuales se alejan del campo de tensiones hasta alcanzar su posición de equilibrio (Fig. 25). Continuando el proceso, se observa que las sucesivas discontinuidades en la gráfica fuerza-penetración corresponden

a la nucleación de sucesivos lazos, los cuales también se alejan de la punta del nanoindentador. La gráfica resultante (Fig. 24) es similar a la encontrada en experimentos (Fig. 1 en Ref. [57]).

D.6 CONCLUSIONES Y TRABAJO FUTURO

En la presente tesis doctoral se han formulado, analizado y aplicado modelos discretos de dislocaciones. Se ha estudiado la nucleación de dislocaciones, dipolos y lazos en diferentes contextos mediante modelos sencillos de elasticidad discreta. Siguiendo el trabajo presentado en esta memoria, se abren muchas posibilidades de trabajos futuros:

1. Extender los modelos del capítulo 2 a otras estructuras cristalinas.
2. Estudiar los efectos de la inercia en la nucleación homogénea de dislocaciones en cristales deformados mediante cizalla. Las soluciones estacionarias encontradas en el capítulo 3 son las mismas para el caso de dinámica conservativa. Sin embargo, la estabilidad de las soluciones es diferente y las diferentes soluciones que oscilan en torno a las estacionarias pueden jugar un papel fundamental. Los métodos para obtener las diferentes soluciones estables serán diferentes y sería interesante estudiar la influencia de los diferentes valores de la energía que pueden establecerse en las condiciones iniciales.
3. En el caso de los sistemas heteroepitaxiales descritos en el Cap. 4, sería interesante desarrollar una teoría analítica que describa el espesor crítico y las posibles bifurcaciones asociadas a la nucleación de dislocaciones. Dado el acuerdo obtenido con los valores experimentales, la descripción presentada pudiera acoplarse con otros modelos que describen la dinámica superficial de islas a mayor escala [51].
4. Analizar mediante la continuación numérica de bifurcaciones los problemas descritos en el capítulo 5. Sería interesante formular y analizar modelos de fisuras y nanoindentaciones más realistas en dos y tres dimensiones.

LIST OF FIGURES

LIST OF TABLES

Table 4 Results obtained for a 6x6 lattice with $A = 0.3071$ and $\alpha = 0.4$. The final stress F_f, and the ramping time t_r, determine the height y at which the dislocation dipoles are nucleated. As opposed to the results shown in Table 1 for the $\alpha = 0.4$ case in a 10x10 lattice, here we find no t_r giving rise to a BR1 configuration. 108

BIBLIOGRAPHY

[1] Doedel, E.J. , Paffenroth, R.C., Champneys, A.R., Fairgrieve, T.F., Kuznetsov, Yu.A., Oldeman, B.E., Sandstede, B., Wang. X., 2002. AUTO2000: Continuation and bifurcation software for ordinary differential equations (with HomCont). Technical Report, Concordia University.
`https://sourceforge.net/projects/auto2000/`
`http://indy.cs.concordia.ca/auto/`
(Cited on pages viii, 49, and 118.)

[2] Kim, H.J., Zhao, Z.M., Xie, Y.H., 2003. Three-stage nucleation and growth of Ge self-assembled quantum dots grown on partially relaxed SiGe buffer layers. Phys. Rev. B **68**, 205312 (7 pages). (Cited on page 1.)

[3] Zhao, Z.M., Hul'ko, O., Kim, H.J., Liu, J., Sugahari, T., Shi, B., Xie, Y.H., 2004. Growth and characterization of InAs quantum dots on Si(001) surfaces. J. Crystal Growth **271**, 450-455. (Cited on page 1.)

[4] Grahn, H. T. (editor), 1995. Semiconductor Superlattices: Growth and Electronic Properties. World Scientific, Singapore. (Cited on page 1.)

[5] Zhu T., Li J., Van Vliet K.J., Ogata S., Yip S. and Suresh S., 2004. Predictive modeling of nanoindentation-induced homogeneous dislocation nucleation in copper. J. Mech. Phys. Solids **52**, 691. (Cited on pages 1 and 46.)

[6] Li, J., Van Vliet, K.J., Zhu, T., Yip, S. and Suresh, S., 2002. Atomistic mechanisms governing elastic limit and incipient plasticity in crystals. Nature **418**, 307. (Cited on pages 1 and 46.)

[7] Tadmor, E. B., Ortiz, M., Phillips, R., 1996. Quasicontinuum analysis of defects in solids. Philosophical Magazine A, **73**, 1529-1563. (Cited on page 2.)

[8] Bulatov, V. V., Cai, W., 2006. Computer simulations of dislocations, Oxford U.P., Oxford, UK. (Cited on pages 2, 4, 5, 6, and 9.)

[9] Liu, W. J., Xin X. J., 2005. A Multiscale Hybrid Method for materials containing defects and inhomogeneities. WIT Transactions on Modelling and Simulation, **41**. Computational Methods and Experimental Measurements XII, 407. (Cited on page 2.)

[10] Foell, H., Webpage on Defects in Crystals, `http://www.tf.uni-kiel.de/matwis/amat/def_en/index.html`. (Cited on page 5.)

[11] Hull, D., Bacon, D.J. 2001. Introduction to Dislocations, 4th edition. Butterworth-Heinemann, Oxford UK. (Cited on pages 5, 30, and 39.)

[12] Nabarro, F.R.N., 1967. Theory of Crystal Dislocations. Oxford University Press, Oxford, UK. (Cited on pages 5, 11, 20, and 57.)

[13] Landau, L.D., Lifshitz, E.M., 1986. Theory of elasticity, 3rd edition. Pergamon Press, London. (Cited on pages 5, 7, 20, 22, 23, and 24.)

[14] Hirth, J.P., Lothe, J., 1982. Theory of Dislocations, 2nd edition. John Wiley and Sons, New York. (Cited on pages 4, 5, 7, 39, 40, 64, and 95.)

[15] Mura, T., 1987. Micromechanics of defects in solids, 2nd. rev. ed., Martinus Nijho Publs., Dordrecht, 1987. (Cited on pages 5 and 8.)

[16] Bonilla, L.L., Carpio, A. Defects, Singularities and Waves. Procs. Lax-Nirenberg 2006, Toledo, Spain, edited by L.L. Bonilla, A. Carpio, J.M. Vega and S. Venakides. AMS Symposia in Applied Mathematics, AMS, to appear. (Cited on pages 4 and 5.)

[17] Baskes, M.I., 1992. Modified embedded-atom potentials for cubic materials and impurities. Phys. Rev. B **46**, 2727. (Cited on page 6.)

[18] Groma, I., Bakó, B., 2000. Dislocation patterning: From micro- to mesoscale description. Phys. Rev. Lett. **84**, 1487-1490. (Cited on page 8.)

[19] Wang, Y. U., Jin, Y. M., Cuitino, A. M., Khatachuryan, A. G., 2001. Nanoscale phase field microelasticity theory of dislocations: model and 3D simulations. Acta Materialia **49** (10), 1847-1857. (Cited on page 8.)

[20] Xiang, Y., Cheng, L. T., Srolovitz, D. J., E, W., 2003. A level set method for dislocation dynamics. Acta Materialia **51** (18), 5499-5518. (Cited on page 8.)

[21] Kubin, L. P., Canova, G., 1992. The modelling of dislocation patterns. Scripta Metallurgica et Materialia **27** (8), 957-962. (Cited on page 9.)

[22] Zbib, H. M., de la Rubia, T. D., Bulatov, V. V., 2002. A Multiscale Model of Plasticity Based on Discrete Dislocation Dynamics. International Journal of Mechanical Sciences **124** (1), 78-87. (Cited on page 9.)

[23] Ghoniem, N. M., Tong, S. H., Sun, L. Z., 2000. Parametric dislocation dynamics: A thermodynamics-based approach to investigations of mesoscopic plastic deformation. Physical Review B **61** (2), 913-927. (Cited on page 9.)

[24] Van der Giessen, E., Needleman, A., 2005. Discrete Dislocation Plasticity. Handbook of Materials Modeling, ed. S. Yip, Springer, pp. 1115-1131. (Cited on page 9.)

[25] Peierls, R., 1940. The size of a dislocation. Proc. Phys. Soc., **52**, 34. (Cited on page 10.)

[26] Frenkel, J., Kontorova, T., 1939. On the theory of plastic deformation and twinning. J. Phys. Moscow **1**, 137-149. (Cited on page 11.)

[27] Frank, F. C., van der Merwe, J. H., 1949. One dimensional dislocations. II. Misfitting monolayers and oriented overgrowth. Proc. Roy. Soc. (London) A **198**, 216-225. (Cited on page 11.)

[28] Suzuki, H., 1967. Motion of dislocations in body-centered cubic crystals, in Dislocation Dynamics, ed. by A. H. Rosenfield et al. MacGraw Hill, New York, pp. 679-700. (Cited on page 11.)

[29] Landau, A. I., Kovalev, A.S., Kondratyuk, A. D. 1993. Model of interacting atomic chains and its application to the description of the crowdion in an anisotropic crystal. Phys. stat. sol. (b) 179 (1993), 373-381. (Cited on page 11.)

[30] Ariza, M. P., Ortiz, M., 2005. Discrete Crystal Elasticity and Discrete Dislocations in Crystals. Archive for Rational Mechanics and Analysis **178**, 149-226. (Cited on page 11.)

[31] Ramasubramaniam, A., Ariza, M. P., Ortiz, M., 2007. A discrete mechanics approach to dislocation dynamics in BCC crystals. Journal of the Mechanics and Physics of Solids **55**, 3, 615-647. (Cited on page 11.)

[32] Carpio, A., Bonilla, L.L., 2003. Edge dislocations in crystal structures considered as traveling waves of discrete models. Phys. Rev. Lett. **90**, 135502 (4 pages). (Cited on pages 11, 21, and 46.)

[33] Carpio, A., Bonilla, L.L., 2005. Discrete models of dislocations and their motion in cubic crystals. Phys. Rev. B **71**, 134105 (10 pages). (Cited on pages 12, 13, 15, 17, 18, 21, 27, 29, 33, 36, 42, 46, 48, 89, 96, 98, 116, and 117.)

[34] Bonilla L.L., Carpio A. and Plans I., 2007. Dislocations in cubic crystals described by discrete models. Physica A **376**, 361. (Cited on pages 13, 46, 98, and 117.)

[35] Carpio, A., Plans, I., Bonilla, L.L. 2004. Atomic models of dislocations for Si and GaAs. Proceedings of the European Congress of Computational Methods in Applied Sciences and Engineering, ECCOMAS 2004. Jyväskylä, Finland, July 24-28th, 2004. (Cited on page 13.)

[36] Carpio, A., Bonilla L.L., Plans I., 2006. Discrete models for defects and their motion in crystals. Proceedings of the 3rd Conference on Multiscale Modeling of Materials, Freiburg. (Cited on page 13.)

[37] Plans, I., Carpio, A., Bonilla, L.L. Homogeneous nucleation of dislocations as bifurcations in a discrete elasticity model. Preprint. (Cited on pages 13 and 100.)

[38] Carpio, A., Plans, I., Bonilla, L.L., 2007. Homogeneous nucleation of dislocations. In Procs. of the 11th International Symposium on Continuum Models and Discrete Systems (CMDS11), Paris, France, 30 July - 3 August 2007, edited by D. Jeulin. (Cited on page 13.)

[39] Plans, I., Carpio, A., Bonilla, L.L., Caflisch, R.E., 2007. Critical thickness for misfit dislocation formation in InAs/GaAs(110) heteroepitaxy. In *Progress in Industrial Mathematics at ECMI 2006*, L.L. Bonilla, M.A. Moscoso, G. Platero and J.M. Vega, eds. Mathematics in Industry **12**. Springer, Berlin 2007 (in press). (Cited on page 13.)

[40] Landau, L.D., Lifshitz, E.M., 1959. Fluid Mechanics, Pergamon Press, London. (Cited on pages 15, 23, 26, and 117.)

[41] Van Saarloos, W., Bedeaux, D., Mazur, P., 1982. Non-linear hydrodynamic fluctuations around equilibrium. Physica A **110**, 147-170. (Cited on pages 15, 23, 26, and 117.)

[42] Romero-Rochín, V., Rubí, J.M., 1998. Discretized integral hydrodynamics. Phys. Rev. E **58**, 1843ï¿½1850. (Cited on pages 15 and 26.)

[43] Rickman, J.M., Viñals, J., 1997. Modeling of dislocation structures in materials. Phil. Mag. A **75**, 1251-1262. (Cited on page 15.)

[44] Groma, I., Csikor, F. F., Zaiser, M., 2003. Spatial correlations and higher-order gradient terms in a continuum description of dislocation dynamics. Acta Mater. **51**, 1271-1281. (Cited on page 15.)

[45] Hähner, P., Bay, K., Zaiser, M., 1998. Fractal Dislocation Patterning During Plastic Deformation. Phys. Rev. Lett. **81**, 2470-2473. (Cited on page 15.)

[46] Bedeaux, D., Albano, A.M., Mazur, P., 1975. Boundary conditions and nonequilibrium thermodynamics. Physica A **82**, 438-462. (Cited on page 26.)

[47] Gomila, G., Rubí, J.M., 1998. Fluctuations generated at semiconductor interfaces. Physica A **258**, 17-31. (Cited on page 26.)

[48] Grahn, H. T., 1999. Introduction to Semiconductor Physics. World Sci., Singapore. (Cited on page 30.)

[49] Matthews, J.W., Blakeslee, A.E., 1974. Defects in epitaxial multilayers. I. Misfit dislocations. J. Crystal Growth **27**, 118-125. (Cited on page 30.)

[50] Szuromi, P., Clery, D., eds., 1998. Special Issue on Control and use of defects in materials. Science **281**, 939. (Cited on page 30.)

[51] Gyure, M. F., Ratsch, C., Merriman, B., Caflisch, R. E., Osher, S., Zinck, J. J., Vvedensky, D. D., 1998. Level-set methods for the simulation of epitaxial phenomena. Phys. Rev. E **58**, R6927-R6930. (Cited on pages 30, 91, and 123.)

[52] Born, M., Huang, K., 1954. Dynamic Theory of Crystal Lattices. Oxford University Press, Oxford, UK. (Cited on pages 30, 31, and 32.)

[53] Hjort, K., Söderkvist, J., Schweitz, J. A., 1994. Gallium arsenide as a mechanical material. J. Micromech. Microeng. **4** 1-13. (Cited on page 40.)

[54] Cottam, R. I., Saunders, G. A., 1973. Elastic constants of GaAs from 2 K to 320 K. J. Phys. C: Solid State Phys., Vol **6**(13): 2105-2118. (Cited on page 40.)

[55] Nikanorov, S. P., Burenkov, Yu. A., Stepanov, A. V., 1971. Elastic properties of silicon. Sov. Phys. Solid State **13**(10), 2516-2518, 1972 [Fiz. Tverd. Tela **13**, 3001-3004]. (Cited on page 40.)

[56] Burenkov, Yu. A., Burdukov, Yu. M., Davidov, S. Yu., Nikanorov, S. P., 1973. Temperature dependences of the elastic constants of gallium arsenide. Sov. Phys. Solid State **15**(6), 1175-1177. [Fiz. Tverd. Tela **13**, 1757-1761]. (Cited on page 40.)

[57] Asenjo A., Jaafar M., Carrasco E. and Rojo J.M., 2006. Dislocation mechanisms in the first stage of plasticity of nanoindented Au (111) surfaces. Phys. Rev. B **73**, 075431. (Cited on pages 45, 46, 84, 85, 86, 123, and 129.)

[58] Rodríguez de la Fuente O., Zimmerman J.A., González M.A., de la Figuera J., Hamilton J.C., Pai W.W., Rojo J.M., 2002. Dislocation Emission around Nanoindentations on a (001) fcc Metal Surface Studied by Scanning Tunneling Microscopy and Atomistic Simulations. Phys. Rev. Lett. **88**, 0361011. (Cited on page 45.)

[59] Breen K.R., Uppal P.N., Ahearn J.S., 1990. Homogeneous nucleation of dislocations in InGaAs/GaAs near critical thickness. J. Vac. Sci. Technol. B **8**, 730. (Cited on page 45.)

[60] Joyce B.A., Vvedensky D.D., 2004. Self-organized growth on GaAs surfaces. Mater. Sci. Eng. R **46**, 127. (Cited on page 45.)

[61] Schall P., Cohen I., Weitz D. and Spaepen F., 2006. Visualizing dislocation nucleation by indenting colloidal crystals. Nature **440**, 319. (Cited on page 45.)

[62] Gouldstone A., Van Vliet K.J. and Suresh S., 2001. Nanoindentation: simulation of defect nucleation in a crystal . Nature **411**, 656. (Cited on page 45.)

[63] Lorenz D., Zeckzer A., Hilpert U., Grau P., Johansen H., 2003. Pop-in effect as homogeneous nucleation of dislocations during nanoindentation. Phys. Rev. B **67**, 172101. (Cited on page 46.)

[64] Ogata S., Li J. and Yip S., 2002. Ideal Pure Shear Strength of Aluminum and Copper. Science **298**, 807. (Cited on page 46.)

[65] Landau A. I., 1994. Application of a model of interacting atomic chains for the description of edge dislocations. Phys. stat. sol. (b) **183**, 407. (Cited on page 48.)

[66] Bonilla L. L., Escobedo R. and Dell'Acqua G., 2006. Voltage switching and domain relocation in semiconductor superlattices. Phys. Rev. B **73**, 115341. (Cited on page 51.)

[67] Joyce, B. A., Vvedensky, D. D., 2004. Self-organized growth on GaAs surfaces. Mater. Sci. Eng., R. **46**, 127. (Cited on page 63.)

[68] Zhang, X., Pashley, D. W., Hart, L., Neave, J. H., Fawcett P. N., Joyce, B. A., 1997. The morphology and asymmetric strain relief behaviour of InAs films on GaAs (110) grown by molecular beam epitaxy. J. Cryst. Growth **131**, 300. (Cited on page 64.)

[69] Belk, J. G., Sudijono, J. L., Zhang, X. M., Neave, J. H., Jones, T. S., Joyce, B. A., 1997. Surface Contrast in Two Dimensionally Nucleated Misfit Dislocations in InAs/GaAs (110) Heteroepitaxy. Phys. Rev. Lett. **78**, 475. (Cited on pages 64 and 120.)

[70] Shiraishi, K., Oyama, N., Okajima, K., Miyagishima, N., Takeda, K., Yamaguchi, H., Ito, T., Ohno.,T., 2002. First principles and macroscopic theories of semiconductor epitaxial growth. J. Crystal Growth **237-239**, 206. (Cited on page 64.)

[71] Carrasco, E. PhD thesis. Universidad Complutense de Madrid (2005). (Cited on page 84.)

[72] Landau, A. I., Kovalev A. S., and Kondratyuk, A. D., 1993. Model of interacting atomic chains and its application to the description of the crowdion in an anisotropic crystal. Phys. Status Solidi B **179**, 373; A. I. Landau, 1994. Application of a model of interacting atomic chains for the description of edge dislocations. Phys. Status Solidi B **183**, 407. (Cited on page 89.)